Citation (APA)
Paul, A. (2026). *Advancing Optical Metrology with Coherent Fourier Scatterometry*. [Dissertation (TU Delft), Delft University of Technology]. https://doi.org/10.4233/uuid:66d43150-130e-4553-acc5-a8d91910a243

Advancing

Optical Metrology

with

Coherent Fourier Scatterometry

Anubhav Paul

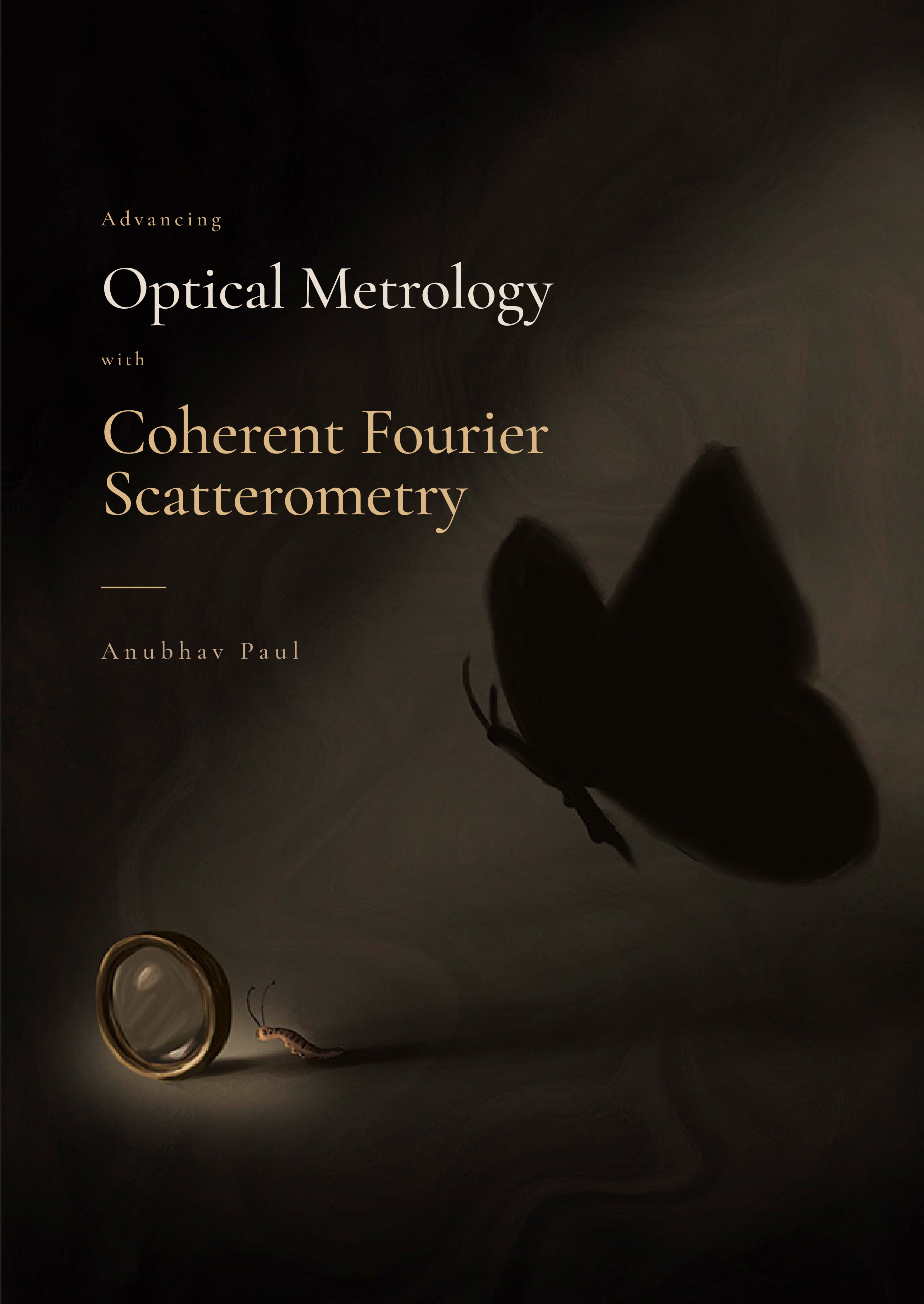

ADVANCING OPTICAL METROLOGY WITH
COHERENT FOURIER SCATTEROMETRY

ADVANCING OPTICAL METROLOGY WITH COHERENT FOURIER SCATTEROMETRY

Dissertation

for the purpose of obtaining the degree of doctor
at Delft University of Technology
by the authority of the Rector Magnificus,
Prof. dr. ir. H. Bijl,
chair of the Board for Doctorates
to be defended publicly on
Monday, 15th of June 2026 at 10:00

by

Anubhav PAUL

This dissertation has been approved by the promotors.

Composition of the doctoral committee:

Rector Magnificus,	chairperson
Dr. ir. S.F. Pereira,	Delft University of Technology, *promotor*
Prof. dr. W.M.J.M. Coene,	Delft University of Technology, *promotor*
Independent members:	
Prof. dr. S. Conesa-Boj,	Delft University of Technology
Prof. dr. S.M. Witte,	Delft University of Technology
Prof. dr. A.J. den Boef,	Vrije Universiteit Amsterdam, The Netherlands
Prof. dr. P. Petrik,	University of Debrecen, Hungary
Prof. dr. A. Fiore,	Eindhoven University of Technology, The Netherlands

Keywords: scatterometry; optical metrology; defect inspection & characterization

Printed by: Gildeprint

Cover by: Sawrav Cintury

ISBN: 978-94-6518-318-3

What we observe is not nature itself,
but nature exposed to our method of questioning.

– Werner Heisenberg

Cover:

The cover illustrates the central idea of this thesis: extracting information about nanoscale structures through the scattering of light. The lens symbolizes the measurement system used to probe nanoscale objects, represented here by the caterpillar. While the object itself appears small and simple, its interaction with light gives rise to a far-field shadow that takes the form of a butterfly. This reflects the principle of optical scatterometry, where information about an object is not obtained through direct observation but inferred from the scattered light it produces. The transformation from caterpillar to butterfly also carries an abstract meaning: that the shadow cast far from an object can reveal something far more complex and meaningful than the object itself – a hidden truth that only emerges through interaction with light.

CONTENTS

SUMMARY

Optical metrology lies at the foundation of modern semiconductor manufacturing, nanophotonics, and emerging two-dimensional material technologies. As device dimensions continue to shrink and architectures become increasingly three-dimensional, the demand for non-destructive, high-resolution, and high-throughput characterization methods has never been greater. This thesis addresses this technological and scientific need by advancing **coherent Fourier scatterometry (CFS)**, a technique that leverages far-field scattering information to probe matter at the nanoscale. Throughout this work, CFS is developed from a directional defect-inspection method into a multi-purpose metrology platform capable of detecting, quantifying, classifying, and retrieving optical and structural properties in regimes traditionally limited by optical diffraction or model complexity. The chapters that follow present these developments as a coherent progression, demonstrating that CFS has capacity well beyond its conventional scope.

Beginning with surface inspection, this thesis established CFS as a non-destructive method capable of detecting subwavelength defects on periodic nanostructures such as diffraction gratings. Through combined 3D-FDTD modeling and experimental validation, we demonstrated that coherent detection amplifies weak perturbations, enabling the identification of contamination particles and common fabrication defects. Building on this, we explored one of the hardest industrial metrology challenges, **defect detection near edges**, where scattering backgrounds, geometry asymmetry, and orientation dependence typically degrade sensitivity. The development of a **quad-detection architecture** showed how directional scattering information can be recovered and processed independently, extending CFS applicability to arbitrarily oriented features and improving edge-adjacent defect visibility.

CFS was further extended beyond surface-only problems by shifting operation to the near-infrared regime, exploiting silicon transparency to investigate deeply buried nanostructures without invasive preparation. This demonstrated detection of nanoparticles, nanopits, nanopillars, and gratings hidden beneath silicon layers up to hundreds of micrometers thick, directly addressing metrology needs in wafer bonding, 3D integration, and subsurface inspection. In parallel, the thesis addressed a second major limitation of existing scatterometry: the dependency on inverse modeling. By introducing **a visibility-based metric for steep sidewall angle and height quantification**, we demonstrated that certain structural parameters can be extracted directly from scattering signatures without iterative optimization. This approach enables fast, model-light metrology for aperiodic cliff-like structures, validated against AFM measurements.

Beyond dimensional analysis, this thesis explored whether CFS can be used not only to retrieve *what is the size of the structure*, but also *what shape it has*. A rotation-dependent scattering method was developed that classifies nanopillars based on symmetry, enabling the identification of cylindrical, triangular, square, and rectangular pillars even below the diffraction limit. Finally, we introduced **AnisoVision**, a deep-learning-assisted

CFS framework capable of retrieving the complete anisotropic refractive index tensor of 2D materials from single-shot angular scattering patterns. This marks a conceptual expansion of CFS, from geometry to material property metrology, opening pathways for characterization of van der Waals crystals and layered media with spatial resolution far beyond what conventional ellipsometry offers.

Across these studies, several themes emerge:

- **CFS is flexible**: It can be adapted to surface, buried, periodic, and isolated structures.
- **CFS is scalable**: With appropriate illumination and detection design, it can operate inline, in real time.
- **CFS is information-rich**: Angular scattering carries recoverable signatures of geometry, anisotropy, and defects.
- **CFS can evolve**: Through new detection modalities, spectral operation, or machine learning, it becomes a more complete metrology system.

Collectively, the contributions of this thesis extend CFS from a defect-inspection technique into a broader nanoscale metrology platform capable of detection, quantification, classification, and optical property retrieval. These results position CFS as a strong candidate for adoption in next-generation semiconductor, nanophotonic, and 2D material processing environments.

SAMENVATTING

Optische metrologie vormt de basis van moderne halfgeleiderfabricage, nano-fotonica en opkomende tweedimensionale materialentechnologieën. Naarmate apparaatafmetingen blijven afnemen en architecturen steeds driedimensionaler worden, is de behoefte aan niet-destructieve, hoge-resolutie en hoog-doorvoer karakterisatietechnieken groter dan ooit. Dit proefschrift speelt in op deze technologische en wetenschappelijke uitdaging door **coherent Fourier scatterometry (CFS)** verder te ontwikkelen, een techniek die verstrooiingsinformatie in het verre veld benut om materie op nanoschaal te onderzoeken. In dit werk transformeert CFS van een directionele defectinspectiemethode naar een veelzijdig metrologieplatform dat structuren kan detecteren, kwantificeren, classificeren en optische en structurele eigenschappen kan bepalen in regimes die traditioneel beperkt worden door diffractielimieten of modelcomplexiteit. De daaropvolgende hoofdstukken presenteren deze ontwikkeling als een logische voortgang, waarbij wordt aangetoond dat CFS veel verder reikt dan het conventionele toepassingsgebied.

Te beginnen bij oppervlakte-inspectie toont dit proefschrift aan dat CFS een niet-destructieve methode is die subwavelength defecten kan detecteren op periodieke nanostructuren zoals diffractieroosters. Met behulp van gecombineerde 3D-FDTD simulaties en experimenten laten wij zien dat coherente detectie zwakke verstoringen versterkt, waardoor contaminatie deeltjes en veelvoorkomende fabricagedefecten zichtbaar worden. Vervolgens zijn we ingegaan op een van de grootste industriële metrologie uitdagingen: **defectdetectie nabij randen**, waar verstrooiingsachtergronden, geometrische asymmetrie en oriëntieafhankelijkheid de gevoeligheid vaak beperken. De ontwikkeling van een **quad-detectiearchitectuur** laat zien hoe directionele verstrooiingsinformatie onafhankelijk kan worden uitgelezen en verwerkt, waardoor CFS toepasbaar wordt bij willekeurige oriëntaties en de detectiegevoeligheid aan randen aanzienlijk wordt verbeterd.

CFS is verder uitgebreid voorbij oppervlaktemetingen door over te schakelen naar het nabij-infrarode golflengtegebied, waarbij gebruik wordt gemaakt van de transparantie van silicium om diep begraven nanostructuren te onderzoeken zonder destructieve samplevoorbereiding. Hiermee tonen wij detectie aan van nanodeeltjes, nanopits, nanopillars en roosters onder siliciumlagen tot honderden micrometers dik, een directe stap richting metrologie voor wafer bonding, 3D-integratie en subsurface inspectie. Parallel daaraan is een tweede grote beperking van conventionele scatterometrie aangepakt: de afhankelijkheid van inverse modellering. Door het introduceren van **een visibility gebaseerde metriek voor de bepaling van steile sidewall hoeken en hoogte**, laten wij zien dat structurele parameters rechtstreeks kunnen worden afgeleid uit verstrooiingssignaturen, zonder iteratieve optimalisatie. Dit maakt snelle, model arme metrologie mogelijk van niet-periodieke cliff-achtige structuren, gevalideerd met AFM metingen.

Naast dimensionale analyse onderzoekt dit proefschrift of CFS niet alleen kan bepalen *hoe groot* een structuur is, maar ook *welke vorm* deze heeft. Een rotatie-afhankelijke verstrooiingsmethode wordt geïntroduceerd waarmee nanopillars kunnen worden geclassificeerd op basis van symmetrie, inclusief cilindrische, driehoekige, vierkante en rechthoekige vormen, zelfs wanneer hun dimensies onder de diffractielimiet liggen. Tot slot introduceren wij **AnisoVision**, een deep-learning ondersteund CFS raamwerk dat in staat is de volledige anisotrope brekingsindex-tensor van 2D-materialen te reconstrueren uit enkelvoudige far-field metingen. Dit markeert een conceptuele uitbreiding van CFS, van zuiver geometrische metrologie naar materiaaleigenschapkarakterisatie, en opent nieuwe routes voor het analyseren van van der Waals kristallen en gelaagde structuren met een ruimtelijke resolutie die conventionele ellipsometrie overstijgt.

Over de volledige breedte van dit onderzoek komen duidelijke thema's naar voren:

- **CFS is flexibel**: toepasbaar op oppervlakkige, begraven, periodieke en geïsoleerde structuren.
- **CFS is schaalbaar**: met geschikte belichting en detectie kan het inline en realtime functioneren.
- **CFS is informatierijk**: hoeksverstrooiing bevat herleidbare signaturen van geometrie, anisotropie en defecten.
- **CFS kan evolueren**: via nieuwe detectieschema's, spectrale uitbreiding en machine learning groeit het uit tot een completer metrologieplatform.

Gezamenlijk tonen de bijdragen in dit proefschrift aan dat CFS is getransformeerd van een defectinspectietechniek naar een bredere nanoschaal-metrologie-architectuur, geschikt voor detectie, kwantificatie, classificatie en optische parameterextractie. Deze resultaten positioneren CFS als een sterke kandidaat voor toepassing in toekomstige generaties halfgeleider-, nanofotonische en 2D materiaalverwerkingsprocessen.

1

INTRODUCTION

Anubhav Paul

> *Measure what can be measured, and make measurable what cannot be measured.*
>
> – Galileo Galilei

Optical metrology underpins semiconductor manufacturing by enabling precise, non-destructive, and high-throughput measurement of nanoscale structures. This chapter traces the evolution of optical metrology and microscopy, highlighting the capabilities and limitations of established techniques such as SEM, AFM, scatterometry, and X-ray methods. It then introduces coherent Fourier scatterometry (CFS) — a technique that exploits the full optical field to enhance sensitivity and information content. The chapter reviews the development of CFS research, identifies open challenges, formulates key research questions, outlines the methodological approach by combining simulations and experiments, and provides the contents of this thesis.

1.1. A BRIEF HISTORY AND EVOLUTION OF OPTICAL METROLOGY AND MICROSCOPY

METROLOGY—the science of measurement—enables reliable quantification and comparison of physical properties and underpins technological progress across science and industry. As Lord Kelvin famously argued, “when you can measure what you are speaking about, and express it in numbers, you know something about it” [1]. Optical metrology, which leverages the interaction of light with matter, offers unique advantages: it is inherently non-contact, fast, scalable across length scales, and richly multiplexed in the information channels carried by the optical field (amplitude, phase, polarization, spectrum, angular momentum, and direction) [2, 3]. These advantages have made optics central to length standards, microscopy, manufacturing quality control, and modern semiconductor metrology.

1.1.1. FROM LENSES TO LIMITS: PRE-LASER FOUNDATIONS

The roots of optical metrology intertwine with the rise of optical imaging. Pioneering observations by Hooke and van Leeuwenhoek in the 17th century legitimized the microscope as a scientific instrument and catalyzed centuries of innovation in lens design, illumination, and contrast mechanisms [4–6]. The 19th century then established the conceptual framework: Abbe’s theory of image formation exposed the fundamental role of diffraction in limiting resolution, relating resolvable detail to numerical aperture (NA) and wavelength, thereby defining the levers, such as shorter wavelengths, higher NA, and contrast engineering, for advances in optical metrology and microscopy [7, 8].

In parallel, optical interferometry matured from qualitative fringe inspection into quantitative surface metrology, enabling precise figure and roughness assessment of optical components. Well before lasers, large-aperture optics were tested using slope-based methods (Foucault, Hartmann) and reference-plate interference rings; these evolved into robust interferometric practices once coherent sources became available [9]. On the standards side, optics profoundly shaped the realization of SI units: the meter transitioned from artifact bars to wavelength definitions (e.g., Kr-86) and later to a definition based on the speed of light, while optical frequency standards now drive discussions about redefining the second [10–12].

1.1.2. THE LASER REVOLUTION AND QUANTITATIVE OPTICS

The advent of the laser provided bright, stable, and highly coherent light, transforming interferometry and enabling phase-measuring interferometry, synthetic-wavelength methods, holography, and precision wavefront sensing. In optical testing, lasers accelerated the transition from slope-based diagnostics to direct phase mapping of surface topography and aberrations, supported by advances in detectors and computational phase retrieval [9]. In microscopy, confocal architectures (conceptually introduced mid-20th century and popularized with lasers and scanning in the late 20th century) improved sectioning and contrast, while fluorescence and later super-resolution pushed spatial resolution below Abbe’s classical limits through non-linear and statistical strategies [8, 13].

Beyond imaging, spectroscopic ellipsometry and reflectometry exploited polarization and spectral phase to quantify thin films with sub-nanometer precision, and diffractometry (including scatterometry) leveraged angular distribution of light to infer periodic structure geometry non-destructively and at high throughput [3]. Collectively, these techniques illustrate a recurring theme: metrology power grows when we access *more of the optical field* (amplitude *and* phase, multiple polarizations, richer angular/spectral sampling) and when we couple measurements tightly with rigorous electromagnetic modeling.

1.1.3. INDUSTRIALIZATION: FROM OPTICS LABS TO IN-LINE METROLOGY

As micro- and nano-fabrication advanced, optical metrology evolved from lab-based characterization to in-line process control. Semiconductor manufacturing is representative: decreasing critical dimensions (CDs), complex 3D profiles, multilayer stacks, and material diversity created intense pressure for fast, non-destructive, and model-based metrology. Optical scatterometry (often called optical critical dimension metrology (OCD)) became a workhorse for periodic targets, while interferometry, ellipsometry, confocal and coherence-scanning optical profilers, and angle-resolved tools addressed surfaces, films, and structures at scale [3, 14]. Concomitantly, traceability and uncertainty quantification remained central, with optics integral to maintaining and disseminating SI units [2].

1.1.4. CONTEMPORARY CHALLENGES THAT MOTIVATE NEW APPROACHES

Despite remarkable progress, several persistent and emerging challenges motivate continued innovation in optical metrology:

- **Resolution vs. throughput vs. robustness:** pushing toward smaller features and higher NA often conflicts with field of view, mechanical stability, and process compatibility; methods must balance sensitivity with speed and operational simplicity
- **Complex samples and materials:** non-idealities such as edge effects, roughness, subsurface or buried features, anisotropic and dispersive media, and multi-scale complexity stress forward models and inversion stability
- **Full-field information access:** many industrial instruments primarily exploit intensity; however, richer information (phase, polarization-resolved responses, full angular content) can dramatically improve sensitivity and enable clearer distinction between coupled parameters when combined with rigorous modeling
- **Traceability and uncertainty:** as optical metrology informs critical manufacturing decisions, defensible uncertainty budgets and links to standards remain essential
- **Digital integration:** modern systems increasingly rely on computational optics, inverse modeling, and data-driven filtering to stabilize ill-posed inversions and to focus on the most informative measurements

These historical developments are summarized in Table 1.1, which highlights key milestones from the birth of optical microscopy in the 17th century to the emergence of model-based scatterometry and computational metrology in the 21st century. Optical metrology has continuously evolved from simple lens-based magnifiers to sophisticated, model-driven techniques capable of resolving nanostructures and quantifying

Table 1.1: Selected milestones in optical metrology and microscopy.

Era / Year	**Milestone**
17th century	Hooke, van Leeuwenhoek establish microscopy as a scientific tool; conceptual roots of contrast and lens design [4, 6].
19th century	Abbe's diffraction theory formalizes resolution and role of NA; interferometry matures for optical testing [7].
1950s–1960s	Confocal concept and laser era catalyze quantitative phase metrology and high-contrast microscopy [9, 13].
1960s–1980s	Phase-measuring interferometry, holography, and ellipsometry become precision tools for surface and thin-film metrology [3, 9].
1990s–2000s	Optical scatterometry adopted for in-line semiconductor metrology; model-based inversions standardize [14].
2000s–present	Computational optics, polarization/phase-aware methods, and angular-domain metrology (incl. CFS/OCD) address nanoscale, high-throughput needs [3, 13].

their material and geometrical parameters. The progression reflects a consistent trend: expanding the accessible information from the optical field (amplitude, phase, polarization, spectrum, and angular distribution) and combining it with increasingly accurate electromagnetic modeling to extract quantitative insights.

These trends naturally set the stage for approaches that *scan* an engineered probe, *collect* the scattered field in the Fourier (angular) domain, and *invert* with rigorous solvers while exploiting all accessible information channels. CFS, introduced in the next section, emerges precisely from this logic.

1.2. COHERENT FOURIER SCATTEROMETRY: PRINCIPLES AND EVOLUTION

1.2.1. PRINCIPLES AND MOTIVATION

Coherent Fourier scatterometry (CFS) is an optical metrology technique designed to exploit the information content carried by light scattered from a structure. Traditional optical scatterometry typically measures only the intensity distribution of diffracted light, which limits the amount of retrievable information. In contrast, CFS leverages the amplitude, phase, polarization, and angular distribution of the scattered field [15]. By measuring the scattered light in the Fourier plane (also known as the back focal plane), CFS captures the complex interference pattern of diffracted orders across a large range of spatial frequencies, revealing subtle sample-dependent signatures that are often invisible to intensity-only approaches.

The core concept of CFS is straightforward yet powerful: a spatially coherent beam (commonly a focused laser spot) illuminates the sample, and the scattered field is collected and analyzed in the Fourier/angular domain. The interaction of this coherent field with nanoscale features modifies both its amplitude and phase, and the resulting far-field pattern encodes rich information about the structure's geometry, composition, and material properties. With rigorous electromagnetic modeling, this information can be inverted to retrieve critical parameters such as height, width, sidewall angle, overlay offset, and shape of nanostructures, located both on the surface or buried in the substrate [16, 17].

Coherence also enables new modalities not accessible with incoherent illumination. Interference between diffracted orders can reveal phase differences that are highly sensitive to structural asymmetries, while polarization-resolved detection disentangles contributions arising from different components of the optical response of anisotropic materials. Additionally, illumination or detection strategies, such as engineered pupil functions, structured light, or multi-position scanning, can further enhance sensitivity and parameter separability [18].

1.2.2. COMPARISON WITH CONVENTIONAL OPTICAL AND NON-OPTICAL METROLOGY TECHNIQUES

Optical scatterometry and CFS are part of a broader landscape of dimensional and structural metrology techniques used in semiconductor manufacturing. Each method offers specific advantages but also faces inherent limitations when confronted with the increasing complexity of advanced device architectures. This section briefly reviews the most widely used approaches and positions CFS within this context (a comparative overview of major metrology techniques used in semiconductor manufacturing is provided in Table 1.2).

ELECTRON AND PROBE-BASED METROLOGY

Critical-dimension scanning electron microscopy (CD-SEM) remains the industrial workhorse for inline dimension control, offering sub-nanometer spatial resolution and direct imaging of structures [19, 20]. However, it suffers from several drawbacks: low throughput, vacuum operation requirements, potential for charging and contamination, limited 3D profile information, and, in some cases, it suffers from low contrast [21]. Cross-sectional transmission electron microscopy (TEM) and scanning TEM (STEM) provide unparalleled atomic-scale detail, but their destructive nature, elaborate sample preparation, and long measurement times confine them to reference metrology rather than inline control [22, 23].

Scanning probe techniques such as atomic force microscopy (AFM) and other scanning probe microscopy (SPM) methods also deliver high-resolution surface information and are capable of measuring 3D topography and sidewall angles. Nevertheless, their limited scan area, slow acquisition, and sensitivity to tip-sample interactions make them unsuitable for high-throughput or inline reference metrology [19, 24].

FAR-FIELD OPTICAL TECHNIQUES

Ellipsometry and reflectometry are well-established techniques for thin-film metrology and optical constant extraction due to their non-destructive nature, high throughput, and experimental simplicity, but they provide limited structural information and are not suited for detecting localized defects [20, 25]. Conventional optical scatterometry (OCD) addresses this by inferring structural parameters from diffraction signatures using

Table 1.2: Comparison of CFS with the major metrology techniques for semiconductor manufacturing (adapted from [19, 20, 23]).

Technique	Resolution	Throughput	Destructive	Key Limitations
CD-SEM	< 5 nm	Low	no	Slow, vacuum, charging
TEM/STEM	< 0.1 nm	Very low	yes	Destructive, prep-intensive
AFM/SPM	$\sim$1 nm (lateral)	Very low	yes	Small area, slow
Ellipsometry	10–100 nm	High	no	Model dependent
OCD (incoherent)	2–10 nm	High	no	Needs periodicity, intensity only
X-ray Scatterometry	1–5 nm	Low	no	Complex, costly
EUV Scatterometry	$\sim$1 nm	Medium	no	Source cost, infrastructure
CFS	1–10 nm	High	no	Model complexity

a predefined model of the nominal structure. In high-volume semiconductor manufacturing, OCD is widely used to monitor small process-induced deviations (typically $< 5\%$) and to provide feedback to lithography scanners, with primary applications in critical-dimension (CD) and overlay metrology [23]. While OCD is fast, non-contact, and production compatible, its reliance on intensity-only measurements limits sensitivity to subtle or localized structural variations, and its performance is optimal mainly for periodic targets.

X-RAY AND EUV-BASED TECHNIQUES

X-ray scatterometry and X-ray reflectometry extend metrology capabilities beyond the surface, providing sensitivity to buried interfaces, multilayer stacks, and complex material compositions [26]. They also offer strong sensitivity to thin-film density and roughness. However, these techniques typically require synchrotron or laboratory-scale X-ray sources, involve long acquisition times, and are expensive to integrate into inline environments [27]. Extreme-ultraviolet (EUV) scatterometry, increasingly investigated for advanced nodes, promises enhanced resolution but faces similar constraints in terms of source availability, system complexity, and cost [20, 28].

POSITIONING OF CFS

CFS complements and extends these approaches by exploiting the full optical field, amplitude, phase, polarization, and angular distribution, rather than intensity alone [15]. Its high throughput, non-contact nature, and compatibility with simple optical hardware make it particularly suitable for inline semiconductor metrology. Unlike conventional OCD, CFS can access information about subtle asymmetries, anisotropic material properties, and edge-proximal features. While it does not reach the atomic resolution of SEM or TEM, its combination of sensitivity, speed, and non-destructiveness offers a compelling balance between information content and industrial practicality.

In summary, no single metrology technique satisfies all requirements of advanced semiconductor inspection. Electron and probe-based tools provide ultimate resolution but are slow, costly, and often destructive. X-ray and EUV approaches offer unique subsurface sensitivity but are expensive and complex. Conventional optical tools are fast and non-destructive but limited in sensitivity and information content. CFS bridges these gaps by combining the strengths of optical metrology, speed, non-contact operation, scalability, with richer information access, enabling new capabilities in structural reconstruction, material characterization, and defect inspection.

Table 1.3: Summary of Ph.D. theses on CFS at TU Delft and their key contributions.

Author (Year)	**Focus Area**	**Key Contributions**
N. Kumar (2014) [16]	Sensitivity and overlay	Established theoretical sensitivity gain over IOS; developed first CFS prototype; demonstrated overlay sensitivity and model-based reconstruction.
S. Roy (2016) [17]	Particle detection	Extended CFS to particle inspection; optimized detector geometry, illumination strategies, and evanescent wave amplification for increasing SNR in particle detection; demonstrated sub-100 nm particle detection.
L. Cisotto (2018) [18]	Sidewall angle metrology	Enhanced sensitivity using structured illumination and split detection; introduced pupil optimization methods for CD and sidewall angle retrieval.
D. Kolenov (2022) [29]	Subwavelength detection	Implemented heterodyne detection and explored machine-learning-assisted signal processing and classification.
X. Dou (2024) [30]	Structured-light-assisted retrieval	Developed structured-light-assisted CFS to amplify sensitivity and decouple correlated parameters; demonstrated improved physical parameter retrieval of nanostructures.
S. Soman (2026) [31]	High-throughput scanning strategies for CFS	Developed high-speed and multiplexed CFS architectures using multi-beam and DMD scanning; quantified detection limits and established throughput–sensitivity trade-offs for industrial metrology.

1.2.3. GENESIS AND EVOLUTION OF CFS RESEARCH

The concept of CFS was first formalized around 2011 at Delft University of Technology by Omar El Gawhary *et al.* [15], who demonstrated that coherent illumination combined with Fourier-plane detection could dramatically improve the sensitivity of scatterometry [15]. Early theoretical work showed that CFS could outperform conventional incoherent scatterometry (IOS) in certain parameter regimes and that interference between diffracted orders carried valuable information previously inaccessible to standard OCD.

Building on these foundational insights, the subsequent decade witnessed a sustained and comprehensive research effort at TU Delft, resulting in a mature framework for CFS and its applications. This body of work includes six Ph.D. theses, several postdoctoral projects, and multiple master's and bachelor's theses, each extending the capabilities of CFS in unique directions. Table 1.3 summarizes these doctoral contributions.

1.2.4. STATE OF THE ART BEFORE THIS WORK

By 2022, CFS had matured into a robust and versatile tool for nanoscale optical metrology, demonstrating several major capabilities:

- **High sensitivity to profile parameters:** CFS achieved nanometer-level precision in reconstructing key parameters such as height, critical dimension, and sidewall angle, rivaling SEM and AFM, while remaining non-destructive and scalable [16, 18].
- **Particle and defect inspection:** The technique was extended beyond periodic targets to detect and classify sub-100 nm particles, significantly broadening its inspection capabilities [17, 29].
- **Advanced detection and illumination strategies:** Structured illumination, pupil engineering, and split-detection schemes enhanced sensitivity to subtle geometrical changes and improved parameter separability [18].
- **Structured-light-assisted parameter retrieval:** Tailoring the illumination field to specific parameter sensitivities enabled decoupling of correlated variables and improved reconstruction fidelity [30].

Despite these advances, several key challenges remained unresolved. CFS had not yet been comprehensively applied to non-periodic or highly complex structures, nor had it been optimized for emerging semiconductor challenges such as subsurface metrology, anisotropy characterization, edge-adjacent defect detection, or robust inversion in the presence of strong parameter coupling. Moreover, approaches to selectively enhance informative scattering features while suppressing irrelevant components remained in their infancy.

These limitations defined the starting point for the work presented in this thesis, which aims to push CFS beyond its traditional application domain and address evolving industrial requirements through innovative detection schemes, advanced modeling, and cost-effective implementation strategies.

1.3. MOTIVATION AND RESEARCH QUESTIONS

1.3.1. EVOLVING INDUSTRIAL LANDSCAPE AND UNMET CHALLENGES

While CFS had already demonstrated high sensitivity, flexibility, and strong potential for semiconductor metrology, the landscape of industrial requirements has evolved significantly over the past decade. In addition to advanced semiconductor fabrication, emerging application domains such as power electronics, heterogeneous integration, and fabrication on non-silicon platforms, including glass and polymer substrates, have introduced new metrological demands. Across these areas, rapidly shrinking feature sizes, increasing structural complexity, novel material systems, and ever tighter tolerances pose challenges that traditional scatterometry, and even early implementations of CFS, were not designed to address.

A few of the most pressing trends and challenges include:

- **Complex structures beyond periodic gratings:** Modern device architectures now include quasi-periodic, hierarchical, and 3D structures that deviate significantly from simple line gratings. For such non-periodic structures, the CFS response becomes strongly position-dependent, making probe placement more critical and pushing CFS toward the conceptual boundary with ptychography, where spatial scanning encodes structural information. In parallel, the required structural models grow substantially in complexity, with many more free parameters than in periodic targets, challenging conventional scatterometric analysis.

- **Anisotropic and multifunctional materials:** Emerging materials such as van der Waals crystals, anisotropic oxides, and engineered metasurfaces introduce direction-dependent optical responses. Extracting these anisotropic properties from far-field scattering requires new detection strategies and inversion algorithms.

- **Defects near edges and complex environments:** Traditional scatterometry relies on periodicity and struggles to detect localized defects or particles near edges or buried deep within the wafer, where scattering is strongly influenced by non-periodic boundary conditions or the Fresnel reflections from the top surface.

- **Increased demand for fast, cost-effective solutions:** With the push toward high-volume manufacturing and in-line metrology, there is an increasing need for compact, simple, and computationally efficient metrology tools that can deliver rich information without prohibitive system complexity.

- **Selective information extraction:** As the complexity of scattering responses grows, there is a need for metrology strategies that can selectively enhance the most informative features of the scattered field while suppressing irrelevant or redundant components, improving inversion stability and interpretability.

These challenges reveal a fundamental opportunity: by expanding the measurement capabilities of CFS, both in terms of the type of information collected and the classes of structures analyzed, the technique could be transformed from a specialized tool for periodic structures into a general-purpose optical metrology platform for next-generation surface and nanostructure inspection.

1.3.2. RESEARCH QUESTIONS

The central motivation of this thesis is to advance CFS beyond its traditional application space and adapt it to address emerging challenges in optical metrology. This goal can be distilled into the following key research questions:

1. **How can CFS be extended to inspect complex features and material properties, for anisotropy, near-edge, subsurface, and non-periodic nanostructures, beyond its conventional scope?**
2. **How can numerical modeling and tailored detection schemes be used to extract the most informative scattering features and improve parameter retrieval accuracy?**
3. **How can CFS be implemented as a simple, robust, and cost-effective tool suitable for emerging industrial applications?**

These questions are interconnected. The first focuses on the physical measurement side, identifying what new information is needed and how to access it. The second targets the inversion and interpretation problem, how to maximize the utility of that information through advanced modeling and detection. The third emphasizes practicality, ensuring that the developed techniques are not only scientifically innovative but also industrially relevant.

1.3.3. POSITIONING OF THIS THESIS

This thesis addresses these questions through a combination of theoretical, numerical, and experimental approaches. We explore novel detection concepts (such as quad detection), investigate sensitivity to anisotropic material responses, study scattering from complex and edge-adjacent features, and integrate structured illumination and pupil engineering to improve measurement performance. Throughout, the goal is to push the capabilities of CFS beyond existing boundaries, while maintaining a focus on industrial practicality, simplicity, robustness, and scalability.

1.4. THESIS APPROACH

COMBINING SIMULATION AND EXPERIMENT

Addressing the challenges and research questions outlined above requires a comprehensive approach that integrates both numerical modeling and experimental investigation. A key premise of this thesis is that a deeper understanding of light–matter interaction, particularly in complex scattering scenarios, can only be achieved by tightly coupling theory, simulation, and measurement.

Rigorous electromagnetic simulations play a central role in this work. Methods such as the finite-difference time-domain (FDTD) technique, finite element method (FEM), and rigorous coupled-wave analysis (RCWA) are employed to model the scattering response of nanostructures under different illumination and detection conditions [32–34]. These simulations allow us to:

- Predict how specific structural or material parameters influence the scattered field (amplitude, phase, polarization, and angular distribution).
- Identify which regions of the Fourier plane or which field components carry the most sensitive and least correlated information.

- Explore the effects of structural complexity, edge proximity, anisotropy, and non-periodicity before designing and conducting experiments.

This simulation-guided design enables the experimental implementation to be highly targeted. Rather than measuring the scattered field indiscriminately, the system is optimized to focus on the most informative signals, improving both sensitivity and inversion robustness.

FEATURE SELECTION AND ENHANCEMENT

A central concept in this thesis is the idea of *information-driven metrology*: rather than attempting to capture all scattered light, we aim to selectively enhance those features that carry meaningful structural information while suppressing irrelevant contributions. This is achieved through several complementary strategies:

- **Structured illumination and pupil engineering:** By tailoring the incident field (polarization, wavelength, NA), the system sensitivity to specific parameters (e.g., anisotropy, sidewall angle) can be significantly increased.
- **Advanced detection schemes:** Approaches such as quad detection, polarization-resolved detection, and angle-selective collection help isolate weak but informative scattering signatures.
- **Numerical inversion and filtering:** Combining measured data with forward models allows us to ignore non-essential signal components, reducing cross-sensitivity and improving parameter retrieval accuracy.

Through this feature-focused approach, CFS is transformed from a passive measurement tool into an active metrology platform that interrogates specific physical properties with high precision.

TOWARDS PRACTICAL OPTICAL METROLOGY

Finally, this thesis emphasizes not only scientific innovation but also practical applicability. Each experimental implementation is designed with industrial constraints in mind: simplicity, robustness, speed, and cost-effectiveness. By focusing on compact optical architectures, minimal hardware complexity, and model-based interpretation, we demonstrate how CFS can evolve into a viable solution for in-line semiconductor metrology and inspection.

This combined numerical–experimental methodology forms the backbone of the work presented in the following chapters. It provides both the physical insight and the practical tools required to extend CFS to new application domains, enhance its sensitivity, and adapt it to meet future metrology challenges.

1.5. THESIS OUTLINE

This dissertation is organized into seven core chapters followed by a concluding discussion. Each chapter addresses a distinct aspect of CFS and its applications in advanced optical metrology.

- **Chapter 2**: Inspection of Defects on Patterned Surfaces. This chapter introduces CFS as a sensitive, non-invasive technique for detecting nanoscale defects on patterned surfaces, using diffraction gratings as representative test structures. By combining three-dimensional electromagnetic simulations with experiments, we demonstrate the detection of sub-100 nm particles and common structural defects, positioning CFS as a promising in-line inspection tool for semiconductor manufacturing.

- **Chapter 3**: Inspection of Defects Near Structural Edges. This chapter investigates the challenges of defect detection in the vicinity of structural edges, where strong scattering backgrounds limit conventional split-detection sensitivity. To overcome these limitations, a quad-detection scheme is implemented to capture asymmetries along multiple orientations, enabling robust detection near edges and on arbitrarily oriented features.

- **Chapter 4**: Deep Subsurface Nanostructure Metrology in Silicon. This chapter extends CFS to subsurface inspection of buried nanostructures by operating in the near-infrared regime, leveraging silicon's transparency at these wavelengths. By tailoring source coherence and implementing spatial filtering, interface reflections are suppressed and weak buried signals are enhanced, where high-throughput inspection through silicon up to 500 μm thickness has been demonstrated.

- **Chapter 5**: Dimensional Metrology of Cliff-Like Nanostructures. This chapter presents a metric-driven calibration method for quantifying steep sidewall angles and heights of cliff-like nanostructures. Introducing the "visibility" parameter, this approach directly links far-field scattering signatures to structural dimensions, enabling simplified and robust dimensional metrology without the need for extensive inverse modeling.

- **Chapter 6**: Shape Characterization of Subwavelength Nanostructures. This chapter focuses on lateral shape determination of subwavelength nanopillars with various cross-sectional geometries. By exploiting preferential excitation and rotational symmetry, the method identifies distinct far-field scattering signatures associated with different shapes, demonstrating sub-diffraction-limited shape discrimination and robustness to fabrication imperfections.

- **Chapter 7**: Deep Learning Enabled Anisotropic Optical Characterization of Van der Waals Materials. This chapter explores the use of data-driven methods for optical constant retrieval in anisotropic materials. A deep learning–based framework, AnisoVision, is developed to extract the full refractive index tensor from single-shot CFS measurements using radially polarized illumination. The method is validated on isotropic, uniaxial, and biaxial materials, enabling scalable, high-throughput anisotropy mapping.

- **Chapter 8**: Conclusions and outlook. The final chapter summarizes the main findings of this work and discusses possible research directions for the future of CFS.

BIBLIOGRAPHY

[1] Marc E Himbert. “A brief history of measurement”. In: *The European Physical Journal Special Topics* 172.1 (2009), pp. 25–35. DOI: `10.1140/epjst/e2009-01039-1`.

[2] David Whitehouse. “Metrology Past, Present and Future with Reference to Optics and Manufacture”. In: *Fabrication of Complex Optical Components*. Springer, 2013, pp. 179–206. DOI: `10.1007/978-3-642-33001-8_12`.

[3] W Osten. “Optical metrology: the long and unstoppable way to become an outstanding measuring tool”. In: *Speckle 2018: VII International Conference on Speckle Metrology*. Vol. 10834. SPIE. 2018, p. 1083402. DOI: `10.1117/12.2322533`.

[4] Robert Hooke. *Micrographia: or some physiological descriptions of minute bodies made by magnifying glasses, with observations and inquiries thereupon*. Printed by J. Martyn and J. Allestry, 1665.

[5] Henry Baker. “IX. An account of Mr. Leeuwenhoek’s microscopes”. In: *Philosophical Transactions of the Royal Society of London* 41.458 (1739), pp. 503–519. DOI: `10.1098/rstl.1739.0085`.

[6] Antoni van Leeuwenhoek and Samuel Hoole. *The select works of anthony van leeuwenhoek: containing his microscopical discoveries in many of the works of nature*. Vol. 1. London : G. Sidney, 1800.

[7] Ernst Abbe. “Beiträge zur Theorie des Mikroskops und der mikroskopischen Wahrnehmung”. In: *Archiv für mikroskopische Anatomie* 9.1 (1873), pp. 413–468. DOI: `10.1007/BF02956173`.

[8] Adam JM Wollman et al. “From Animaculum to single molecules: 300 years of the light microscope”. In: *Open Biology* 5.4 (2015), p. 150019. DOI: `10.1098/rsob.150019`.

[9] Katherine Creath and Robert E Parks. “Optical metrology at the Optical Sciences Center: an historical review”. In: *Fifty Years of Optical Sciences at The University of Arizona*. Vol. 9186. SPIE. 2014, pp. 277–290. DOI: `10.1117/12.2064376`.

[10] GD Burdun. “On the new determination of the meter”. In: *Measurement Techniques* 1.3 (1958), pp. 259–264. DOI: `10.1007/BF00974680`.

[11] Peter de Groot. “Optical metrology”. In: *The Optics Encyclopedia, edited by TG Brown, et al* (2004), pp. 2085–2117.

[12] Fritz Riehle. “Towards a redefinition of the second based on optical atomic clocks”. In: *Comptes Rendus. Physique* 16.5 (2015), pp. 506–515. DOI: `10.1016/j.crhy.2015.03.012`.

[13] Rajpal S Sirohi. *Introduction to optical metrology*. CRC press, 2017. DOI: 10.1201/9781315215228.

[14] Christopher J Raymond. "Milestones and future directions in applications of optical scatterometry". In: *Optical Metrology: A Critical Review*. Vol. 10294. SPIE. 1999, pp. 124–154. DOI: 10.1117/12.351670.

[15] O El Gawhary et al. "Performance analysis of coherent optical scatterometry". In: *Applied Physics B* 105.4 (2011), pp. 775–781. DOI: 10.1007/s00340-011-4794-7.

[16] Nitish Kumar. "Coherent Fourier scatterometry". PhD thesis. Delft University of Technology, 2014. DOI: https://doi.org/10.4233/uuid:94b3ec33-cf29-4704-a277-e3029b2e211f.

[17] Sarathi Roy. "Sub-wavelength metrology using coherent Fourier scatterometry". PhD thesis. Delft University of Technology, 2016. DOI: https://doi.org/10.4233/uuid:234cb48f-62b3-41e7-bde0-04f0186f52f6.

[18] Luca Cisotto. "Optimisation of coherent Fourier scatterometry for side wall angle estimation of printed structures". PhD thesis. Delft University of Technology, 2018. DOI: https://doi.org/10.4233/uuid:acc326db-752b-4dcd-9672-5e208cd6285e.

[19] Jinlong Zhu et al. "Optical wafer defect inspection at the 10 nm technology node and beyond". In: *International Journal of Extreme Manufacturing* 4.3 (2022), p. 032001. DOI: 10.1088/2631-7990/ac64d7.

[20] Elisabeth Mansfield et al. *International Roadmap for Devices and Systems^{TM} 2023 Edition Metrology*. 2023. URL: https://irds.ieee.org/editions/2023.

[21] Carl Georg Frase, Egbert Buhr, and Kai Dirscherl. "CD characterization of nanostructures in SEM metrology". In: *Measurement Science and Technology* 18.2 (2007), p. 510. DOI: 10.1088/0957-0233/18/2/S26.

[22] Nan Jiang. "On the limitation of quantitative measurements using transmission electron microscopy". In: *Journal of Non-crystalline Solids* 358.1 (2012), pp. 119–123. DOI: 10.1016/j.jnoncrysol.2011.09.004.

[23] Yan Li and Deepak Goyal. *3D Microelectronic packaging: from architectures to applications*. Vol. 64. Springer Nature, 2020. DOI: 10.1007/978-981-15-7090-2.

[24] Danish Hussain et al. "Advances in the atomic force microscopy for critical dimension metrology". In: *Measurement Science and Technology* 28.1 (2016), p. 012001. DOI: 10.1088/0957-0233/28/1/012001.

[25] M Erman and JB Theeten. "Spatially resolved ellipsometry". In: *Journal of Applied Physics* 60.3 (1986), pp. 859–873. DOI: 10.1063/1.337327.

[26] C Schmidt. "3-D X-Ray imaging with nanometer resolution for advanced semiconductor packaging FA". In: *IEEE Transactions on Components, Packaging and Manufacturing Technology* 8.5 (2018), pp. 745–749. DOI: 10.1109/TCPMT.2018.2827058.

[27] Dalia Yablon. *Metrology capabilities keep up with semiconductor industry push into 3D integrated circuits (Part 1)*. 2024. URL: https://analyticalscience.wiley.com/content/article-do/metrology-capabilities-keep-%E2%80%A8up-semiconductor-industry-push-into-3d-integrated-circuits.

[28] H Gross et al. “Profile reconstruction in extreme ultraviolet (EUV) scatterometry: modeling and uncertainty estimates”. In: *Measurement Science and Technology* 20.10 (2009), p. 105102. DOI: 10.1088/0957-0233/20/10/105102.

[29] Dmytro Kolenov. “Coherent Fourier scatterometry for sensitive detection of subwavelength structures and particles”. PhD thesis. Delft University of Technology, 2022. DOI: https://doi.org/10.4233/uuid:c189b14b-c454-4f13-8658-5c6210bb652e.

[30] Xiujie Dou. “Structured light assisted coherent Fourier scatterometry for physical parameter retrieval of nanostructures”. PhD thesis. Delft University of Technology, 2024. DOI: https://doi.org/10.4233/uuid:2ac46a6e-c97a-495a-b9d3-f65ec8c7cf2b.

[31] Sarika Soman. “High-speed coherent Fourier scatterometry”. PhD thesis. Delft University of Technology, 2026. DOI: https://doi.org/10.4233/uuid:88cd1453-8898-4b1d-9963-5edf36b9c758.

[32] Dennis M Sullivan. *Electromagnetic simulation using the FDTD method*. John Wiley & Sons, 2013. DOI: 10.1002/9781118646700.

[33] Junuthula Narasimha Reddy. *An introduction to the finite element method*. 2nd ed. New York: McGraw-Hill, 1993.

[34] M. G. Moharam and T. K. Gaylord. “Rigorous coupled-wave analysis of planar-grating diffraction”. In: *Journal of the Optical Society of America* 71.7 (1981), pp. 811–818. DOI: 10.1364/JOSA.71.000811.

2

INSPECTION OF DEFECTS ON PATTERNED SURFACES

This chapter presents coherent Fourier scatterometry (CFS) as a sensitive, non-destructive technique for detecting nanoscale defects on patterned surfaces, using diffraction gratings as representative structures. Through 3D FDTD simulations and experiments, we demonstrate detection of tungsten and platinum particles down to ~ 100 *nm and identification of structural defects such as bridges, breaks, and line collapses. These results establish CFS as a promising in-line metrology tool for inspecting periodic and non-periodic nanostructures in advanced semiconductor manufacturing.*

Parts of this chapter have been published in Applied Optics **62**(29), 7589 (2023) [1].

The presence of nanoscale defects on patterned surfaces remains one of the most critical challenges in advanced optical and semiconductor technologies. Even a single contaminant particle or structural imperfection can compromise device performance or yield, particularly as feature dimensions approach the deep-subwavelength regime. Diffraction gratings are one such patterned surface, which is an integral component in a wide range of optical technologies, including spectroscopy [2, 3], spectral beam combining [4, 5], chirped pulse compression [6–8], and photonic integration [9]. Despite advances in nanofabrication that enable precise grating geometries [10], nanoscale contaminants or structural defects introduced during manufacturing can significantly degrade performance, for example by reducing diffraction efficiency or altering spectral response [11–13]. Detecting such subtle imperfections is increasingly critical as device dimensions continue to shrink.

Traditional inspection techniques such as scanning electron microscopy (SEM) [14] and atomic force microscopy (AFM) [15] provide excellent spatial resolution but are slow, invasive, and unsuitable for in-line operation. Bright-field microscopy offers higher throughput but is diffraction-limited [16–19], while advanced approaches such as stochastic optical reconstruction microscopy (STORM) [20] require fluorescent labeling, limiting industrial applicability. Conventional optical scatterometry offers a non-destructive, model-based solution but is typically restricted to retrieving small deviations from nominal profile parameters and shows limited sensitivity to isolated nanoscale defects.

Coherent Fourier scatterometry (CFS) addresses these limitations by exploiting the full optical field in the Fourier plane [21–24]. Its coherent illumination enhances sensitivity to weak scattering perturbations, while the use of a split-detection scheme further improves sensitivity, enabling reliable detection of nanoparticles and subtle structural variations without labeling. Moreover, CFS is compatible with large-area scanning and industrial inspection workflows.

This chapter explores the application of CFS for detecting nanoscale defects on patterned surfaces, using periodic diffraction gratings as model systems. We investigate both particle contamination and structural defects such as bridges, breaks, indentations, and line collapses through a combination of rigorous three-dimensional electromagnetic simulations and experimental measurements.

2.1. METHODS

2.1.1. THEORY

In this section, we introduce the diffraction theory of a grating for CFS. In Fig. 2.1(a) the geometrical representation of a periodic 1D grating interacting with a focused beam is illustrated. The grating is defined by the geometrical parameters: period (p), line width (w), height (h), side wall angle (swa, defined as the angle between the wall of the grating line and the surface plane of the sample), and bias (b). b is a parameter that is introduced to define the relative position of the grating to the optical axis of the focused beam. Although the definition of the position $b = 0$ can be arbitrary, we define it as the position when the optical axis of the focused beam bisects the w i.e., the position $x = 0$ as indicated in Fig. 2.1(a). We introduce a coordinate system (x, y, z) to define the grating geometry, with $x-$axis being parallel to the grating vector ($\vec{g}$), $y-$axis being perpendicular

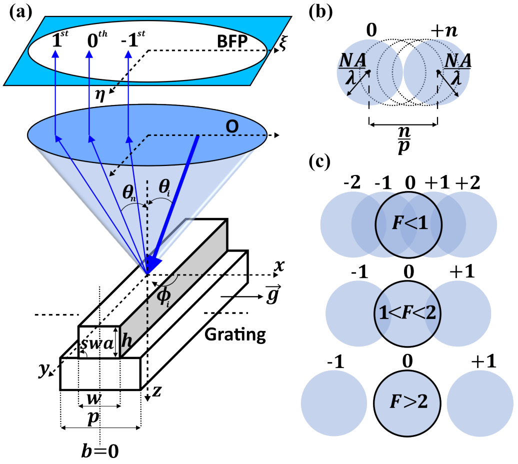

Figure 2.1: (a) Schematic representation of a 1D periodic grating, having coordinate system (x, y, z), diffracting an incident beam into multiple orders. The diffracted beams are collected by an objective lens (O) having numerical aperture (NA) and propagated to the back focal plane (BFP), having coordinate system (ξ, η). (b) Condition of overlap between 0^{th} order and $+n^{th}$ order (having radius NA/λ), separated by distance n/p in the back focal plane. The same applies to $-n^{th}$ order. (c) Effect of overlap parameter (F), on the back focal plane of the objective lens (represented with black circles).

to the grating vector, and $z-$axis being parallel to the optical axis of the focused beam. Using angular spectrum representation formalism we can conceive a focused beam to be an expansion of an infinite number of plane waves of different propagation directions [25]. Let us consider one such instance of the plane wave, incident on the grating by the polar angle θ_i and azimuthal angle ϕ_i. The grating diffracts the incident beam into multiple different directions as 0^{th} order, $\pm 1^{th}$ order, and higher orders. The angle of propagation for the n^{th} diffraction order is given by grating's law,

$$\sin\theta_i + \sin\theta_n = n\lambda/p, \tag{2.1}$$

where λ is the wavelength of the incident plane wave. The diffracted orders are collected by an objective lens (O) having numerical aperture (NA) and mapped to the back focal plane (BFP) based on the Fourier optics theory. The BFP is in the Fourier space with the coordinate system (ξ, η), where ξ and η are parallel to x and y, respectively. Now, if we consider the diffraction from the grating for all the plane waves, each θ_i and ϕ_i will be mapped to a different point in the BFP i.e., the (ξ, η) plane. This mapping is limited by the NA of the objective lens. This results in each order being mapped as a circle of radius NA/λ, separated by a distance n/p in the BFP, where n is the diffraction order, as shown in Fig. 2.1(b). Now, any order is said to overlap if it follows the condition,

$$\frac{n}{p} \leq \frac{2\text{NA}}{\lambda}. \tag{2.2}$$

Further, the amount of overlap between the diffracted orders in the BFP is defined by the overlap parameter (F) as [26],

$$F = \frac{\lambda}{\mathrm{NA} \times p}. \tag{2.3}$$

In Fig. 2.1(c), we have shown the effect of F, on the BFP of the objective lens. When $F > 2$ there is no overlap between the orders i.e., all the higher orders are not collected by the objective lens. When $1 < F < 2$, there is an overlap between $0, \pm 1$ orders but no overlap between ± 1 orders is observed. Finally, when $F < 1$, there is overlap between even more diffracted orders.

2.1.2. EXPERIMENTAL SETUP

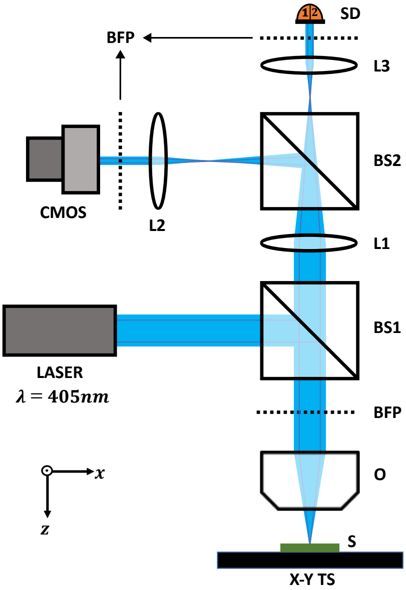

Figure 2.2: Schematic of the experimental setup of coherent Fourier scatterometry (CFS).

Here, the experimental configuration of the CFS setup, schematically illustrated in Fig. 2.2, is employed to perform the measurements in this chapter, where a collimated and linearly polarized laser ($\lambda = 405$ nm) source is applied for illumination. The collimated beam from the laser passes through a non-polarizing beam splitter (BS1) which further travels to a high NA microscope objective (O) (NA = 0.9) and is focused on the Si grating sample (S). In the experiment, we can use any arbitrary linear polarization state for the measurements. The sample is placed on a piezo translation stage (X-Y TS), with the grating vector ($\vec{g}$) parallel to the horizontal (typically wider) scan direction (x). The translation stage can be laterally scanned in a serpentine pattern. The diffracted light from the grating is collected back by the microscope objective (O) and passes through the non-polarizing beam splitter (BS1) again. A telescopic setup consisting of two lenses (L1 and L2/ L3) is added to de-magnify the Fourier plane of the objective to a split detector (SD). In this way, the angular spectrum for all diffracted waves is detected at once for all incident plane waves within the focused spot determined by the NA of the system. A complementary metal-oxide-semiconductor (CMOS) camera is added in the back focal plane (BFP) of the microscope objective (O) with the help of a second non-polarizing beam splitter (BS2) to localize the region of interest in the sample.

The split detector consists of two pixels aligned perpendicular to the scan direction, and the intensity from one pixel is subtracted from the other. As a result, any specular reflections (such as the case for gratings with $F > 2$) and noise in the system are eliminated and we observe the differential signal to be nearly zero. As the focused beam is scanned through a grating structure i.e., bias (b) is increased from 0 to period (p), for gratings with $F < 2$, the far field signature becomes asymmetric and we observe a position-dependent differential signal. This position-dependent differential signal will repeat periodically if scanned through a large number of periods across the grating sample i.e., the obtained differential signal is scan invariant.

2.1.3. NUMERICAL MODEL

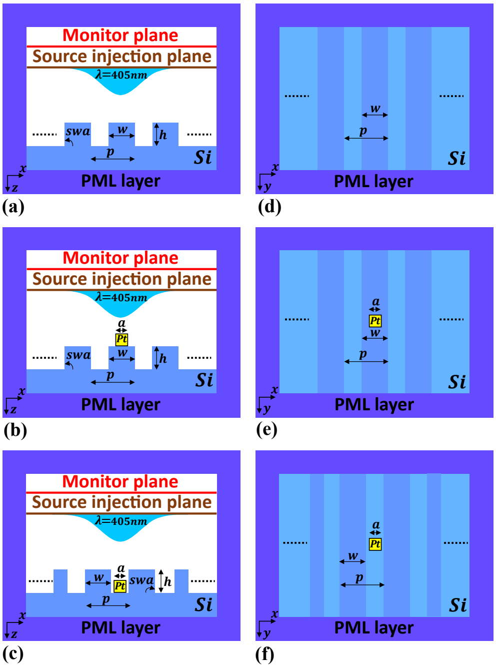

Figure 2.3: The 3D-FDTD simulation scheme of a grating with and without an isolated particle at different positions (shown for bias position $b = 0$). The corresponding $y = 0$ plane in (a),(b), and (c). The corresponding $z = 0$ plane in (d),(e), and (f).

To understand the interaction of a focused beam with an isolated particle present in a grating we need to perform accurate rigorous electromagnetic modeling. The electromagnetic problem of the interaction of a 1D grating illuminated by a focused beam has been studied using well-known rigorous coupled-wave analysis RCWA [26, 27], which is acclaimed for applications in periodic dielectric structures. In our case, we have an aperiodic scatterer i.e., a particle, on a periodic background i.e., a grating. In order to treat this problem, we utilized rigorous 3D electromagnetic simulations, the finite difference time domain (3D-FDTD) method, using a commercial software package (Lumerical FDTD) [28]. In FDTD simulations, Maxwell's equations are solved in discretized Yee grids (i.e., spatial and temporal grids) in the time domain.

To mimic the experimental conditions, we model multiple periods (nine periods for this case) of the grating with and without the isolated particle at different positions (i.e., the particle is present on top of the groove (line), and the particle is present on top of the substrate of the grating), as the simulation object. We determine the number of periods of the grating in the simulation object such that the width of the focused beam (FWHM$\sim$ 302 nm) is smaller than the dimension of the simulation object ($\sim$ 7.128 µm). We implement perfectly matched layer (PML) boundary conditions to all the boundaries. The illumination scheme is defined as that of a TE polarized (i.e., the polarization direction at the pupil is parallel to the grating lines) plane wave of wavelength $\lambda = 405$ nm being focused by a high NA (=0.9) microscope objective onto the simulation object [29]. This choice of illumination scheme provides a well-defined and controlled excitation, which is necessary for accurately solving Maxwell's equations and understanding the scattering response. In contrast, the experimental system operates under a general polarization state, where precise alignment is not required for defect detection. The diffracted near field from the sample is computed and sampled at the monitor plane and propagated to the far field in the FDTD simulation using Lumerical FDTD's inbuilt near-to-far field transformation (NFFT), where the computed near field is decomposed into spherical waves emanating from the sampled grids (point sources) of the monitor plane. By using Green's theorem, the radiating spherical waves at a specific distance from the monitor plane can be integrated to produce the far field signatures [30].

In Fig. 2.3(a-c), the $y = 0$ plane, while in Fig. 2.3(d-f), the $z = 0$ plane of the full 3D-FDTD model is shown (for bias position, $b = 0$). The simulation object's geometry is defined by the parameters, period (p), line width (w), height (h), side wall angle (swa), bias (b), and particle dimension (a). The grating and particle materials are Si ($n = 5.4254 + 0.3309i$) and Pt ($n = 1.7317 + 2.8713i$), respectively, for the wavelength $\lambda = 405$ nm. To simulate scanning effects, we change b and we shift the simulation object along $x-$axis keeping the position of the source injection plane, monitor plane, and computational domain constant.

2.1.4. SAMPLE PREPARATION/ DEPOSITION METHOD

Table 2.1: Geometrical parameters of the diffraction grating.

Grating parameters	**Nominal values**
Period (p)	792 nm
Line width (w)	396 nm
Height (h)	150 nm
Side wall angle (swa)	90°

Grating sample with geometrical parameters as detailed in Table 2.1 served as the substrate for particle deposition and subsequent measurements. Particle deposition is performed via electron beam induced deposition (EBID) with FEI FIB/SEM Helios G4 CX. Nominal sizes are 100 × 100 × 100 nm tungsten (W) and platinum (Pt) particles deposited on period 792 nm diffraction grating. Same settings were used: 5 kV acceleration voltage, 1.3 pA beam current, 200 ns dwell time, −90% overlap, 0.05 μm^3/nC volume per dose. For the W material transverse size of the resulting particles according to SEM image is ≈ 130 nm and for Pt particles ≈ 115 nm. The SEM measurements of the tilted plane grating with the particles deposited were not conclusive and it is not possible to report the height of the final structures. It is our observation for the deposition of similar particles directly on silicon wafers that the height of the resulting structures is less than the nominal structure. Also, the nominal size particles we deposited are lacking definition effectively being not a cube but rather bumps of material.

2.2. RESULTS

2.2.1. PARTICLE IN A PERIODIC GRATING: NUMERICAL STUDY

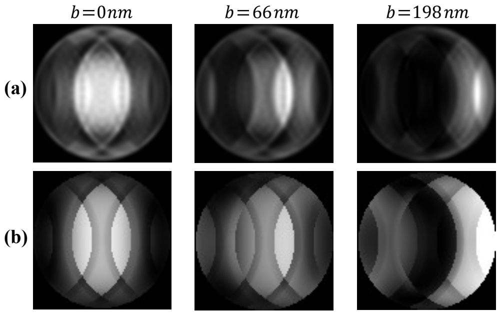

Figure 2.4: The far field signatures for different bias positions (b = 0 nm, 66 nm, 198 nm) of a Si grating (without particle) of period (p) = 792 nm, line width (w) = $p/2$, height (h) = 150 nm, illuminated by a TE polarized focused beam of wavelength (λ) = 405 nm. (a) Simulated using 3D-FDTD scheme; (b) Simulated using RCWA.

In this section, we perform a numerical study on the influence of an isolated particle on the far field signatures of the diffraction grating. The primary objective of this numerical study is to provide a valuable tool for enhancing our understanding and interpretation of experimental results. Experimental data can often be intricate and challenging to interpret directly, making these simulations particularly valuable in aiding comprehension. As discussed earlier we are modeling an infinite periodic structure (a grating) as a finite non-periodic structure. Thus, we need to verify that our simulation model is faithful. We compare our simulated far field signatures with that of a semi-analytical method (RCWA), for the case where there is no defect/particle present on the grating. In Fig. 2.4(a) we have shown the far field signatures of the 3D-FDTD simulations performed without the presence of a particle (as shown in Fig. 2.3(a) and (d)) corresponding to the different bias positions (b = 0 nm, 66 nm, 198 nm) within a single period for a Si grating with geometrical parameters as mentioned in Table 2.1. In Fig. 2.4(b) the corresponding far field signatures obtained from RCWA have been shown. As for both the simulation methods the far field signatures are consistent, we establish that our model describes the phenomena satisfactorily.

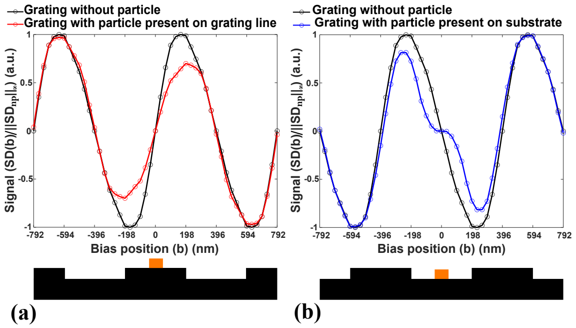

Figure 2.5: Simulated differential scan signal of a Si grating (geometrical parameters described in Table 2.1) (a) with particle (dimension $a = 100$ nm) present on grating line (represented by the red curve) and without particle (represented by the black curve), with the representation of the scanned region and the position of the particle (shown in orange); (b) with particle (dimension $a = 100$ nm) present on the grating substrate (represented by the blue curve) and without particle (represented by the black curve), with the representation of the scanned region and the position of the particle (shown in orange).

Now, to simulate the scanning of the grating with and without the isolated particle, we add a platinum (Pt) particle in the shape of a cube with dimension $(a) = 100$ nm in the simulation object of the grating. We consider two such cases: first, when the particle is present on top of the groove (line) of the grating (as shown in Fig. 2.3(b) and (e)), and second, when the particle is present on top of the substrate of the grating (as shown in Fig. 2.3(c) and (f)). We perform a scan by changing the bias $b(= 0$ to $p)$ across a period with a scan step of 33 nm, with the center of the particle at the position $b = 0$ for both cases. As the bias position $b = 0$, represent the axis of symmetry for which the grating is reflection symmetric i.e., bias $-b$ is equivalent to the mirror image of bias b, consequently, the far field signatures are also mirror images. Therefore, we obtain the far field signatures for scan positions $b = -p$ to p. For all the scan positions we calculate the split-detector differential signal of the far field signatures. Mathematically, this can be described as

$$SD(b) = \sum_{n_1=1}^{N/2} \sum_{n_2=1}^{N} I_{n_1,n_2}(b) - \sum_{n_1=N/2+1}^{N} \sum_{n_2=1}^{N} I_{n_1,n_2}(b), \tag{2.4}$$

where I_{n_1,n_2} is the far field signatures at the (n_1, n_2)th pixel, with N^2 being the total number of pixels in the square far field plane. In Fig. 2.5(a), the differential signal of the scan for the first case (represented by the red curve) along with the differential signal when the particle is absent (represented by the black curve) is plotted. Consequently in Fig. 2.5(b), the differential signal of the scan for the second case (represented by the blue curve) along with the differential signal when the particle is absent (represented by the black curve) is plotted. The depiction of the scanned region has been shown below in both the plots of Fig. 2.5. The scan signal in each case is normalized to the respective scenario in the absence of the particle, such that $signal = SD(b)/||SD_{np}||_\infty$. The cumulative change in the signal (c) can be calculated with, $c = \sum|signal_{np} - signal_{wp}|$, where the indices np and wp means the case of no particle and with particle, respectively. In case of modeled scenario of $swa = 90°$ when the particle is present on top of the substrate of the grating, the change is $c_{swa=90°} = 6.61$ and it drops slightly when the swa parameter is varied $c_{swa=85°} = 6.52$, $c_{swa=80°} = 6.55$. For the case when the particle is present on top of the grooves (lines), the change is $c_{swa=90°} = 5.18$ and it increases when the swa parameter is varied $c_{swa=85°} = 6.00$, $c_{swa=80°} = 5.90$. The simulated results in Fig. 2.5 indicate that the presence of an isolated particle on the grating affects the far field signatures by reducing the differential signals near the vicinity of the particle irrespective of the position of the particle on the groove (line) or substrate. But in the absence of a particle, we measure the differential signal repeating itself as we scan through the grating. These results demonstrate that this technique can detect isolated particles present on a grating.

2.2.2. PARTICLE IN A PERIODIC GRATING: EXPERIMENTAL STUDY

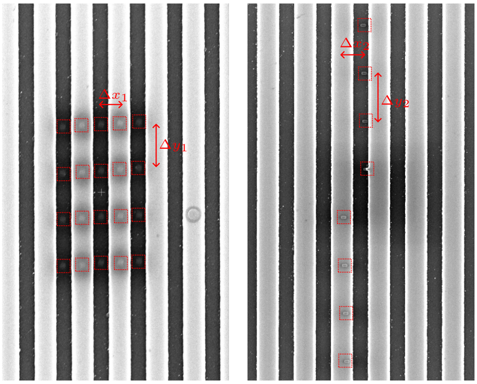

$\Delta x_1 = 0.44\,\mu m$; $\Delta y_1 = 1\,\mu m$
(a)

$\Delta x_2 = 0.378\mu m$; $\Delta y_2 = 2\mu m$
(b)

Figure 2.6: SEM images of a deposition of array of (a) 4 × 5 tungsten (W) particles (in shape of cube 100 × 100 × 100 nm); (b) 8 × 1 platinum (Pt) particles (in shape of cube 100 × 100 × 100 nm) on a Si grating (period $p = 792$ nm, line width $w = p/2$, height $h = 150$ nm, and side wall angle $swa = 90°$) using using electron beam induced deposition (EBID). The locations of the deposited particles are marked using dashed-cubes for better visualization.

In this section, we demonstrate the experimental measurements using CFS to detect particles present on a diffraction grating structure. For that, we have deposited an array of 4 × 5 tungsten (W) particles (in the shape of cube 100 × 100 × 100 nm) and an array of 8 × 1 platinum (Pt) particles (in shape of cube 100 × 100 × 100 nm) on a Si grating (period $p = 792$ nm, line width $w = p/2$, height $h = 150$ nm, and side wall angle $swa = 90°$) using electron beam induced deposition (EBID). In Fig. 2.6 we show the SEM images of the grating where the particles are deposited.

The experimental setup of CFS as depicted in Fig. 2.2 has been used for data collection. Here we illuminate the grating sample using a linearly polarized focused spot using a high NA=0.9 microscope objective, with the polarization in an arbitrary orientation. The grating sample is placed on the piezo translation stage with the grating vector ($\vec{g}$) being parallel to scan direction (x). The diffracted field is captured by the split-detector and the

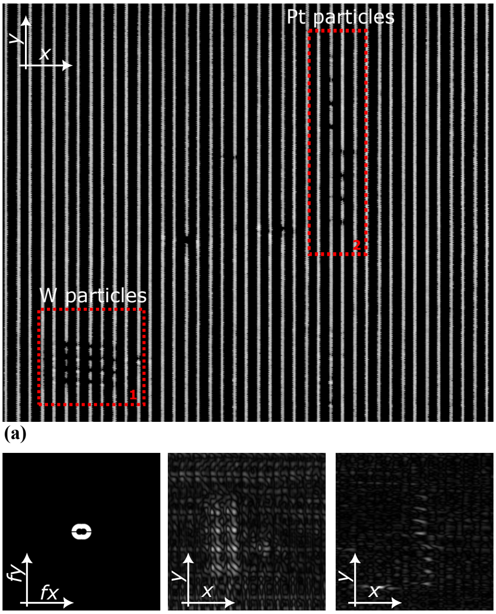

(a)

(b) (c) (d)

Figure 2.7: (a) CFS mapped data where the W (shown within dashed region 1) and Pt (shown within dashed region 2) particles are deposited, highlighting the change in the periodic differential signal due to the particles. (b) *ad hoc* Fourier filter used to remove the background signals. (c) CFS mapped data after filtering the background signals, where the array of W particles can be clearly seen. (d) CFS mapped data after filtering the background signals, where the array of Pt particles can be clearly seen.

position-dependent differential signal is recorded. Now, the change in the signal in the vicinity of a particle is a reduction in the peak-to-peak value of the periodic differential signal as also discussed earlier. We can use this property, and by highlighting this change in the differential signal, we can improve the visualization of the detected particles. In Fig. 2.7(a) we have shown the CFS mapped data in the region where particles are deposited. Here, the breaks in the solid line indicate the presence of a particle. With the array of 4×5 W particles shown within the dashed region 1 and the array of 8×1 Pt particles shown within the dashed region 2. The shown CFS mapped data is rotated by an angle 1.8°, as the grating sample is placed on the piezo translation stage manually, and we cannot place the grating vector ($\vec{g}$) exactly parallel to the scan direction.

Now, we define the signal-to-noise ratio (SNR) as,

$$SNR_{dB} = 10\log_{10}\frac{P_{signal}}{P_{noise}}. \tag{2.5}$$

Here, P_{signal} is the power of the signal, and P_{noise} is the power of the noise. Now, to calculate the SNR our task reduces to separating out the signal due to the particle only, without the periodic background signal. To tackle this problem, we Fourier transform our data to the frequency domain and filter out the frequencies due to the background structure. This can be done for periodic structures like grating where the frequencies of the background are located along the axes parallel to the direction of the grating vector ($\vec{g}$). We use a combination of rectangular and circular filters to eliminate the background frequencies due to the periodic grating as well as the noise and inverse-Fourier transform it back to the spatial domain, as shown in Fig. 2.7(b). However, it should be noted that the filter used is *ad hoc* and cannot be generalized just yet. From this Fourier filtering step, a significant contrast between the scattering of the structure and the scattering of the particle is achieved, making the problem analogous to particle detection on a plane substrate. In Fig. 2.7(c) and (d), we have shown the CFS mapped data after using the filter for an array of 4 × 5 W particles, and an array of 8 × 1 Pt particles, respectively. We can observe that the background from Fig. 2.7(a) is minimized and we can distinguish the particles. The SNR is 7.24 dB.

2.2.3. EXTRA DEFECTS

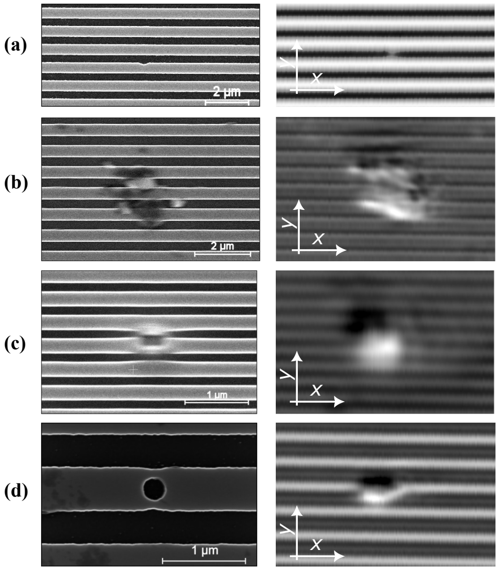

Figure 2.8: SEM images (in the left) and the corresponding CFS mapped data (in the right) for various defect types in Si grating (a) a break defect ($p = 792$ nm); (b) a bridge defect ($p = 792$ nm); (c) a line collapse defect ($p = 378$ nm); (d) an indentation defect ($p = 918$ nm). For visual clarity, the SEM and CFS panels are shown with different field-of-view scaling; however, each pair corresponds to the same grating pitch and defect.

In this section, we demonstrate the capabilities of CFS to detect different types of defects usually encountered in diffraction gratings. Some of the most common defects in diffraction gratings are break defects, indentation defects, bridge defects, and line collapse defects [31]. We identify and locate these defects in Si gratings with periods $p = 378$ nm, 792 nm, 918 nm, having line width $w = p/2$, height $h = 150$ nm, side wall angle $swa = 90°$. In Fig. 2.8(a), we have shown a break defect in Si gratings with period $p = 792$ nm using SEM and the corresponding CFS mapped data. In Fig. 2.8(b), we have shown a bridge defect in Si grating with period $p = 792$ nm using SEM and the corresponding CFS mapped data. In Fig. 2.8(c), we have shown a line collapse defect in Si grating with period $p = 378$ nm using SEM and the corresponding CFS mapped data. In Fig. 2.8(d), we have shown an indentation defect in Si grating with period $p = 918$ nm using SEM and the corresponding CFS mapped data. From the following study, we have demonstrated that CFS is a viable tool that can be used to detect different types of defects encountered in diffraction gratings.

2.3. SUMMARY

In this chapter, we demonstrated coherent Fourier scatterometry (CFS) as an effective technique for inspecting diffraction gratings and detecting nanoscale defects. Three-dimensional FDTD simulations were performed to investigate the impact of isolated particles on the far-field differential signal, showing a localized signal reduction near the defect, independent of its position. Experimental validation confirmed the subwavelength detection of tungsten and platinum particles as small as $\sim$ 100 nm on gratings with a 792 nm period using a wavelength of 405 nm. The use of Fourier filtering was shown to enhance the SNR to 7.24 dB by suppressing background periodic signals. Furthermore, CFS successfully identified common structural defects such as bridges, breaks, and line collapses. Despite sensitivity to alignment tolerances, the results establish CFS as a promising, non-destructive, in-line metrology tool for patterned nanostructures.

BIBLIOGRAPHY

[1] Anubhav Paul et al. “Coherent Fourier scatterometry: a holistic tool for inspection of isolated particles or defects on gratings”. In: *Applied Optics* 62.29 (2023), pp. 7589–7595. DOI: `10.1364/AO.503350`.

[2] Luo Biao and Zhi-yu Wen. “Design and experiment of spectrometer based on scanning micro-grating integrating with angle sensor”. In: *Infrared Physics & Technology* 62 (2014), pp. 29–33. DOI: `10.1016/j.infrared.2013.09.010`.

[3] AN Shatokhin et al. “High-resolution stigmatic spectrograph for a wavelength range of 12.5–30 nm”. In: *Optics Express* 26.15 (2018), pp. 19009–19019. DOI: `10.1364/OE.26.019009`.

[4] Jun Zhang et al. “CW 50W/M2 = 10.9 diode laser source by spectral beam combining based on a transmission grating”. In: *Optics Express* 21.3 (2013), pp. 3627–3632. DOI: `10.1364/OE.21.003627`.

[5] Deepak Vijayakumar et al. “Spectral beam combining of a 980 nm tapered diode laser bar”. In: *Optics Express* 18.2 (2010), pp. 893–898. DOI: `10.1364/OE.18.000893`.

[6] Donna Strickland and Gerard Mourou. “Compression of amplified chirped optical pulses”. In: *Optics Communications* 56.3 (1985), pp. 219–221. DOI: `10.1016/0030-4018(85)90120-8`.

[7] Lukas Stankevičius et al. “Diffraction efficiency optimization of multilayer dielectric mirror-based gratings for 1030nm femtosecond lasers”. In: *Optics & Laser Technology* 126 (2020), p. 106071. DOI: `10.1016/j.optlastec.2020.106071`.

[8] Wenfei Zhang et al. “Review of pulse compression gratings for chirped pulse amplification system”. In: *Optical Engineering* 60.2 (2021), p. 020902. DOI: `10.1117/1.OE.60.2.020902`.

[9] Kun Yin et al. “Advanced liquid crystal devices for augmented reality and virtual reality displays: principles and applications”. In: *Light: Science & Applications* 11.1 (2022), p. 161. DOI: `10.1038/s41377-022-00851-3`.

[10] Ye Wang et al. “The Development Progress of Surface Structure Diffraction Gratings: From Manufacturing Technology to Spectroscopic Applications”. In: *Applied Sciences* 12.13 (2022), p. 6503. DOI: `10.3390/app12136503`.

[11] Nan Liu et al. “Manufacturing-induced contamination in common multilayerdielectric gratings”. In: *Optics Express* 31.1 (2023), pp. 714–726. DOI: `10.1364/OE.478701`.

[12] Luis Miguel Sanchez-Brea and Francisco Jose Torcal-Milla. “Near-field diffraction of gratings with surface defects”. In: *Applied Optics* 49.11 (2010), pp. 2190–2197. DOI: `10.1364/AO.49.002190`.

[13] Jinlong Zhu et al. "Optical wafer defect inspection at the 10 nm technology node and beyond". In: *International Journal of Extreme Manufacturing* 4.3 (2022), p. 032001. DOI: `10.1088/2631-7990/ac64d7`.

[14] András E. Vladár and Vasile-Dan Hodoroaba. "Chapter 2.1.1 - Characterization of nanoparticles by scanning electron microscopy". In: *Characterization of Nanoparticles*. Ed. by Vasile-Dan Hodoroaba, Wolfgang E.S. Unger, and Alexander G. Shard. Micro and Nano Technologies. Elsevier, 2020, pp. 7–27. DOI: `10.1016/B978-0-12-814182-3.00002-X`.

[15] Ernst Meyer. "Atomic force microscopy". In: *Progress in Surface Science* 41.1 (1992), pp. 3–49. DOI: `10.1016/0079-6816(92)90009-7`.

[16] Ernst Abbe. "Beiträge zur Theorie des Mikroskops und der mikroskopischen Wahrnehmung". In: *Archiv für mikroskopische Anatomie* 9.1 (1873), pp. 413–468. DOI: `10.1007/BF02956173`.

[17] Oguzhan Avci et al. "Interferometric reflectance imaging sensor (IRIS)—A platform technology for multiplexed diagnostics and digital detection". In: *Sensors* 15.7 (2015), pp. 17649–17665. DOI: `10.3390/s150717649`.

[18] Jacob T Trueb et al. "Robust visualization and discrimination of nanoparticles by interferometric imaging". In: *IEEE Journal of Selected Topics in Quantum Electronics* 23.2 (2016), pp. 394–403. DOI: `10.1109/JSTQE.2016.2639824`.

[19] Jaime Ortega-Arroyo and Philipp Kukura. "Interferometric scattering microscopy (iSCAT): new frontiers in ultrafast and ultrasensitive optical microscopy". In: *Physical Chemistry Chemical Physics* 14.45 (2012), pp. 15625–15636. DOI: `10.1039/C2CP41013C`.

[20] Duyen Thi Nguyen et al. "Super-Resolution Fluorescence Imaging for Semiconductor Nanoscale Metrology and Inspection". In: *Nano Letters* 22.24 (2022), pp. 10080–10087. DOI: `10.1021/acs.nanolett.2c03848`.

[21] S Roy et al. "High speed low power optical detection of sub-wavelength scatterer". In: *Review of Scientific Instruments* 86.12 (2015), p. 123111. DOI: `10.1063/1.4938183`.

[22] Hung-Fei Kuo, Muhamad Faisal, and Shun-Feng Su. "Linewidth Reconstruction Employing a Radial Basis Function Network in Optical Scatterometry". In: *IEEE Access* 4 (2016), pp. 6739–6748. DOI: `10.1109/ACCESS.2016.2616367`.

[23] S Roy et al. "Coherent Fourier scatterometry for detection of nanometer-sized particles on a planar substrate surface". In: *Optics Express* 22.11 (2014), pp. 13250–13262. DOI: `10.1364/OE.22.013250`.

[24] D Kolenov et al. "Direct detection of polystyrene equivalent nanoparticles with a diameter of 21 nm ($\lambda/19$) using coherent Fourier scatterometry". In: *Optics Express* 29.11 (2021), pp. 16487–16505. DOI: `10.1364/OE.421145`.

[25] Jakob J Stamnes. *Waves in focal regions: propagation, diffraction and focusing of light, sound and water waves*. Routledge, 2017.

[26] Nitish Kumar et al. "Reconstruction of sub-wavelength features and nano-positioning of gratings using coherent Fourier scatterometry". In: *Optics Express* 22.20 (2014), pp. 24678–24688. DOI: 10.1364/OE.22.024678.

[27] N Kumar et al. "Phase retrieval between overlapping orders in coherent Fourier scatterometry using scanning". In: *Journal of the European Optical Society-Rapid Publications* 8 (2013), p. 13048. DOI: 10.2971/jeos.2013.13048.

[28] Ansys *Lumerical FDTD solutions*. Available from https://www.lumerical.com/.

[29] Louis Thibon et al. "Resolution enhancement in confocal microscopy using Bessel-Gauss beams". In: *Optics Express* 25.3 (2017), pp. 2162–2177. DOI: 10.1364/OE.25.002162.

[30] İlker R Çapoğlu et al. "The microscope in a computer: Image synthesis from three-dimensional full-vector solutions of Maxwell's equations at the nanometer scale". In: *Progress in Optics* 57 (2012), pp. 1–91. DOI: 10.1016/B978-0-44-459422-8.00001-1.

[31] Bappaditya Dey et al. "Deep learning-based defect classification and detection in SEM images". In: *Metrology, Inspection, and Process Control XXXVI*. SPIE. 2022, PC120530Y. DOI: 10.1117/12.2618178.

3

INSPECTION OF DEFECTS NEAR STRUCTURAL EDGES

This chapter investigates the performance and limitations of coherent Fourier scatterometry (CFS) for defect detection near structural edges. Edge proximity introduces complex scattering backgrounds and reduces sensitivity, posing significant challenges for conventional split-detection CFS. To address these issues, we implement a quad detection scheme that captures scattering asymmetries in multiple directions, thereby improving sensitivity to edge-proximal defects. By combining experiments with three-dimensional electromagnetic simulations, we quantify the influence of edge proximity on detection signals and demonstrate enhanced performance for arbitrarily oriented features in complex device architectures.

Parts of this chapter have been published in Optical Measurement Systems for Industrial Inspection XIV **13567**, 312 (2025) [1], and Optical Measurement Systems for Industrial Inspection XIV **13567**, 550 (2025) [2].

In the previous chapter, we demonstrated that coherent Fourier scatterometry (CFS) enables sensitive, non-destructive detection of nanoscale contaminants and structural defects on periodic surfaces. By combining simulations and experiments, we showed that CFS can detect particles down to 100 nm and classify common defect types such as bridges, breaks, and line collapses. However, many critical defects in real semiconductor devices occur near structural edges, such as line terminations, wafer bevels, or notches, where strong field gradients, material transitions, and background scattering significantly complicate detection.

Edge-proximal inspection poses additional challenges because defect signals often overlap with edge-induced scattering or are masked by geometric asymmetries. Traditional inspection techniques like scanning electron microscopy (SEM) and atomic force microscopy (AFM) offer nanometer-scale resolution but are slow, invasive, and unsuitable for in-line applications [3, 4]. Optical approaches such as bright- and dark-field microscopy provide higher throughput but suffer from diffraction limitations, strong dependence on illumination and defect orientation, and reduced sensitivity near structural edges due to dominant edge-induced scattering [5–8].

CFS offers a promising alternative by analyzing far-field scattering asymmetries with subwavelength sensitivity [9, 10]. Yet, conventional implementations using split detection measure differential signals along a single axis, losing information orthogonal to the scan direction [11]. This directional limitation reduces sensitivity for arbitrarily oriented defects and limits performance near edges, where scattering is inherently multidirectional.

To overcome this, we implement a quad detection scheme that records four independent channels: integrated intensity, left–right and top–bottom differential signals, and a novel quad signal, enabling sensitivity to asymmetries in all directions. Combined with three-dimensional finite-difference time-domain (FDTD) simulations, this approach allows us to quantify how defect–edge proximity influences scattering signals and to define practical detection limits.

3.1. METHODS

3.1.1. IMPLEMENTATION OF QUAD DETECTION SCHEME

In CFS, the far-field scattering pattern carries crucial spatial information about surface morphology and defects. The detection system acts not merely as a passive receiver but as a mathematical operator, transforming this spatial distribution into a measurable signal that emphasizes certain features over others. Traditional implementations of CFS rely on a split detector, which computes the differential signal between opposing halves of the scattered field. Mathematically, this corresponds to applying a first-order directional gradient, analogous to edge detection filters used in image processing, such as the Prewitt operator.

To overcome the directional limitation of split detection, we introduce a quad detector-based scheme. This configuration comprises four independent photodetector elements, denoted A, B, C, and D, arranged in a quadrant geometry (see Fig. 3.1). Each photodetector outputs a current signal, which is converted into a voltage using a dedicated transimpedance amplifier (TIA). The TIA provides high sensitivity and linear conversion, enabling precise capture of optical power fluctuations across the four quadrants.

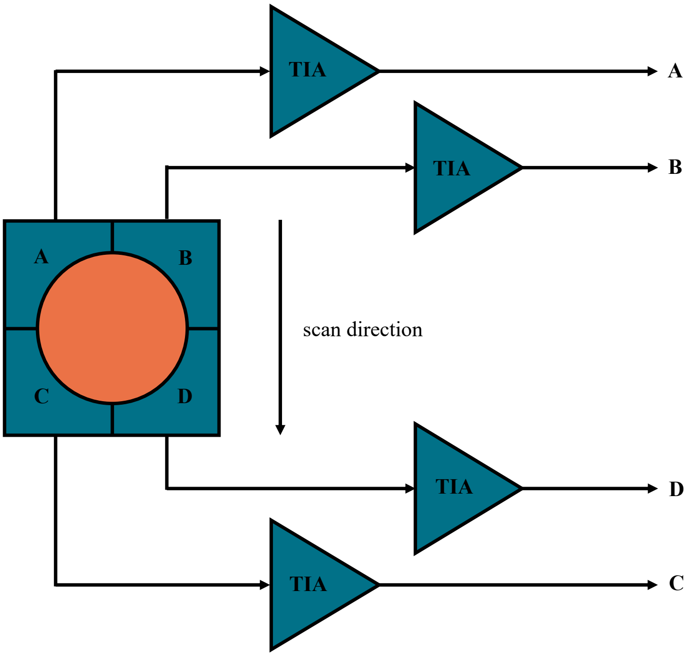

Figure 3.1: Schematic of the quad detector.

The quad detector is carefully aligned such that the incident beam is centered at the intersection of the four pixels, maximizing symmetry and ensuring balanced baseline response.

From these four voltage signals, we compute several derived outputs that encode different spatial characteristics of the scattered field:

$$\text{I signal} = A + B + C + D, \tag{3.1a}$$

$$\text{SD}_{\text{LR}}\ \text{signal} = (A + B) - (C + D), \tag{3.1b}$$

$$\text{SD}_{\text{TB}}\ \text{signal} = (A + C) - (B + D), \tag{3.1c}$$

$$\text{QD signal} = \sqrt{2[(A - D)^2 + (B - C)^2]}. \tag{3.1d}$$

These operators can be interpreted as spatial filters: the SD_{LR} and SD_{TB} correspond to directional derivatives along orthogonal axes (akin to Prewitt masks), while the QD signal approximates the Euclidean norm of the gradient, providing isotropic edge sensitivity.

DATA PROCESSING

Accurate edge detection in CFS requires minimizing detector-specific noise and offset. Due to slight misalignments, the beam may not be centered perfectly on the quad detector, leading to distinct DC offsets in the individual channels. To address this, we employ Fourier filtering to suppress the central DC component of each detector signal prior to calculating the derived outputs. This process ensures uniform baseline correction and enhances signal contrast.

After DC offset removal, the signals are processed pixel-by-pixel using Eqs. 3.1(a)-(d) to generate spatial maps for integrated, split, and quad outputs. These outputs can be interpreted as different modalities of the same optical measurement, each highlighting a distinct feature class: intensity (I), direction-specific asymmetry (SD), and orientation-independent edges (QD).

3.1.2. EXPERIMENTAL SETUP

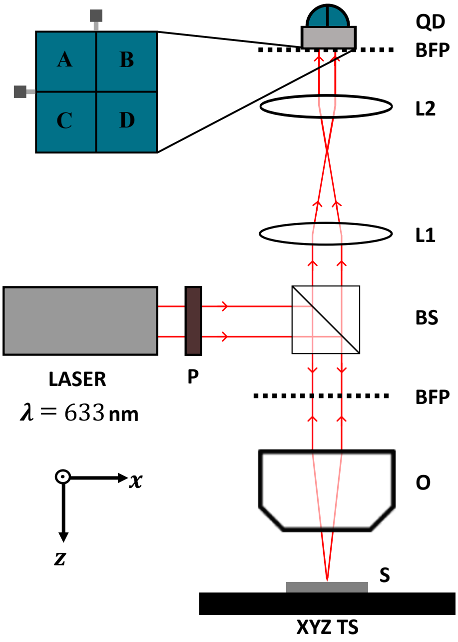

Figure 3.2: Schematic of the experimental setup of coherent Fourier scatterometry (CFS).

The experimental realization of the CFS system with quad detection is shown schematically in Fig. 3.2. A 633 nm He-Ne laser provides a coherent, collimated beam that serves as the illumination source. The beam passes through a rotatable polarizer (P), allowing control over the direction of the incident linear polarization illumination. With this setup, we can select and use any arbitrary linear polarization state for the measurements. The beam is directed onto the sample using a non-polarizing beam splitter (BS) and a high numerical aperture (NA=0.9) objective lens (O), which tightly focuses the beam onto the sample (S). The sample is mounted on a piezo-controlled XYZ translation stage (XYZ TS) and scanned in a serpentine pattern to acquire spatially resolved measurements over the target area. The scattered light from the sample is collected in reflection mode, passing back through the objective and redirected by the BS into the detection path. A 4f (L1 and L2) relay lens system images the back focal plane (BFP) of the objective onto the detection plane, where the quad detector is positioned. The quad detector is mounted on a holder equipped with two orthogonal alignment screws. These allow fine adjustment of the detector position to ensure precise centering of the focused beam on the detector quadrants. Accurate alignment is critical for minimizing signal imbalance and ensuring the correct computation of integrated, split, and quad signals as described in Section 3.1.1.

3.1.3. NUMERICAL MODEL

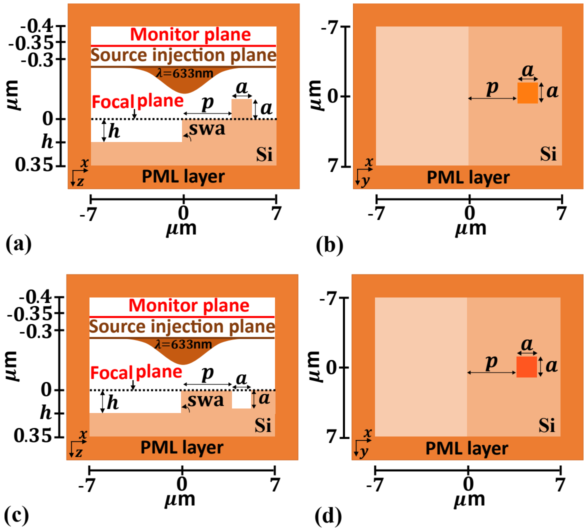

Figure 3.3: The 3D-FDTD simulation scheme of a defect near the edge. The edge is characterized by geometrical parameters: swa and h, being illuminated by a TM polarized focused spot of wavelength 633 nm and NA=0.9. The particle and the burrow are characterized by the parameters: a and p. The corresponding y = 0 plane in (a) and (c). The corresponding z = 0 plane in (b) and (d).

To model defect interactions near edges, we performed 3D FDTD simulations using Lumerical software. In Fig. 3.3(a) and (c), the y = 0 plane, and in Fig. 3.3(b) and (d), the z = 0 plane of the complete 3D-FDTD model is depicted. The simulation domain consisted of a silicon substrate with a well-defined edge, and a cubical particle or burrow (dimension, a = 100 nm) placed at varying distances (p = 0 nm to 1000 nm) from the edge. The edge is defined by the geometrical parameters, sidewall angle, $swa = 90°$, and height, h = 100 nm. The domain was illuminated with a TM-polarized beam (i.e., the polarization direction at the pupil is parallel to the x-axis, λ =633 nm) focused through a 0.9 NA objective, resulting in a ~858 nm spot size. Perfectly matched layer (PML) boundaries were used to absorb outgoing waves. Field monitors were positioned to capture near-field data, which was transformed into far-field signals. The differential signal was calculated by analyzing asymmetries across the detection plane. To simulate scanning effects, we shift the simulation object along the x-axis, keeping the position of the source injection plane, monitor plane, and computational domain constant. Simulation geometry and materials were defined in alignment with the previous explanation in Section 2.1.3, ensuring consistency with experimental conditions.

3.2. RESULTS

3.2.1. PARTICLES NEAR THE EDGE: NUMERICAL STUDY

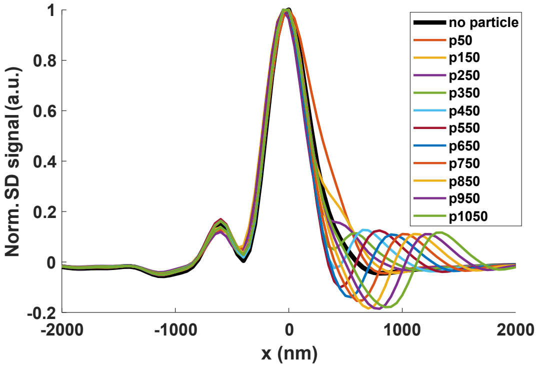

Figure 3.4: Simulated CFS scan profiles for 100 nm particles at varying distances from the edge ($p = 50$ nm to 1050 nm). As the particle distance increases, a distinct particle signal with a central zero-crossing emerges. For distances below 350 nm (≈ diffraction limit of the system), the particle signal blends with the edge response, defining the system's resolution limit for particle detection.

To systematically assess the limits of particle detection near edges, we simulated a 100 nm particle in the shape of a cube placed at varying distances ($p = 50$ nm to 1050 nm) from a sharp edge on a planar Si substrate. Using the 3D FDTD model described earlier, we computed the split detector signals corresponding to each particle-edge configuration. The illumination conditions replicated the experimental setup: a TM-polarized (perpendicular to the edge) 633 nm beam focused by a 0.9 NA objective lens. The focused spot size was approximately 858 nm, setting a theoretical resolution limit of ~351 nm ($\lambda/2\text{NA}$). The far-field profiles were analyzed to extract the normalized differential signal. Figure 3.4 shows the resulting normalized scan profiles for each particle distance to the edge p. As the particle is moved farther from the edge, its signature in the CFS signal becomes increasingly distinguishable. For $p > 858$ nm (the spot diameter), the particle and edge produce independent scattering features, confirming the spatial resolution of CFS in this regime. As the particle moves closer to the edge, the individual particle signal begins to merge with the edge response, leading to reduced contrast and signal ambiguity.

Nevertheless, a discernible deviation from the baseline edge signal is still observable down to $p = 350$ nm; this distance is close to the diffraction limit in this configuration. It is worth noting that for particles localized at a distance $p < 350$ nm, the CFS signal is still different from the non-particle case (black line in Fig. 3.4). Additional signal processing or multi-line scanning with a quad detection scheme could further enhance defect detectability within this subspot size regime.

3.2.2. BURROWS NEAR THE EDGE: NUMERICAL STUDY

To extend the defect detection analysis, we examined the detectability of subsurface burrows (voids or pits) near edges using the same 3D FDTD framework. The modeled burrows were cubical indentations with a dimension of 100 nm, placed at various lateral

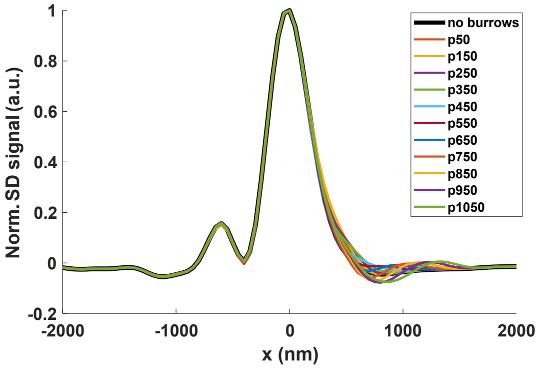

Figure 3.5: Simulated CFS scan profiles for burrows at varying distances from the edge ($p = 50$ nm and 1050 nm). Burrow signals are weaker than those of the above surface particles and exhibit a larger distance $p = 650$ nm, beyond which the burrow can be distinctly resolved from the edge.

distances ($p = 50$ nm to 1050 nm) from the edge. Simulations were performed using the same TM-polarized 633 nm illumination and a 0.9 NA objective, maintaining consistency with particle simulation conditions. The far-field response was extracted from the near-field monitors and analyzed via the split detector signal. Figure 3.5 shows the normalized differential signal profiles for the burrow simulations. Similar to the particle case, as the burrow is placed farther from the edge, a distinct signal emerges. However, the amplitude of the signal associated with burrows is significantly lower than that for surface particles, owing to the reduced scattering efficiency of sub-surface features. In particular, distinct burrow signals are observed until $p \geq 650$ nm, beyond which the edge and burrow signatures can be resolved separately. For $p < 650$ nm, the edge signal dominates, and the burrow's presence results only as subtle distortions in the overall profile. This suggests a larger resolution threshold for burrows compared to particles, consistent with their lower scattering cross-section.

These results highlight that while subsurface burrow detection near edges is feasible with CFS, differences in the scattered signal are smaller than for surface particles. Nonetheless, as with particle detection, multi-line scanning strategies and profile shape analysis with a quad detection scheme could help infer the presence of such defects even below the conventional resolution limit.

3.2.3. INSPECTION OF NANOPARTICLES: EXPERIMENTAL STUDY

To evaluate the performance of the quad detection scheme, we first scanned a 25 × 25 µm area of a sample containing 150 nm polystyrene latex (PSL) nanoparticles on a Si wafer. Figure 3.6 shows the raw voltage signals obtained from the four photodetector channels (A, B, C, and D), after removal of the DC background using Fourier filtering. These signals form the basis for all subsequent outputs. Here, the individual channel signals show weak signals arising from the scattering of the PSL nanoparticles.

In Fig. 3.7 we show the 25 × 25 µm CFS scanned maps of I, SD_{LR}, SD_{LR}, and QD signal of 150 nm PSL nanoparticles. These signals were computed using Eq. 3.2 on the individual photodetector channel signals A, B, C, and D. The I signal shows the total intensity of

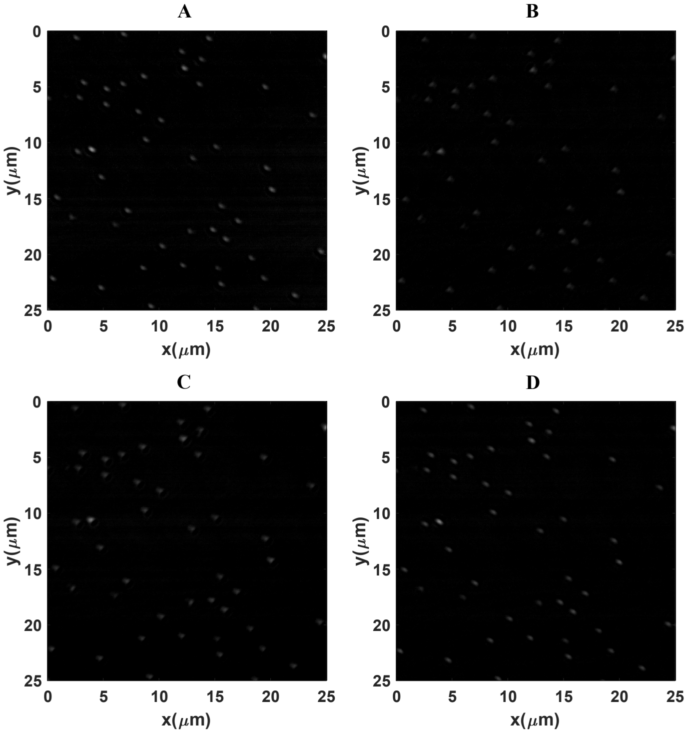

Figure 3.6: 25 × 25 µm CFS scanned map showing signals from each individual photodetector (A, B, C, and D) of 150 nm PSL nanosparticles on Si wafer.

the scattered field. While this mode captures the presence of particles through intensity variation, it lacks directional sensitivity and edge specificity. The SD signals (SD_{LR} and SD_{TB}) highlight asymmetries in the far-field scattering pattern, producing characteristic dipole-like lobes aligned with the scan direction. This result mirrors previous implementations of CFS using single-axis split detectors and is effective for detecting directional features or off-center scattering profiles. However, as shown in Fig. 3.7, the QD signal provides a fundamentally different representation. It reveals ring-like patterns corresponding to the edges of the particles, with much clearer definition and isotropic contrast. This demonstrates that the QD signal is sensitive to gradients and edges irrespective of their orientation relative to the scan axis.

Interestingly, as shown in Fig. 3.8, the rings observed around the particles are not perfectly circular, but rather elliptical. This shape distortion is linked to the ellipticity of the point spread function (PSF) of the system, caused by the high numerical aperture (NA) of the illumination beam. To verify this, we performed measurements with different polarization orientations of the incident beam. Figure 3.8 shows the QD signal for two different arbitrary incident illumination polarization directions defined by angle $\theta \sim 20^\circ$ (left) and $\theta \sim 90^\circ$ (right). Notably, the orientation of the elliptical edge response rotates with the polarization, confirming that the observed ellipticity is not intrinsic to the parti-

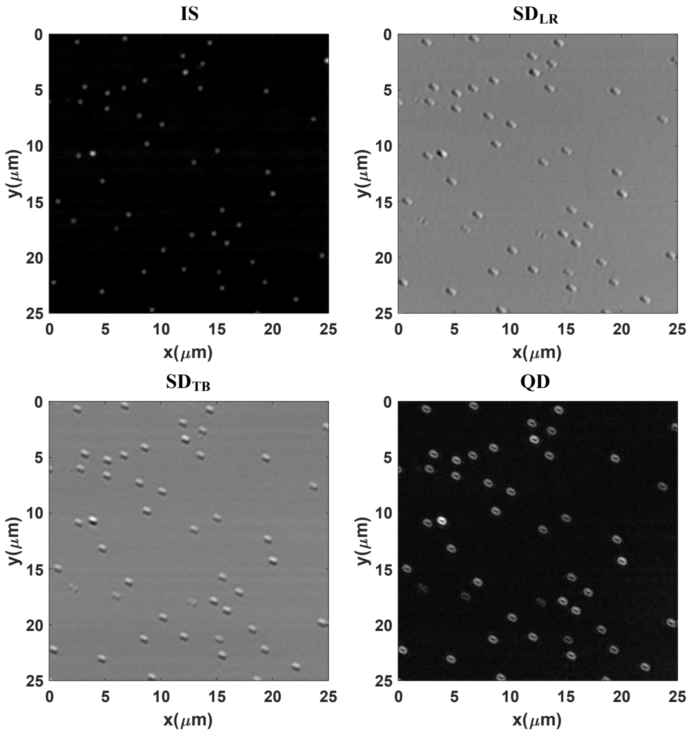

Figure 3.7: 25 × 25 μm CFS scanned map showing I, SD_{LR}, SD_{LR}, and QD signal of 150 nm PSL nanosparticles on Si wafer (obtained using Eq. 3.1).

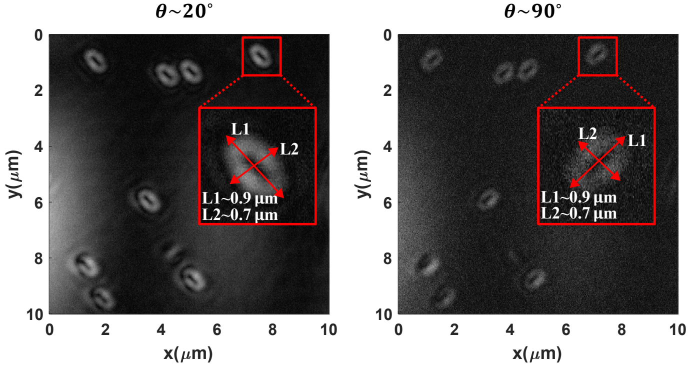

Figure 3.8: 10 × 10 μm CFS scanned map showing QD signal of 150 nm PSL nanosparticles for two different illumination polarization directions defined by angle $\theta \sim 20^{\circ}$ (left) and $\theta \sim 90^{\circ}$ (right).

cles but originates from the illumination PSF. Insets in Fig. 3.8 show a zoom into a single particle and measure the edge dimensions of the PSF (L1∼ 0.9 μm, L2∼ 0.7 μm), clearly illustrating that the quad signal is tracking the PSF footprint rather than the physical size of the particle. This highlights that for subspot-size particles, the edge detection reflects the intensity gradient of the beam rather than the actual object boundary. As the particle size approaches the illumination spot size, the quad signal is expected to more accurately trace the physical edges.

SNR

The signal-to-noise ratio (SNR) for the different outputs can be compared by computing the power ratio between signal and background regions. For the quad signal, we define it as:

$$\mathrm{SNR}_{\mathrm{dB}}^{\mathrm{QD}} = 10\log_{10}\frac{P_{sig}^{\mathrm{QD}}}{P_{noise}^{\mathrm{QD}}} = 10\log_{10}\frac{P_{sig}^{\mathrm{SD_{LR}}}+P_{sig}^{\mathrm{SD_{TB}}}}{P_{noise}^{\mathrm{SD_{LR}}}+P_{noise}^{\mathrm{SD_{TB}}}}, \tag{3.2}$$

where, P_{sig}^{QD}, $P_{sig}^{\mathrm{SD_{LR}}}$, and $P_{sig}^{\mathrm{SD_{TB}}}$ is the power of the signal (contained at the edges of the nanostructure) for QD, $\mathrm{SD_{LR}}$, and $\mathrm{SD_{TB}}$ signals, respectively, and P_{noise}^{QD}, $P_{noise}^{\mathrm{SD_{LR}}}$, and $P_{noise}^{\mathrm{SD_{TB}}}$ is the background noise of the QD, $\mathrm{SD_{LR}}$, and $\mathrm{SD_{TB}}$ signals, respectively. According to Eq. 3.2, the $\mathrm{SNR}_{\mathrm{dB}}^{\mathrm{QD}} = 10.76$ for the 150 nm PSL nanoparticles. We similarly calculate, $\mathrm{SNR}_{\mathrm{dB}}^{\mathrm{SD_{LR}}} = 9.93$ and $\mathrm{SNR}_{\mathrm{dB}}^{\mathrm{SD_{TB}}} = 11.26$. The QD signal does not necessarily yield the highest SNR. In practice, one of the individual split signals may achieve better contrast or exhibit lower background noise, resulting in superior SNR compared to the combined QD output. This indicates that the QD signal offers a balance between noise suppression and feature completeness, rather than maximizing SNR alone. However, the key advantage of the QD signal lies in its orientation-invariant edge detection, which makes it particularly effective for irregularly oriented nanostructure patterns or situations where split detection may fail to provide consistent output.

3.2.4. INSPECTION OF PATTERNED NANOSTRUCTURES: EXPERIMENTAL STUDY

Having validated the scheme on symmetric particles, we turn to its primary application: inspecting patterned nanostructures with arbitrary feature orientation. Figure 3.9 presents the $\mathrm{SD_{LR}}$ (left column), $\mathrm{SD_{TB}}$ (middle column), and QD (right column) obtained from various marker patterns, such as crossed lines (two patterns), and saw tooth patterns (two patterns), fabricated on a wafer. These features span a range of orientations and edge profiles. The split signals in this case exhibit strong directional bias; edges aligned with the gradient axis are highlighted, while orthogonal features are suppressed or distorted. As a result, fine details, such as corner shapes, edge defects, or small indentations, are either missed or partially resolved in the SD maps. Further, $\mathrm{SD_{LR}}$ and $\mathrm{SD_{TB}}$ are not mutually transferable by a 90° rotation. This asymmetry arises from the polarization-dependent scattering response, which couples differently to edges of different orientations. In contrast, the quad signal in Fig. 3.9 provides a uniform edge representation, capturing all edge orientations simultaneously. This confirms the central premise of the quad detection scheme, which enables orientation-independent edge detection, crucial for inspecting nanostructures, which may not be aligned with the scan direction.

These results demonstrate that the quad detector scheme significantly expands the applicability of CFS. It enhances edge contrast, maintains rotational invariance, and enables more robust defect detection for complex surface features.

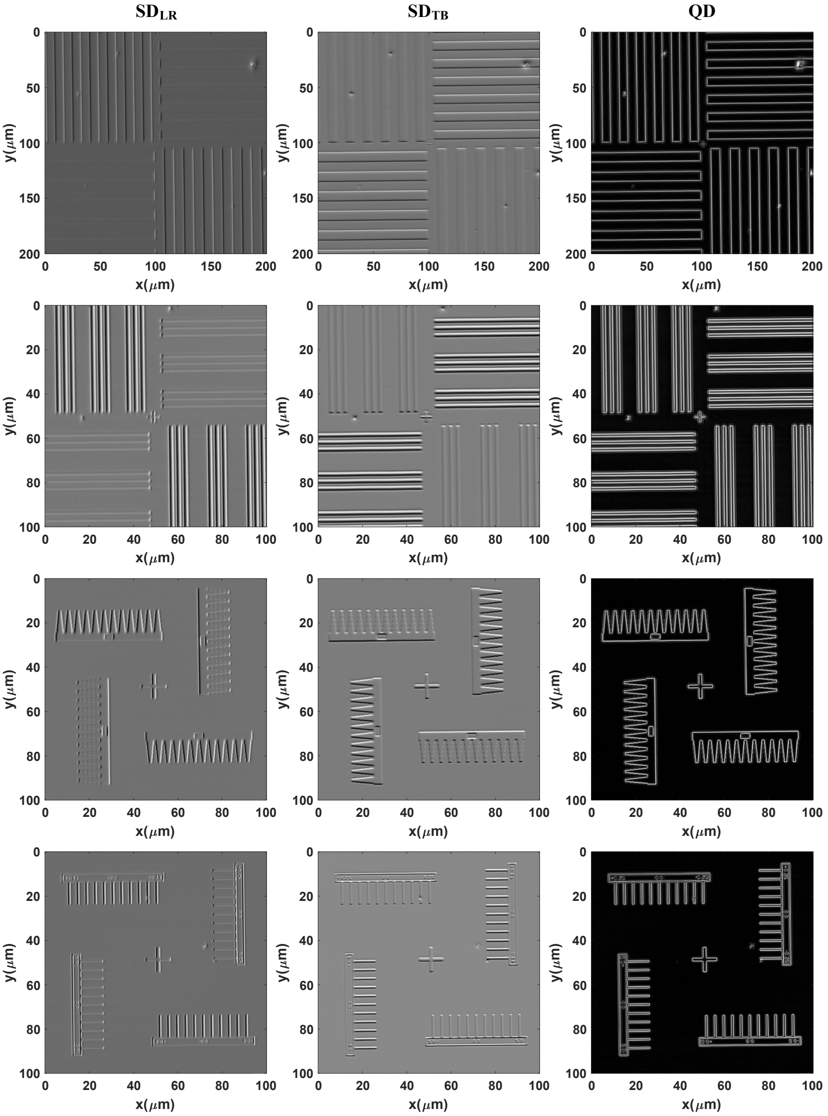

Figure 3.9: CFS scans of four different types of markers fabricated on Si wafer. (left column) showing SD_{LR} signal; (middle column) showing SD_{TB} signal; (right column) showing QD signal. Here we can also detect the defects on top of the nanostructures.

3.3. SUMMARY

In this chapter, we extended coherent Fourier scatterometry (CFS) beyond periodic structures to investigate its capabilities and limitations for defect detection near structural edges. We showed that edge proximity introduces strong field perturbations and complex scattering backgrounds that obscure conventional defect signatures, significantly reducing detection sensitivity. To overcome the directional limitations of traditional split detection, we implemented a quad detection scheme capable of capturing scattering asymmetries in all directions. By combining this approach with three-dimensional FDTD simulations and experimental measurements, we quantified how defect–edge distance and orientation influence the CFS response and demonstrated improved detection of nanoparticles and structural defects in edge-rich environments. These results highlight both the current constraints and future potential of CFS for edge-critical inspection, laying the groundwork for advanced metrology strategies in complex device architectures where conventional techniques often fail.

BIBLIOGRAPHY

[1] Anubhav Paul and Silvania F Pereira. “Implementation of quad detection scheme in coherent Fourier scatterometry for inspection of patterned structures”. In: *Optical Measurement Systems for Industrial Inspection XIV*. Vol. 13567. SPIE. 2025, pp. 312–320. DOI: 10.1117/12.3062040.

[2] Anubhav Paul and Silvania F Pereira. “Limits of detection of defects near edges of nanostructures for coherent Fourier scatterometry”. In: *Optical Measurement Systems for Industrial Inspection XIV*. Vol. 13567. SPIE. 2025, pp. 550–556. DOI: 10.1117/12.3062549.

[3] Carl Georg Frase, Egbert Buhr, and Kai Dirscherl. “CD characterization of nanostructures in SEM metrology”. In: *Measurement Science and Technology* 18.2 (2007), p. 510. DOI: 10.1088/0957-0233/18/2/S26.

[4] Danish Hussain et al. “Advances in the atomic force microscopy for critical dimension metrology”. In: *Measurement Science and Technology* 28.1 (2016), p. 012001. DOI: 10.1088/0957-0233/28/1/012001.

[5] Richard M Silver et al. “The limits and extensibility of optical patterned defect inspection”. In: *Metrology, Inspection, and Process Control for Microlithography XXIV*. Vol. 7638. SPIE. 2010, pp. 182–194. DOI: 10.1117/12.850935.

[6] Toshie Yoshioka, Takashi Miyoshi, and Yasuhiro Takaya. “Particle detection for patterned wafers of 100nm design rule by evanescent light illumination: analysis of evanescent light scattering using finite-difference time-domain (FDTD) method”. In: *Optomechatronic Sensors and Instrumentation*. Vol. 6049. SPIE. 2005, pp. 73–81. DOI: 10.1117/12.647933.

[7] Laura Peters. *Defect Challenges Grow At The Wafer Edge*. Available at https://semiengineering.com/defect-challenges-grow-at-the-wafer-edge/. 2024.

[8] Burhan Ali. *A Bare Wafer Mystery: Inspecting For Back, Edge, And Notch Defects In Advanced Nodes*. Available at https://semiengineering.com/a-bare-wafer-mystery-inspecting-for-back-edge-and-notch-defects-in-advanced-nodes/. 2023.

[9] D Kolenov et al. “Direct detection of polystyrene equivalent nanoparticles with a diameter of 21 nm ($\lambda/19$) using coherent Fourier scatterometry”. In: *Optics Express* 29.11 (2021), pp. 16487–16505. DOI: 10.1364/OE.421145.

[10] S Roy et al. “Coherent Fourier scatterometry for detection of nanometer-sized particles on a planar substrate surface”. In: *Optics Express* 22.11 (2014), pp. 13250–13262. DOI: 10.1364/OE.22.013250.

[11] Anubhav Paul et al. “Coherent Fourier scatterometry: a holistic tool for inspection of isolated particles or defects on gratings”. In: *Applied Optics* 62.29 (2023), pp. 7589–7595. DOI: `10.1364/AO.503350`.

4

DEEP SUBSURFACE NANOSTRUCTURE METROLOGY IN SILICON

This chapter presents a near-infrared coherent Fourier scatterometry (CFS) approach for non-destructive inspection of deeply buried nanostructures in silicon. By exploiting silicon's transparency in the near-IR and optimizing source coherence and spatial filtering, unwanted interface reflections are suppressed and weak subsurface scattering signals are enhanced. The technique enables detection of subwavelength features such as nanoparticles, nanopillars, nanopits, and buried gratings under silicon layers up to 500 µm *thick, providing a high-throughput metrology solution for 3D integration, bonded overlay, and multilayer device inspection.*

Parts of this chapter have been published in Optics and Lasers in Engineering **195**, 109354 (2025) [1].

In the previous chapters, we demonstrated the capability of coherent Fourier scatterometry (CFS) for surface inspection of nanoscale defects on periodic and edge-proximal structures. Building on this foundation, this chapter extends CFS to one of the most challenging areas in semiconductor metrology: non-destructive detection of deeply buried nanostructures.

As device architectures evolve toward complex 2.5D and 3D integration with stacked dies, micro-bumps, and through-silicon vias (TSVs), detecting buried defects such as voids, cracks, and incomplete interconnects has become increasingly critical for yield and reliability [2–6]. Existing techniques including X-ray microscopy [7, 8], scanning acoustic microscopy (SAM) [9], photoluminescence [10], and atomic force microscopy (AFM) [11, 12] face trade-offs in resolution, depth penetration, throughput, or invasiveness. Infrared (IR) microscopy leverages Si transparency [13, 14] but is diffraction-limited and suffers from strong Fresnel reflections [15].

CFS offers a promising alternative by analyzing far-field scattering to retrieve subdiffraction information [16, 17]. Operating in the near-IR, where Si is transparent, and controlling the source coherence length suppresses unwanted reflections, while spatial filtering isolates weak scattering from buried structures. This enables the non-destructive detection of subwavelength features, including nanoparticles, nanopillars, nanopits, and buried gratings, even under 500 µm of Si.

4.1. METHODS

4.1.1. EXPERIMENTAL SETUP

Here, the experimental configuration of the CFS setup, schematically illustrated in Fig. 4.1, is employed to perform the measurements in this chapter. A laser diode controller (LDC) drives a near-infrared diode laser (λ = 1055 nm). The emitted light is coupled into a single-mode fiber (SMF) using a lens (L1), and an off-axis parabolic mirror (OAP M1) collimates the emerging beam. The collimated beam passes through a polarizer (P1), which is used to set the polarization direction of the illumination beam. In the experiments, we use the TE polarization configuration, where the polarization direction of P1 at the pupil is parallel to the y-axis (see Fig. 4.1). The linearly polarized beam is directed through a nonpolarizing beam splitter (BS1) and then focused onto the sample using a microscope objective (MO) having a numerical aperture (NA) of 0.55, resulting in a focused spot having Airy diameter of $1.22\lambda/\mathrm{NA} = 2.34$ µm. The sample is mounted on a piezocontrolled translation stage (XYZ TS) to scan the sample in the (x, y) plane. The translation stage can be laterally scanned in a serpentine pattern. The scattered light is collected by the same MO and transmitted back through the nonpolarizing beam splitters (BS1 and BS2). A telescopic system composed of two lenses (L2 and L3) relays the light to the back focal plane (BFP) of the MO. A complementary metal-oxide-semiconductor (CMOS) camera positioned at this plane captures the so-called far-field signatures, which is the angular spectrum of the scattered waves from all incident plane waves within the focused spot. A pinhole (F1) is placed between L2 and L3, as a spatial filter to selectively remove unwanted scattering from the defocused planes. A split detector (SD) is placed in the BFP of the MO with the help of a mirror (M2) and another telescopic system composed of two lenses (L4 and L5). The split detector consists of two pixels aligned perpendicular

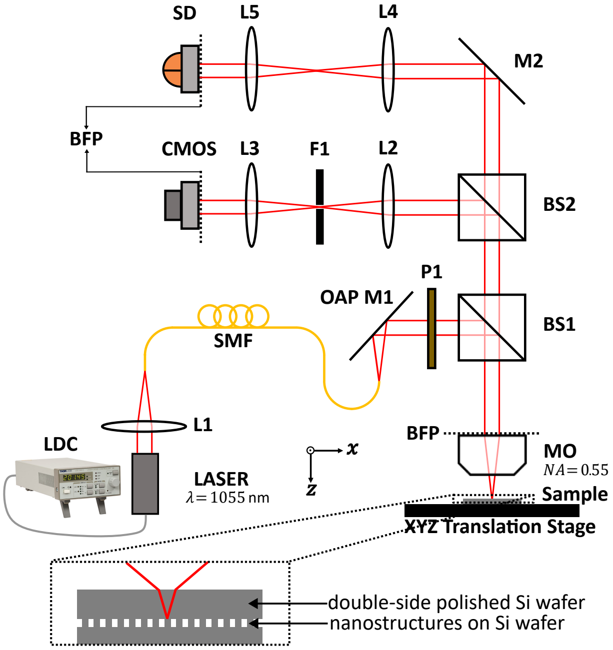

Figure 4.1: Schematic of the experimental setup of coherent Fourier scatterometry (CFS).

to the scan direction, and the intensity from one pixel is subtracted from the other. In defect-free regions of the sample, the scattered far-field pattern (specular reflection) remains reflection symmetric with respect to the illumination polarization direction. This results in nearly equal intensities on both detector halves and a differential signal close to zero. Additionally, the specular reflections from the polished air–Si interface, are also effectively suppressed. As a result, both background specular reflections and system noise are suppressed, and we observe a clean, near-zero baseline. Due to this unique feature we do not need to use a spatial filter in this beam arm. Now, as the focused beam is scanned through a nanostructure placed on the sample, the far field signature becomes asymmetric, and we observe a position-dependent differential signal.

In the experiments, we investigate samples consisting of nanostructures such as gratings and various types of defects buried within Si. However, fabricating such buried structures with precise control is highly complex [18]. To overcome this challenge, we first measure the nanostructures that are fabricated on the Si wafer without any overlying Si layer (sample in its exposed state). Then, to simulate different degrees of buriedness, we place double-side polished Si wafers of varying thicknesses on top of the structures. This approach allows us to systematically study how the overlying Si influences the scattering and far-field signatures, providing insights into the detectability of buried features.

4.1.2. REFOCUSING ADJUSTMENT FOR SI LAYER COMPENSATION

Accurate focusing of the illumination beam onto the nanostructures under investigation is crucial for obtaining reliable experimental results. However, when a Si wafer is placed on

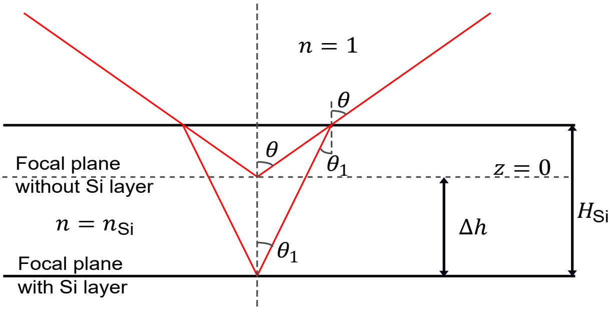

Figure 4.2: Schematic illustration of the focal shift when a Si layer of thickness H_{Si} is placed on top of the sample. The red lines represent the maximum cone of light forming the focused spot before (angle θ) and after (angle θ_1) entering the Si layer.

top of the sample, the focal plane shifts [19]. As the beam now travels through a medium with a different refractive index, the original focus moves away from the nanostructures, requiring an adjustment in the z-axis to bring the focus back onto the buried nanostructures. To quantify this focal shift, we consider the schematic as illustrated in Fig. 4.2, which depicts the displacement Δh needed to refocus the beam onto the nanostructures when a Si layer of thickness H_{Si} is introduced. The red lines in the diagram represent the maximum cone of light forming the focused spot. Initially, outside the Si layer, this cone is defined by the angle θ, where, $\sin(\theta) = \text{NA}$. Upon entering the Si layer, the light undergoes refraction due to the difference in refractive indices. The new propagation angle inside the Si is denoted as θ_1, given by, $\theta_1 = \sin^{-1}\left(\frac{\text{NA}}{n_{\text{Si}}}\right)$, where n_{Si} is the refractive index of Si. Since the focal plane inside the Si is determined by the altered beam convergence, the required displacement in the $z-$axis to refocus the beam onto the buried nanostructures is derived as:

$$\Delta h = H_{\text{Si}}\left(1 - \frac{\tan(\theta_1)}{\tan(\theta)}\right). \tag{4.1}$$

The Eq. 4.1 provides a straightforward method to calculate the necessary focal adjustment based on the Si layer thickness and the numerical aperture (NA) of the objective. By precisely shifting the focus by Δh, we ensure that the beam remains optimally focused on the nanostructures despite the presence of the Si layer, thereby maintaining measurement accuracy and consistency across different sample configurations. For instance, Si wafers of thickness H_{Si} 300 µm and 500 µm, require shifts of Δh approximately 229 µm and 381 µm, respectively.

4.1.3. ABERRATIONS ANALYSIS

In this section, we present a detailed analysis of the wavefront aberrations induced when a focused laser beam passes through a Si wafer using Zemax optical design software [20]. To mimic the experimental conditions, we model a linearly polarized plane wave of wavelength 1055 nm, illuminating the objective lens having NA of 0.55. The objective focuses the light on the focal plane, where we add a Si wafer having thickness H_{Si}. We move the Si such that the beam focuses on the back surface of the wafer. We then evaluated

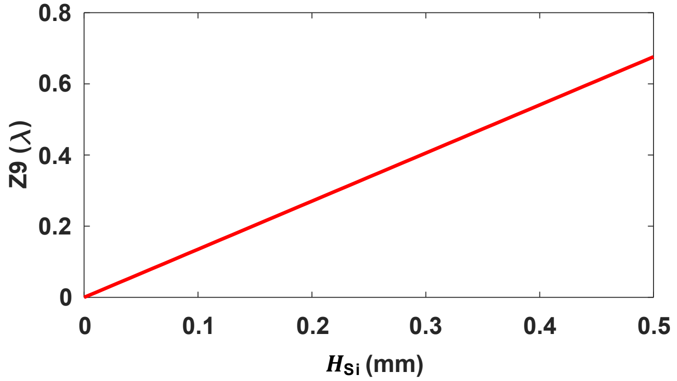

Figure 4.3: Variation in spherical aberration (Z9) as a function of the Si wafer thickness H_{Si} based on Zemax simulations.

the wavefront aberrations in this focal plane for varying thicknesses of the Si wafer. More details about the design parameters have been provided in Appendix A. We observe that only spherical aberration (Zernike term Z9) is introduced in the wavefront because of the wafer [21]. Figure 4.3 shows the relative variation in Z9 as we increase the thickness H_{Si} of the wafer, where we see that Z9 increases linearly with thickness. This trend indicates that in inspecting nanostructures through even thicker Si layers, compensating for the resulting spherical aberrations will be crucial for achieving a high quality of the focused spot, which can be sufficiently addressed by either using adaptive optics or aspherical lens designs.

4.1.4. COHERENCE TUNING FOR INTERFERENCE SUPPRESSION

When investigating nanostructures such as gratings, where we retrieve structural parameters using far-field signatures, it is crucial to minimize unwanted interference from reflections at the air-Si interface. Although Si is highly transparent in the near-IR range due to its extremely low absorption coefficient ($\Im(n_{\mathrm{Si}}) = 0.0001114$) at 1055 nm, its high refractive index ($\Re(n_{\mathrm{Si}}) = 3.5575$) causes significant Fresnel reflections at the air-Si boundary. These reflections interfere with the light scattered from the nanostructures, producing interference fringes in the far-field that complicate the data interpretation.

For applications such as grating inspection, where structural parameters are retrieved solving inverse problems from scattering responses, this interference is undesirable. The presence of strong reflections from the air-Si interface introduces additional complexity to the inverse problem, making an already ill-posed problem even harder to solve. To suppress this interference, we tune the coherence length of the laser so that it is shorter than the thickness of the Si layer, ensuring that the reflection from the air-Si interface and the scattering from the nanostructure become mutually incoherent while maintaining sufficient coherence for the coherent scattering of the nanostructures. The coherence length (L_c) is approximated by $L_c = \lambda^2/\Delta\lambda$, where λ is the central wavelength, and $\Delta\lambda$ is the spectral linewidth. We adjust L_c by controlling the driving current of the laser diode controller. Above the lasing threshold (e.g., 30 mA), the laser operates in a narrow spectral

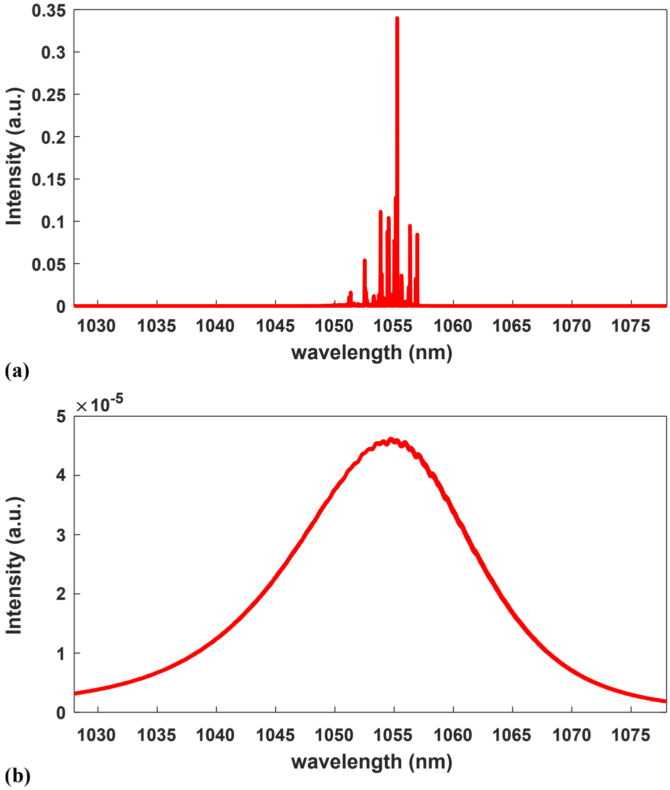

Figure 4.4: Laser spectra at two operating conditions. (a) Above the lasing threshold (30 mA), the narrow linewidth results in high coherence length. (b) Below the lasing threshold (17 mA), the broadened spectrum reduces coherence length.

mode with a long coherence length ($L_c^{\text{lasing}} = 48392$ µm), maintaining coherence and leading to strong interference. Below the lasing threshold (e.g., 17 mA), the laser spectrum broadens significantly, reducing the coherence length to ($L_c^{\text{non-lasing}} = 61.83$ µm), which is much smaller than the Si layer thickness we use in this study. This effectively removes interference between the reflection and scattered components, ensuring that the far-field signature primarily originates from the nanostructure. This state of the laser, combined with a spatial filter (pinhole), ensures that reflections from the air-Si interface do not distort the far-field signature.

However, for the application of inspection of defects, we operate the laser above the lasing threshold, as the split detector eliminates the specular reflections from the air-Si interface. In Fig. 4.4, we show the measured laser spectra for both cases: (a) above the lasing threshold (30 mA), showing a narrow linewidth and long coherence length, and (b) below the lasing threshold (17 mA), exhibiting a broadened spectrum and reduced coherence length. These spectra were recorded using an optical spectrum analyzer, Yokogawa AQ6374.

4.1.5. SAMPLE DETAILS

The samples investigated in this work include various nanostructures and defects fabricated on Si substrates. For defect inspection, we use three different samples: (1) a sample with 400 nm polystyrene (PSL) nanospheres deposited on a Si wafer, (2) a sample with 10 × 2 Si nanopillars, consisting of two rows of cube- and cylinder-shaped nanopillars with lateral nominal dimensions ranging from 100 nm to 1000 nm in 100 nm steps and a nominal height of 250 nm, and (3) a sample with 4 × 5 etched nanopits on a Si wafer, where the pits have a cubic shape with lateral sizes from 125 nm to 425 nm in 100 nm steps and a nominal height of 160 nm, organized into five rows of identical structures. Further details on the fabrication of these nanostructures can be found in Ref. [22]. For grating inspections, we use a Si grating with a pitch of 1430 nm, with rectangular profile, 50% duty cycle, and height of 160 nm. Additional fabrication details can be found in Ref. [23]. To simulate the buriedness of these nanostructures, we place double-sided polished Si wafers of 300 µm and 500 µm thickness on top of the samples.

4.2. RESULTS

4.2.1. INSPECTION OF DEFECTS

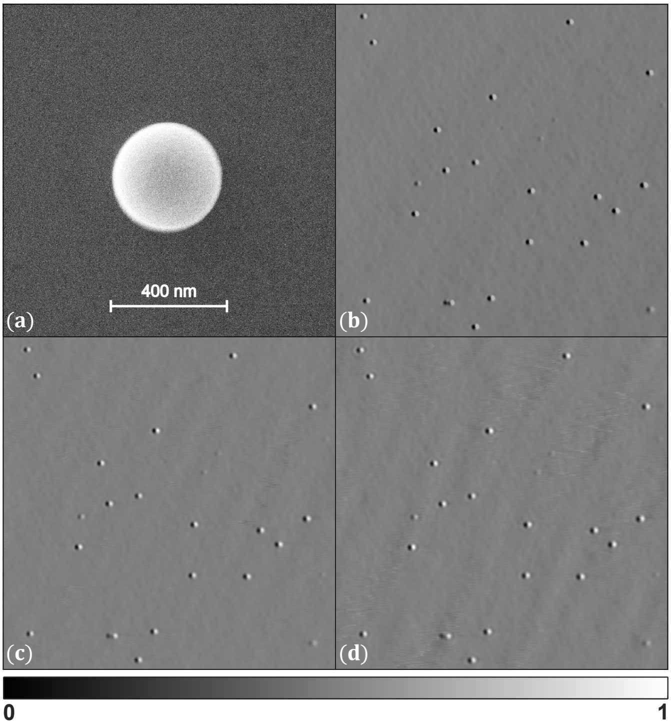

Figure 4.5: (a) SEM image of a 400 nm PSL nanosphere on Si with no overlying wafer. (b) CFS scan of a 100 × 100 µm region showing 400 nm PSL nanospheres on Si with no overlying wafer. (c) CFS scan of the same region with a 300 µm thick Si wafer on top. (d) CFS scan of the same region with a 500 µm thick Si wafer on top.

In this section, we demonstrate the capabilities of CFS for inspecting isolated defects buried within a Si wafer. Here, we detect 400 nm polystyrene (PSL) nanospheres (smaller than the diffraction limit, $\lambda/2\mathrm{NA}$) deposited on a Si wafer. To perform defect inspection, we operate the laser above its lasing threshold ($L_c^{\text{lasing}} = 48392\ \mu\text{m}$) with a lasing power of 0.5 mW. Our goal is to systematically examine how overlying Si layers affect the scattering signals. We first measure each sample in its exposed state (with no Si wafer on top). To simulate different degrees of buriedness, Si wafers with thicknesses 300 μm and 500 μm are then placed over the sample. After each wafer is added, the focal plane is readjusted by moving the translation stage along the $z-$axis, as described in Section 4.1.2. Figure 4.5(a) shows an SEM image of a 400 nm PSL nanosphere on Si without any Si wafer on top (SEM imaging cannot be performed through the Si wafer due to limited electron penetration depth). Figures 4.5(b)–(d) shows the CFS scans of a 100 × 100 μm region of 400 nm PSL nanospheres on Si: (b) without Si wafer on top; (c) with 300 μm Si wafer on top; and (d) with 500 μm Si wafer on top. The PSL nanospheres are clearly detected in all cases, illustrating that CFS can effectively inspect defects even under 500 μm of Si. To quantify performance, we calculate the signal-to-noise ratio (SNR) according to

$$\mathrm{SNR_{dB}} = 10\log_{10}\left(\frac{P_{\text{signal}}}{P_{\text{noise}}}\right), \tag{4.2}$$

where P_{signal} is the power of the signal (contained in the defects) and P_{noise} is the background noise. Table 4.1 lists the calculated SNR values. Although the SNR is high for all the cases, it decreases slightly as the wafer thickness increases. This is primarily due to aberrations introduced by the additional Si layers, which degrade the focal spot and reduce the Strehl ratio. Further, in the context of our CFS based detection scheme, the detection capability is not governed by the conventional diffraction limit ($\lambda/2\mathrm{NA} \approx 959$ nm) of the system, but rather by the SNR of the scattered signal associated with the defect. That is, defect detection is feasible as long as the defect-induced signal exceeds the system noise floor, even if the defect is subwavelength in size. A comprehensive analysis of CFS regarding minimum detectable signal, noise tolerance, and dynamic range has already been demonstrated by Kolenov *et al.* [24].

Table 4.1: Measured SNR of 400 nm PSL sample.

Case	**SNR**$_{\text{dB}}$
Without Si wafer on top	26.09
With 300 μm Si wafer on top	25.28
With 500 μm Si wafer on top	23.04

Now, to investigate the limitation of the technique in determining how small the defects can be and still be detected, we consider two types of defects: nanopillars and nanopits. Our samples consist of these nanostructures with varying lateral dimensions, with the smallest defects of dimension ~ $\lambda/10$, as already discussed in Section 4.1.5. The experimental approach is the same as that used for the 400 nm PSL nanospheres, detailed earlier. Figure 4.6(a) shows a SEM image of a 100 × 30 μm region of Si nanopillars without any Si wafer on top, where the top row has nanopillars in the shape of a cylinder, while

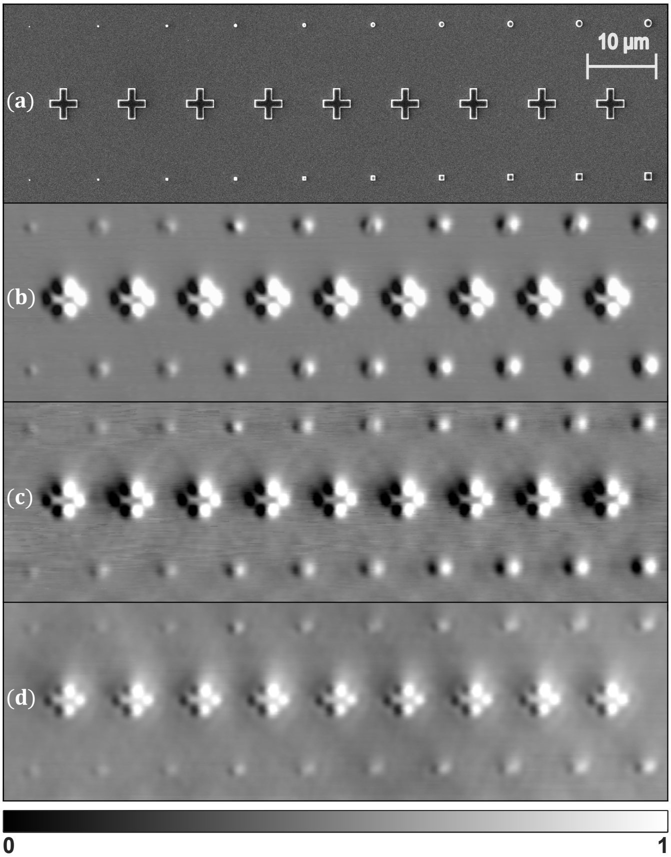

Figure 4.6: (a) SEM image of a 100 × 30 µm region showing the Si nanopillars with no overlying wafer. (b) CFS scan of the same region with no overlying wafer. (c) CFS scan of the same region with a 300 µm thick Si wafer on top. (d) CFS scan of the same region with a 500 µm thick Si wafer on top.

the bottom row has nanopillars in the shape of a square; the nanopillars have dimensions ranging from 100 nm to 1000 nm (from left to right). The middle row has markers in the shape of '+'. Figures 4.6(b)-(d) shows the corresponding 100 × 30 µm CFS scans of nanopillars: (b) without Si wafer on top; (c) with 300 µm Si wafer on top; and (d) with 500 µm Si wafer on top. We can observe that even the 100 nm ($\sim \lambda/10$) nanopillars are detected in all the different cases, showcasing the capability of CFS to detect ≥100 nm nanopillars buried under 500 µm of Si. In Table 4.2, we summarize the calculated SNR based on Eq. 4.2, for all the different dimensions of nanopillars and different cases. Although the SNR is high in all cases, we observe a decrease in the SNR as the dimension of the Si nanopillars becomes smaller. This is understandable as the signal/scattering strength scales with the dimension of the scatterer [24]. Additionally, the SNR reduces as the Si wafer on top becomes thicker.

Figure 4.7(a) shows a SEM image of a 50 × 50 µm region of etched nanopits without any Si wafer on top, where all rows have identical nanopits in the shape of a square, with

Table 4.2: Measured SNR of Si nanopillars sample.

Dim. (nm)	SNR_{dB} Without Si wafer on top	With 300 μm Si wafer on top	With 500 μm Si wafer on top
100	12.23	5.91	5.85
200	15.23	12.26	6.64
300	15.32	11.82	6.51
400	19.90	16.20	13.69
500	20.03	15.73	11.77
600	19.76	15.79	10.25
700	21.27	17.69	9.51
800	21.97	18.26	10.97
900	21.69	17.72	12.83
1000	22.15	18.84	13.48

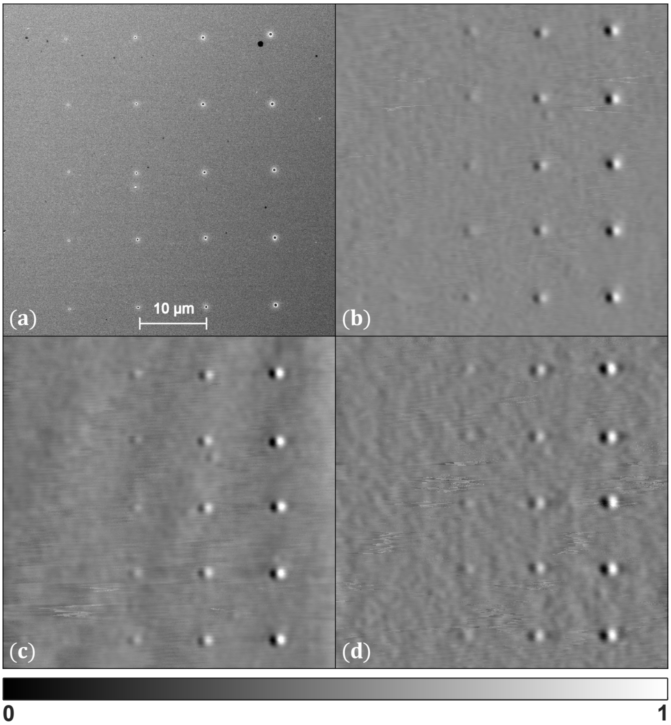

Figure 4.7: (a) SEM image of a 50 × 50 μm region showing the etched nanopits with no overlying wafer. (b) CFS scan of the same region with no overlying wafer. (c) CFS scan of the same region with a 300 μm thick Si wafer on top. (d) CFS scan of the same region with a 500 μm thick Si wafer on top.

dimensions ranging from 125 nm to 425 nm (from left to right). Figures 4.7(b)-(d) shows the corresponding 50 × 50 µm CFS scans of nanopits: (a) without Si wafer on top; (c) 300 µm Si wafer on top; and (d) with 500 µm Si wafer on top. We can observe that even the 125 nm ($\sim \lambda/10$) nanopillars are detected, in Fig. 4.7(b), where the top Si wafer is not present. However, for all the other cases with the Si wafer on top, we cannot detect 125 nm etched nanopits. This can be due to the aberrations introduced by the intervening Si, which degrade the focus spot and reduce the scattered signal from the nanopits. In contrast, 100 nm nanopillars are detectable under similar conditions, likely due to their greater vertical extent and scattering volume, which enhances their interaction with the focal field and results in a stronger scattered signal. Nevertheless, nanopits with dimensions ≥225 nm remain detectable even through 500 µm of Si. It is important to note that the split detector provides differential contrast based on far-field asymmetry, enabling detection of subwavelength features. However, it does not distinguish between different defect types, such as nanopits and nanopillars, since both produce similar asymmetry signatures. Our approach is focused on universal detection of buried nanoscale features, rather than classification. In Table 4.3, we summarize the calculated SNR based on Eq. 4.2, for all the different dimensions of nanopits and different cases. Similar to the nanopillars, we observe that the SNR decreases as the dimension of the Si nanopits becomes smaller, and as the Si layer becomes thicker.

Table 4.3: Measured SNR of etched nanopits sample.

	$\mathrm{SNR}_{\mathrm{dB}}$		
Dim. (nm)	**Without Si wafer on top**	**With 300 µm Si wafer on top**	**With 500 µm Si wafer on top**
125	4.07	-	-
225	12.20	10.13	4.92
325	16.64	14.37	13.84
425	19.94	16.95	16.87

4.2.2. INSPECTION OF GRATINGS

In this section, we demonstrate the inspection of diffraction gratings buried within Si wafer using CFS. For that, we inspect a diffraction grating defined by geometrical parameters: period (p) = 1430 nm, line width (w) = p/2, height (h) = 160 nm, and bias (b). b is a parameter that is introduced to define the relative position of the grating to the optical axis of the focused beam. Although the definition of the position $b = 0$ can be arbitrary, we define it as the center of the grating line. When the grating interacts with a focused beam, the incident beam is diffracted into multiple diffraction orders, as described by the grating equation. Each diffracted order is mapped to the Fourier plane (the mapping is limited by the NA), where a CMOS camera captures them. A more detailed discussion on the diffraction theory for CFS is provided in Section 2.1.1. For the inspection of gratings, as discussed in Section 4.1.4, we operate the laser below the lasing threshold ($L_c^{\text{non-lasing}}$ = 61.83 µm), with 2.5 μW of lasing power. This broadens the laser linewidth and reduces the temporal coherence of the illumination, which is critical for suppressing interference between the air–Si interface reflection and the grating diffraction orders. We

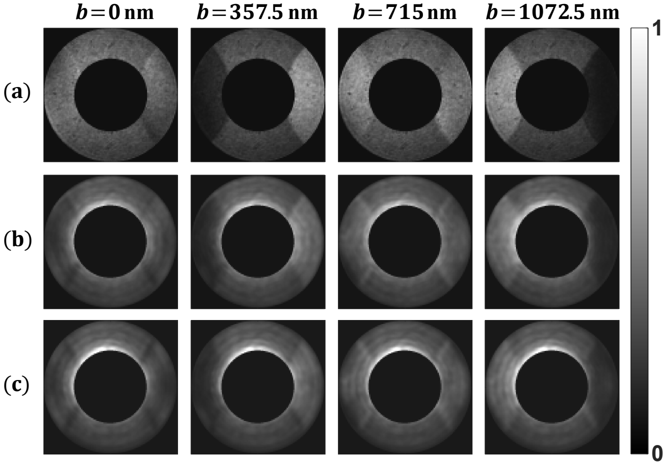

Figure 4.8: Far-field signatures of grating with period (p) of 1430 nm, at four bias positions ($b = 0$ nm, 357.5 nm, 715 nm, 1072.5 nm); (a) with no overlying wafer, (b) with a 300 µm thick Si wafer on top, and (c) with a 500 µm thick Si wafer on top.

also use a spatial filter in the form of a pinhole to remove the reflected signal from the air-Si interface. This blocks most of the unwanted signal coming from the defocused planes, however, some residual light passes through the center of the pinhole, appearing in the central part of the far-field. For this, we crop the central region of the far-field signatures. Similar to our previous measurements with 400 nm PSL nanospheres, we begin by measuring the grating in its exposed state (without any Si wafer on top). We then place Si wafers of 300 µm and 500 µm thickness on top to simulate different degrees of buriedness, adjusting the focal plane via the $z-$axis translation stage as detailed in Section 4.1.2. The sample is mounted on an XYZ piezo stage such that the grating lines are parallel to the $y-$axis at the pupil, and the far-field is captured for various bias positions ($b = 0$ nm, 357.5 nm, 715 nm, 1072.5 nm) within one period of the grating. Figure 4.8(a) shows the far-field signatures for different bias positions without any Si wafer on top. As bias (b) is introduced, the interference between the overlapping orders changes [16], resulting in different intensities in the overlapping region. Figures 4.8(b) and 4.8(c) shows the corresponding far-field signatures for different bias positions with 300 µm and 500 µm thick Si wafer on top, respectively. We observe that for all the different cases, we obtain the same complete far-field information without any unwanted interference from reflections at the air-Si interface, showcasing the capability of CFS to inspect gratings buried below through 500 µm of Si.

4.3. SUMMARY

In this chapter, we extended coherent Fourier scatterometry (CFS) beyond surface inspection to enable non-destructive detection and characterization of deeply buried nanostructures within silicon substrates. By operating CFS in the near-infrared regime, where silicon is transparent, and optimizing the source coherence and spatial filtering, we suppressed unwanted interface reflections and enhanced sensitivity to weak subsurface scattering. This approach enabled the detection of various subwavelength features, including nanoparticles, nanopillars, nanopits, and buried gratings, even under silicon layers up to 500 µm thick. The results demonstrate that CFS can overcome the diffraction and depth limitations of conventional techniques, offering a versatile, high-throughput solution for subsurface metrology in advanced 3D integration, bonded overlay applications, and multilayer device inspection.

BIBLIOGRAPHY

[1] Anubhav Paul, Mathijs Boonstra, and Silvania F. Pereira. "Near-infrared coherent Fourier scatterometry for deep subsurface nanostructure metrology in silicon". In: *Optics and Lasers in Engineering* 195 (2025), p. 109354. DOI: 10.1016/j.optlaseng.2025.109354.

[2] Elisabeth Mansfield et al. *International Roadmap for Devices and Systems^{TM} 2023 Edition Metrology*. 2023. URL: https://irds.ieee.org/editions/2023.

[3] J Bogdanowicz et al. "3D metrology and inspection to enable the rise of stacked transistors, wafers, and chips". In: *Metrology, Inspection, and Process Control XXXIX*. Vol. 13426. SPIE. 2025, pp. 8–15. DOI: 10.1117/12.3052399.

[4] Yan Li and Deepak Goyal. *3D Microelectronic packaging: from architectures to applications*. Vol. 64. Springer Nature, 2020. DOI: 10.1007/978-981-15-7090-2.

[5] Gajendra S Shekhawat and Vinayak P Dravid. "Nanoscale imaging of buried structures via scanning near-field ultrasound holography". In: *Science* 310.5745 (2005), pp. 89–92. DOI: 10.1126/science.1117694.

[6] Ivan Kassamakov et al. "Nondestructive inspection of buried channels and cavities in silicon". In: *Journal of Microelectromechanical Systems* 22.2 (2012), pp. 438–442. DOI: 10.1109/JMEMS.2012.2227460.

[7] C Schmidt. "3-D X-Ray imaging with nanometer resolution for advanced semiconductor packaging FA". In: *IEEE Transactions on Components, Packaging and Manufacturing Technology* 8.5 (2018), pp. 745–749. DOI: 10.1109/TCPMT.2018.2827058.

[8] Dalia Yablon. *Metrology capabilities keep up with semiconductor industry push into 3D integrated circuits (Part 1)*. 2024. URL: https://analyticalscience.wiley.com/content/article-do/metrology-capabilities-keep-%E2%80%A8up-semiconductor-industry-push-into-3d-integrated-circuits.

[9] BAJ Quesson et al. "Feasibility of detecting and imaging deeply buried voids using GHz Half Wavelength Contact Acoustic Microscopy". In: *2024 IEEE Ultrasonics, Ferroelectrics, and Frequency Control Joint Symposium (UFFC-JS)*. IEEE. 2024, pp. 1–3. DOI: 10.1109/UFFC-JS60046.2024.10793492.

[10] Romain Duru et al. "Photoluminescence for in-line buried defects detection in silicon devices". In: *2017 28th Annual SEMI Advanced Semiconductor Manufacturing Conference (ASMC)*. IEEE. 2017, pp. 262–266. DOI: 10.1109/ASMC.2017.7969241.

[11] Kuniko Kimura et al. "Imaging of Au nanoparticles deeply buried in polymer matrix by various atomic force microscopy techniques". In: *Ultramicroscopy* 133 (2013), pp. 41–49. DOI: 10.1016/j.ultramic.2013.04.003.

[12] Gajendra Shekhawat et al. “Ultrasound holography for noninvasive imaging of buried defects and interfaces for advanced interconnect architectures”. In: *Applied Physics Letters* 95.26 (2009). DOI: `10.1063/1.3263716`.

[13] Lay Wai Kong et al. “Sub-imaging techniques for 3D-interconnects on bonded wafer pairs”. In: *AIP Conference Proceedings*. Vol. 1300. 1. American Institute of Physics. 2010, pp. 221–228. DOI: `10.1063/1.3527129`.

[14] Andrew C Rudack, Lay Wai Kong, and Greg G Baker. “Infrared microscopy for overlay and defect metrology on 3d-interconnect bonded wafers”. In: *2010 IEEE/SEMI Advanced Semiconductor Manufacturing Conference (ASMC)*. IEEE. 2010, pp. 347–352. DOI: `10.1109/ASMC.2010.5551481`.

[15] Alastair Trigg. “Applications of infrared microscopy to IC and MEMS packaging”. In: *IEEE Transactions on Electronics Packaging Manufacturing* 26.3 (2004), pp. 232–238. DOI: `10.1109/TEPM.2003.820807`.

[16] Nitish Kumar et al. “Reconstruction of sub-wavelength features and nano-positioning of gratings using coherent Fourier scatterometry”. In: *Optics Express* 22.20 (2014), pp. 24678–24688. DOI: `10.1364/OE.22.024678`.

[17] S. Roy et al. “Coherent Fourier scatterometry for detection of nanometer-sized particles on a planar substrate surface”. In: *Optics Express* 22.11 (2014), pp. 13250–13262. DOI: `10.1364/OE.22.013250`.

[18] Jeffrey P Gambino, Shawn A Adderly, and John U Knickerbocker. “An overview of through-silicon-via technology and manufacturing challenges”. In: *Microelectronic Engineering* 135 (2015), pp. 73–106. DOI: `10.1016/j.mee.2014.10.019`.

[19] Hao Ling and Shung-Wu Lee. “Focusing of electromagnetic waves through a dielectric interface”. In: *Journal of the Optical Society of America A* 1.9 (1984), pp. 965–973. DOI: `10.1364/JOSAA.1.000965`.

[20] Ansys *Zemax OpticStudio*. Available from `https://www.ansys.com/products/optics/ansys-zemax-opticstudio`.

[21] Joseph Braat. “Analytical expressions for the wave-front aberration coefficients of a tilted plane-parallel plate”. In: *Applied Optics* 36.32 (1997), pp. 8459–8467. DOI: `10.1364/AO.36.008459`.

[22] Anubhav Paul et al. “Utilizing focused field as a probe for shape determination of subwavelength structures via coherent Fourier scatterometry”. In: *Physical Review Applied* 23.2 (2025), p. 024016. DOI: `10.1103/PhysRevApplied.23.024016`.

[23] T Siefke et al. “Fine details of structural deviations in reference samples for scatterometry”. In: *Proc. Of 19th IMEKO TC10 Conference MACRO Meets NANO in Measurement for Diagnostics, Optimization and Control*. 2023. DOI: `10.21014/tc10-2023.021`.

[24] D. Kolenov et al. “Direct detection of polystyrene equivalent nanoparticles with a diameter of 21 nm ($\sim \lambda/19$) using coherent Fourier scatterometry”. In: *Optics Express* 29.11 (2021), pp. 16487–16505. DOI: `10.1364/OE.421145`.

5

DIMENSIONAL METROLOGY OF CLIFF-LIKE NANOSTRUCTURES

This chapter presents a metric-driven approach using coherent Fourier scatterometry (CFS) for the quantitative characterization of height and steep sidewall angles (swa) in cliff-like nanostructures. Unlike conventional scatterometry techniques that rely on complex inverse modeling, our method employs a far-field parameter, termed "visibility", to directly relate scattering signatures to structural dimensions. The approach enables robust, non-destructive dimensional metrology of aperiodic features, with sensitivity validated against atomic force microscopy (AFM). This methodology represents a significant step toward simplified, high-throughput nanoscale calibration without extensive modeling requirements.

Parts of this chapter have been published in Measurement Science & Technology **35**(7), 075202 (2024) [1].

In the previous chapters, we demonstrated the versatility of coherent Fourier scatterometry (CFS) as a powerful optical metrology tool for detecting nanoscale defects on patterned surfaces, investigating edge-proximal sensitivities, and even probing deeply buried structures. These studies established CFS as a sensitive, non-invasive, and high-throughput approach for various inspection challenges. However, beyond defect detection, another challenge of semiconductor metrology lies in the precise *geometrical characterization* of nanostructures, specifically their height and steep sidewall angles (swa). This chapter addresses this complementary but distinct challenge.

The fabrication of nanostructures with accurate height and steep swa is crucial for advanced semiconductor devices, particularly in lithography mask fabrication and pattern transfer processes [2–4]. Even minor deviations in these parameters can lead to shadowing effects during etching, misalignment of printed features, and ultimately device failure [5–7]. Accurate and robust measurement of these structural parameters is therefore fundamental for yield, performance, and reliability.

5.1. METHOD

5.1.1. THEORY

In this section, we provide a detailed description of the nanostructure under investigation and the associated diffraction theory. The nanostructure in consideration consists of a cliff-like configuration with well-defined swa and height. In Fig. 5.1(a) a 2D representation of the nanostructure is schematically shown. The nanostructure is fully characterized by the geometrical parameters: swa and height (h). We introduce an additional parameter b which denotes the projection of the cliff on the $x-$axis, with $b = 0$ implying that the nanostructure has $swa = 90°$. We define a coordinate system (x, y, z) to describe the geometry of the nanostructure, with the nanostructure being infinite along the $x-$axis and invariant along the $y-$axis. Now the profile of the nanostructure can be expressed as

$$z(x) = \begin{cases} -h, & \text{if } x \leq -b, \\ x\tan(swa) - \dfrac{h}{2}, & \text{if } |x| < b, \\ 0, & \text{if } x \geq +b. \end{cases} \tag{5.1}$$

The nanostructure described above can be assumed to act as a pure phase object i.e., a phase step if the slope of the cliff is steep enough [8]. When the phase step interacts with an illuminating focused beam, as shown in Fig. 5.1(b), the beam will encounter different path differences across the cliff, and the resulting scattered beam will experience different offsets depending on the reflection function of the nanostructure. For our nanostructure, the reflection function can be expressed as

$$r_{\mathrm{f}}(x) = r \begin{cases} \exp(-2ikh), & \text{if } x \leq -b, \\ \exp\left(2ik\left(x\tan(swa) - \frac{h}{2}\right)\right), & \text{if } |x| < b, \\ 1, & \text{if } x \geq b, \end{cases} \tag{5.2}$$

where k is the length of the wave vector equal to $2\pi/\lambda$ and r(with $|r| \leq 1$) is the Fresnel reflection coefficient of the nanostructure. In the angular spectrum decomposition

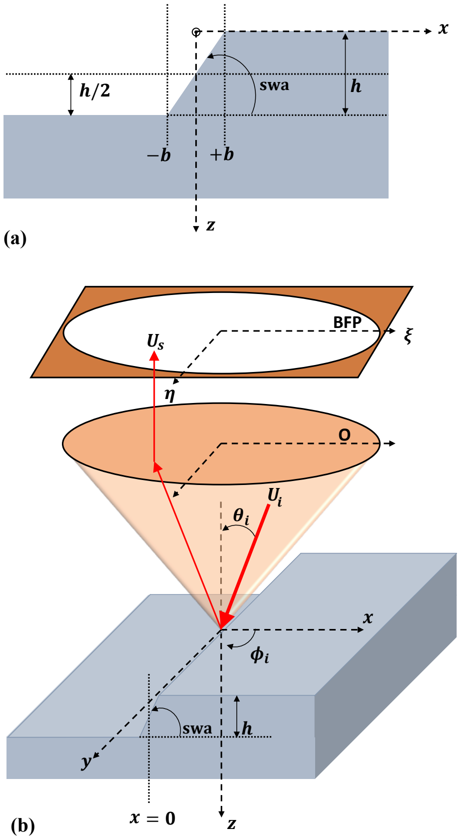

Figure 5.1: (a) Geometrical representation of the cliff-like nanostructure under investigation. (b) Schematic representation of the cliff-like nanostructure, scattering an incident beam (U_i). The scattered beam (U_s) is captured by a microscope objective (O) having numerical aperture (NA) and propagated to the back focal plane (BFP).

formalism, a focused beam can be decomposed into an infinite number of plane waves of different propagation directions [9]. Let us consider a plane wave (defined by U_i, θ_i, ϕ_i) incident on the nanostructure. The nanostructure (defined by r_f) scatters the incident plane wave, which is captured by a microscope objective (O) having numerical aperture (NA), which further propagates it to the back focal plane (BFP) (having coordinate system (ξ, η)) based on the Fourier optics theory [10]. The scattered field propagated to the BFP is given by

$$\begin{aligned} U_s(\xi,\eta) = \quad & \frac{1}{\lambda f}\exp(2ikf)\int_{-\infty}^{\infty} U_i(x,y)\, r_f(x)\times \\ & \exp\left[-2\pi i\left(\frac{\xi}{\lambda f}x+\frac{\eta}{\lambda f}y\right)\right] \mathrm{d}x\,\mathrm{d}y, \end{aligned} \tag{5.3}$$

where f is the focal length of the objective, and λ is the wavelength of the incident plane wave. Now, if we take into account the scattering from the nanostructure for all plane waves of different propagation directions, each θ_i and ϕ_i will correspond to a distinct point in the BFP. However, it's important to note that this mapping is constrained by the NA of the objective.

5.1.2. EXPERIMENTAL SETUP

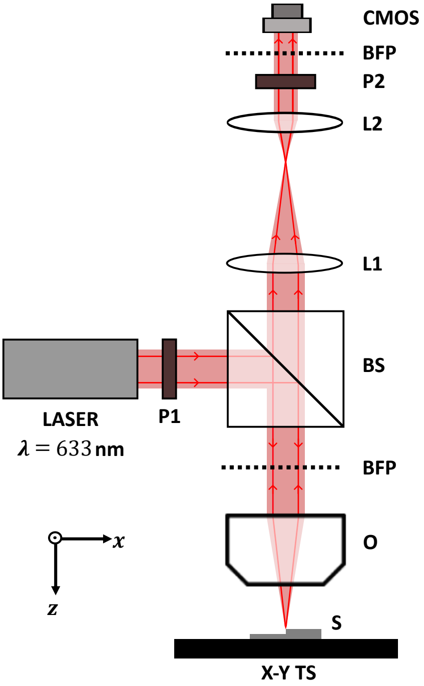

Figure 5.2: Schematic of the experimental setup of coherent Fourier scatterometry (CFS).

In this section, we illustrate the experimental setup of CFS used in this chapter. Its general schematic is shown in Fig. 5.2. To begin, a collimated He-Ne laser with a wavelength of $\lambda = 633$ nm is utilized for illumination. The collimated laser beam first passes through a linear polarizer (P1). The linearly polarized beam passes through a non-polarizing beam splitter (BS), and then it is directed towards a microscope objective (O) with an NA of 0.4. The objective focuses the beam onto the cliff-like nanostructure sample (S). The sample is positioned on a piezo-controlled translation stage (X-Y TS), which is controlled to localize the region of interest in the S and allows for precise observation. The scattered light from the sample is collected and directed back through the objective and again passes through the BS. We further incorporate a telescopic setup comprising two lenses (L1 and L2) to de-magnify the Fourier plane of the objective, directing the light towards a complementary metal-oxide-semiconductor (CMOS) camera. We can choose the output polarization at the CMOS with the help of a second linear polarizer (P2). This approach enables the simultaneous detection of the angular spectrum for all scattered waves from every incident plane wave within the focused spot.

With the help of P1 and P2, we can choose between two orthogonal configurations of polarization, TE and TM. We use these two polarization configurations throughout all experiments and simulations in this work. Here, TE polarization means that the polarization direction of P1 at the pupil is parallel to the invariant direction of the structure (i.e., $y-$axis). Consequently, TM polarization means that the polarization direction of P1 at the pupil is perpendicular to the invariant direction of the structure (i.e., $y-$axis). P2 is always aligned parallel to P1.

5.1.3. NUMERICAL MODEL

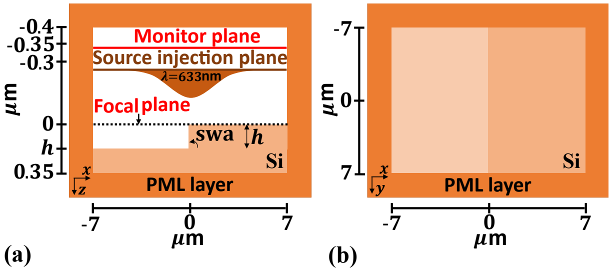

Figure 5.3: The 3D-FDTD simulation scheme of a cliff-like nanostructure characterized by geometrical parameters: swa and h, being illuminated by a TE or TM polarized focused spot of wavelength 633 nm. The corresponding $y = 0$ plane in (a). The corresponding $z = 0$ plane in (b).

The intricate electromagnetic interaction between a focused beam and a nanostructure characterized by steep swa presents a significant challenge. To tackle this complex problem, we employed rigorous 3D electromagnetic simulations, specifically the finite difference time domain (3D-FDTD) method, employing the software package Lumerical FDTD [11]. Within the FDTD framework, Maxwell's equations are solved on discretized Yee grids (i.e., spatial and temporal grids) in the time domain.

In our simulations, we replicate the experimental conditions by modeling a cliff-like nanostructure invariant along one direction (along $y-$axis) and profile variation along the orthogonal direction (along $x-$axis), as the simulation object. The dimension of the simulation domain is chosen to ensure that the width of the focused beam (FWHM ~ 818 nm) remains significantly smaller than the dimension of the simulation domain (=14 µm). Perfectly matched layer (PML) boundary conditions are applied to all boundaries to prevent reflections. For the illumination scheme, we used the vectorial diffraction theory of Richards and Wolf [12, 13] to employ a TE polarized (i.e., the polarization direction at the pupil is parallel to the invariant direction of the nanostructure) or TM polarized (i.e., the polarization direction at the pupil is perpendicular to the invariant direction of the nanostructure) plane wave of wavelength $\lambda = 633$ nm being focused by a microscope objective of numerical aperture 0.4 onto the focal plane (we choose our focal plane to be at the top layer of the cliff-like nanostructure). The scattered near field emanating from the simulation object is computed and sampled at the monitor plane, thereafter propagating it into the far-field through the FDTD simulation.

In Fig. 5.3(a), the $y = 0$ plane, and in Fig. 5.3(b), the $z = 0$ plane of the complete 3D-FDTD model is depicted. The simulation object's geometry is characterized by the geometrical parameters, swa and height (h). The nanostructure's material is silicon (Si) with a refractive index of $n = 3.88126 + 0.01894i$. To investigate the impact of varying the geometrical parameters of the cliff-like nanostructure on the far-field signatures, we systematically sweep swa (ranging from 70° to 100°) and h (ranging from 100 to 300 nm), while keeping the position of the source injection plane, monitor plane, and computational domain constant.

5.1.4. SAMPLE PREPARATION

The sample has been fabricated at the TU Delft clean room and it consists of a 2x2 mm square etched on a silicon wafer.

5.2. RESULTS

5.2.1. FAR-FIELD INTENSITY PATTERN AND DEFINITION OF VISIBILITY

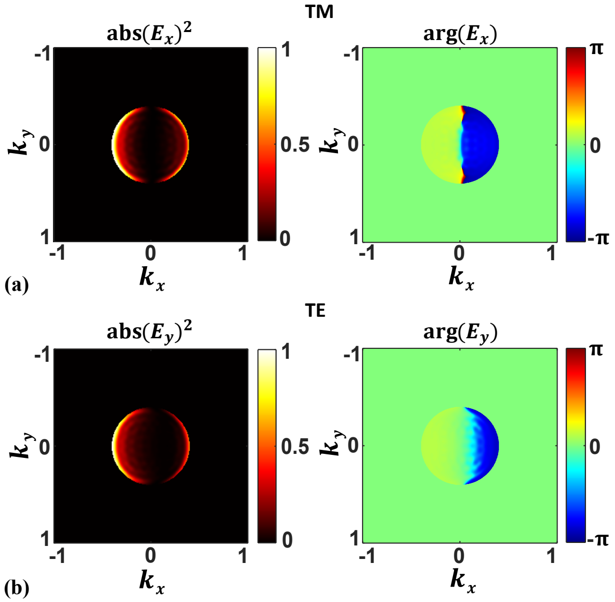

Figure 5.4: (a) Simulated normalized far-field intensity (on the left) and phase (on the right) for a cliff-like nanostructure with geometrical parameters: $swa = 90°$ and $h = 150$ nm, being illuminated by a TM polarized focused spot having $\lambda = 633$ nm. (b) Corresponding far-field intensity (on the left) and phase (on the right) for the same nanostructure illuminated by a TE polarized focused spot having $\lambda = 633$ nm.

In this section, we perform numerical investigations to understand the electromagnetic interaction of a cliff-shaped nanostructure with that of a linearly polarized focused beam, with the nanostructure being defined by the parameters: swa and h. To understand this phenomenon, let us consider one such nanostructure with parameters: $swa = 90°$ and $h = 150$ nm. For the study, we have used rigorous 3D FDTD simulations as already discussed. In Fig. 5.4(a) we have shown the normalized far-field intensity pattern (on the left) and the corresponding wrapped phase (on the right) for the TM polarized incident beam. Similarly, in Fig. 5.4(b) we have shown the normalized far-field intensity pattern (on the left) and the corresponding wrapped phase (on the right) for the TE polarized incident beam. Here, we observe two asymmetric radiation fields along the $x-$axis i.e., along the direction of variation in the nanostructure profile, with the central region of the far-field experiencing weak radiation because of the interference of the beam that is scattered by the two halves of the nanostructure [14]. Further, we observe a phase jump along the nanostructure induced by the height variation (which produces the phase variation) of the nanostructure. While the far-field intensity patterns appear similar for both TE and TM polarizations, there are variations in the intensities of the two asymmetric peaks. This discrepancy arises as a consequence of the distinct treatment of TE and TM polarized beams due to the electromagnetic boundary conditions, i.e., the continuity in both tangential components and their derivatives of the electric fields [15].

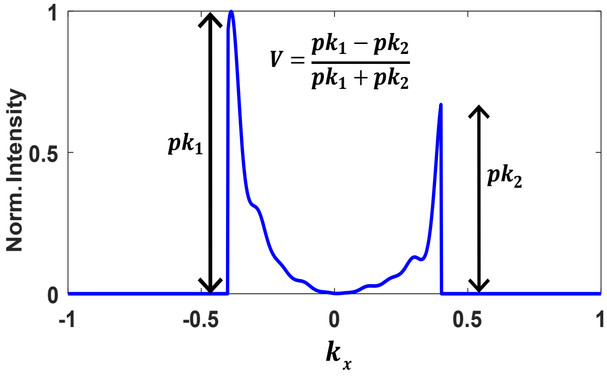

Figure 5.5: Schematic describing the quantity visibility (V) parameter.

We introduce the concept of “visibility” (V) as a quantitative parameter that characterizes the relative contrast between the two distinct radiation fields observed in the far-field intensity pattern. The V is a parameter that depends on the swa and the height of the nanostructure. As the geometrical parameters of the nanostructure are varying the V will vary providing us with a unique means for calibration. A similar calibration of nanoparticle size has been performed by Kolenov *et al.* [16]. In Fig. 5.5, we illustrate the procedure for calculating V applicable to any normalized far-field intensity pattern of a cliff-shaped nanostructure. Initially, we examine the cross-section along the $k_y = 0$ plane within the normalized far-field intensity pattern. Subsequently, we designate the two radiation peaks as pk_1 (the peak corresponding to $-k_x$) and pk_2 (the peak corresponding to $+k_x$). Finally, the parameter V is quantitatively determined through the following mathematical expression:

$$V = \frac{pk_1 - pk_2}{pk_1 + pk_2}. \tag{5.4}$$

This quantitative parameter V allows us the further possibility to optimize the experimental setup, where instead of utilizing a CMOS camera we can replace it with a set of single-pixel detectors positioned along the k_x-axis which measures pk_1 and pk_2 separately while yielding the quantity V. This in turn will reduce the noises associated with the CMOS camera, further reducing the computation associated with quantifying V from a far-field intensity map.

5.2.2. Numerical calibration of CFS for steep SWA and height

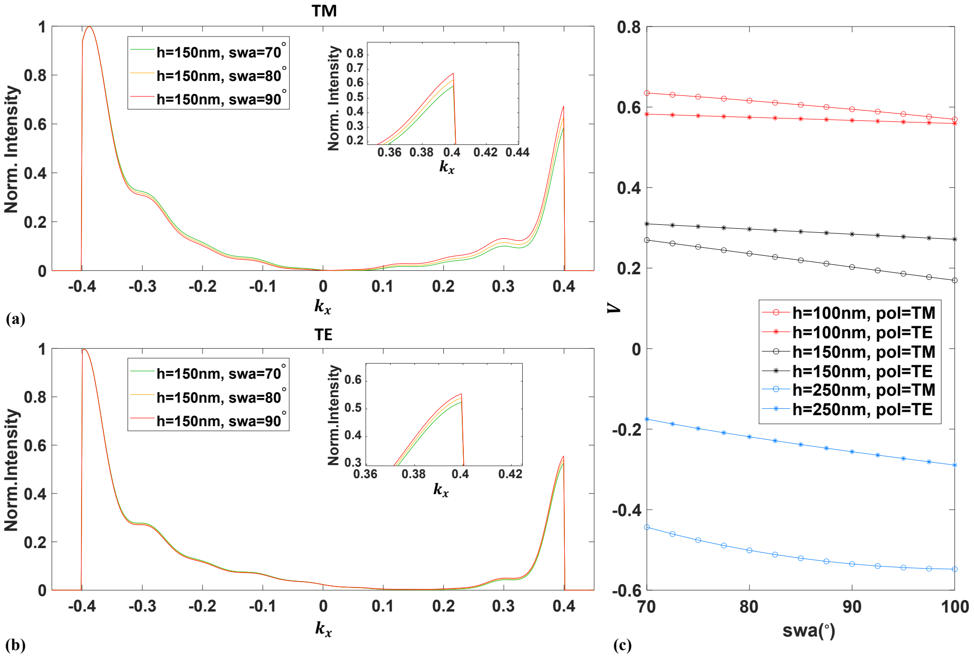

Figure 5.6: (a) Normalized $k_y = 0$ plane plotted for three different cliff-like nanostructures with different $swa(= 70^\circ, 80^\circ$, and $90^\circ)$ but fixed $h(= 150$ nm), when illuminated by TM polarized beam. (b) Normalized $k_y = 0$ plane plotted for three different cliff-like nanostructures with different $swa(= 70^\circ, 80^\circ$, and $90^\circ)$ but fixed $h(= 150$ nm), when illuminated by TE polarized beam. (c) Calibration curves of swa are shown for three different $h(= 100$ nm, 150 nm, and 250 nm) for TE and TM polarized incident illumination schemes.

In this section, we investigate the influence of the two geometrical parameters, namely the steep swa and the height (h), on the far-field intensity patterns exhibited by the cliff-like nanostructure when subjected to illumination from a linearly polarized focused beam. Our investigation encompasses two distinct aspects: the impact of variation in swa and the impact of variation in h, each considered independently. To explore these effects comprehensively, we systematically vary the swa over a range spanning 70° to 100° while varying h within the range of 100 nm to 300 nm for separate analyses.

Let us first explore the effects of swa on the far-field intensity pattern of the cliff-like nanostructure. In Fig. 5.6(a) we have shown the far-field intensity pattern cross-section in $y = 0$ plane, normalized to the maximum intensity of each pattern, for cliff-like nanostructure with varying $swa(= 70^\circ$(green curve), 80°(amber curve), and 90°(red curve)) while maintaining a constant $h(= 150$ nm), for a TM polarized incident illuminating beam. Here, we observe that there is a significant difference in the value $pk_1 - pk_2$ for the different swa, resulting in different values of V. Consequently, in Fig. 5.6(b) we have shown the analogous cross-sections for the same cliff-like nanostructure parameters but under TE polarized incident illumination. Although differences in $pk_1 - pk_2$ persist across varying swa, the differences are comparatively smaller than those observed in the TM polarized scenario. This implies that TM polarization exhibits greater sensitivity to alterations in swa than its TE counterpart. Further, we perform a comprehensive study to understand the trend of change due to the impact of swa by sweeping it in the range spanning 70° to 100°, with the parameter V calculated for three different heights (h = 100 nm (red curve), 150 nm (black curve), and 250 nm (blue curve)) as shown in Fig. 5.6(c). Notably, asterisk-marked curves signify TE polarization, while curves marked with circles represent TM polarization. We observe that for the different heights, TM polarization is more sensitive to changes in the swa. This sensitivity is further accentuated with increasing height, attributing this trend to the increased lateral shadow accompanying the growth of the nanostructure's height.

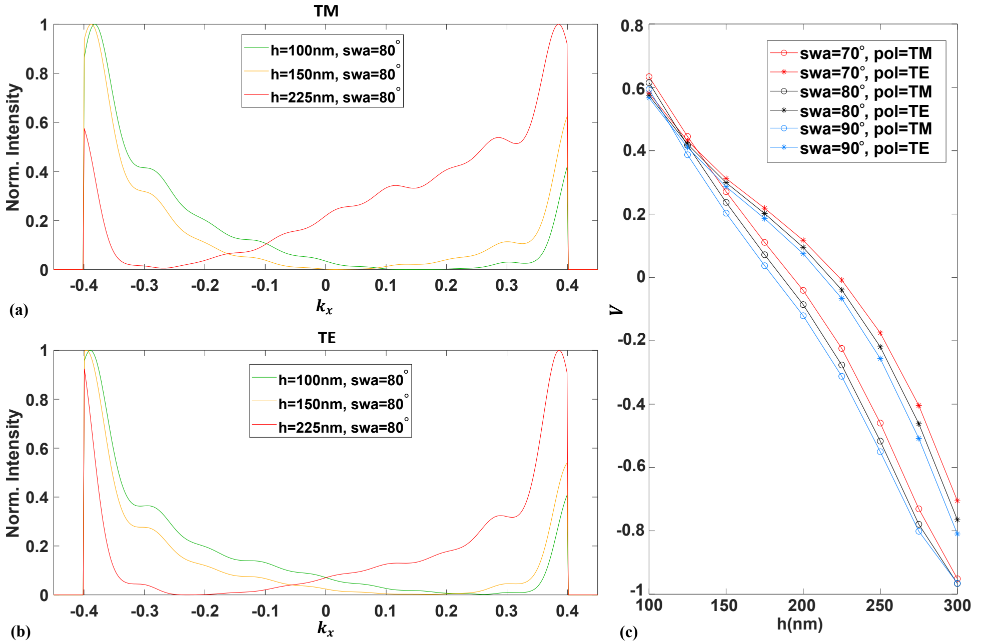

Figure 5.7: (a) Normalized $k_y = 0$ plane plotted for three different cliff-like nanostructures with different h(= 100 nm, 150 nm, and 225 nm) but fixed swa(= 80°), when illuminated by TM polarized beam. (b) Normalized $k_y = 0$ plane plotted for three different cliff-like nanostructures with different h(= 100 nm, 150 nm, and 225 nm) but fixed swa(= 80°), when illuminated by TE polarized beam. (c) Calibration curves of h are shown for three different swa(= 70°, 80°, and 90°) for TE and TM polarized incident illumination schemes.

Now, let us investigate the effects of varying h on the far-field intensity pattern of the cliff-like nanostructure. In this context, altering h introduces a corresponding modification in the phase difference between the scattered fields emanating from distinct height levels within the structure, resulting in variation in the far-field intensities. For the scenario where $h = \lambda/4$ and $swa = 90°$, a phase shift of π is introduced, resulting in destructive interference between the scattered beams emanating from different regions within the structure. Similarly, when $h = \lambda/2$ and $swa = 90°$, a phase shift of 2π leads to constructive interference, rendering the change in h inconspicuous to the incident beam. As we vary the h, deviations from these distinctive cases become apparent. In Fig. 5.7(a) we have shown the normalized far-field intensity pattern cross-section in $y = 0$ plane, for cliff-like nanostructure with varying h(= 100 nm (green curve), 150 nm (amber curve), and 225 nm(red curve)) while maintaining a constant swa(= 80°), for a TM polarized incident illuminating beam. Here, we observe that there is a more pronounced difference in the value $pk_1 - pk_2$ for the different h compared to the variations induced by changing swa. An intriguing observation emerges at $h = 225$ nm where the far-field seems to flip i.e., $pk_1 < pk_2$, this is due to the fact that at this h we have a phase difference surpassing π. Consequently, in Fig. 5.7(b) we have shown the analogous cross-sections for the same cliff-like nanostructure parameters but under TE polarized incident illumination. Here, we observe that the difference in the value $pk_1 - pk_2$ is comparably substantial for both TE and TM polarizations, suggesting that the variation in h is sensitive for both the polarizations states. Further, we perform a comprehensive study to understand the trend of change due to the impact of h by sweeping it in the range spanning 100 nm to 300 nm, with the parameter V calculated for three different swa(= 70°(red curve), 80°(black curve), and 90°(blue curve)) as shown in Fig. 5.7(c). The curves marked with asterisks denote TE polarization, while circles represent TM polarization. The quasi-periodic curves as shown in Fig. 5.7(c) stem from the interplay between the phase difference introduced by the cliff-like nanostructure among different segments of the incident beam. These findings demonstrate the capability of CFS as an adept calibration tool for precisely gauging nanostructures characterized by steep swa and varying heights (h).

5.2.3. SENSITIVITY ANALYSIS OF CFS

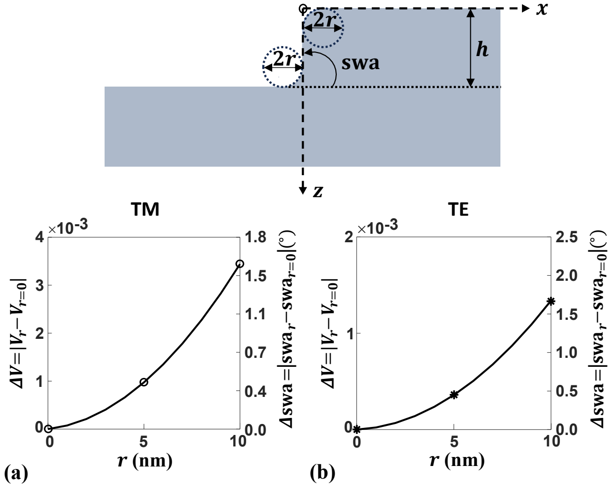

Figure 5.8: Sensitivity analysis, indicating edge roundness of 10 nm in nanostructure results in a swa variation within 1.7°.

In this section, we analyze the sensitivity of the proposed CFS method for the calibration of steep swa against the edge roundness of the cliff-like nanostructure; and the variation in the position of the cliff-like nanostructure with respect to the focused beam.

Accordingly, for the analysis of the influence of edge roundness of the cliff-like nanostructure, we introduce roundness $r(= 0$ nm to 10 nm) to the nanostructure (as shown in Fig. 5.8), for one such nanostructure with parameters: $swa = 90°$ and $h = 100$ nm. We measure the deviation introduced in V due to the roundness in the cliff-like nanostructure, by calculating ΔV, where $\Delta V = |V_r - V_{r=0}|$. Here, the subscript r denotes the roundness in the cliff-like nanostructure. In Fig. 5.8(a) we have shown the deviation introduced in V due to the roundness in the cliff-like nanostructure for TM polarized incident beam. Similarly, in Fig. 5.8(b) we have shown the deviation introduced in V due to the roundness in the cliff-like nanostructure for TE polarized incident beam. The resulting deviation in the swa measurement, denoted by Δswa, where $\Delta swa = |swa_r - swa_{r=0}|$ is represented in the vertical right axis for both plots. We observe that V varies exponentially with the edge roundness, although for edge roundness within 10 nm the resulting variation of swa is within 1.7° for both the polarization states. Such a variation of V around the edge roundness of the nanostructure confirms the robustness of the proposed CFS method implemented against unwanted roundness on the edge of the nanostructure. Further for nanostructures with larger h, the deviation in swa due to the same extent of roundness (i.e., $r = 10$ nm) will be less than 1.7°. This is due to the fact that the effective variation in the nanostructure reduces as the h increases for the same roundness. We also note that for high values of roundness, the proposed method will not be sensitive; this is understandable because as the quality of the nanostructure reduces, the definition of swa cannot be that of the ideal nanostructure.

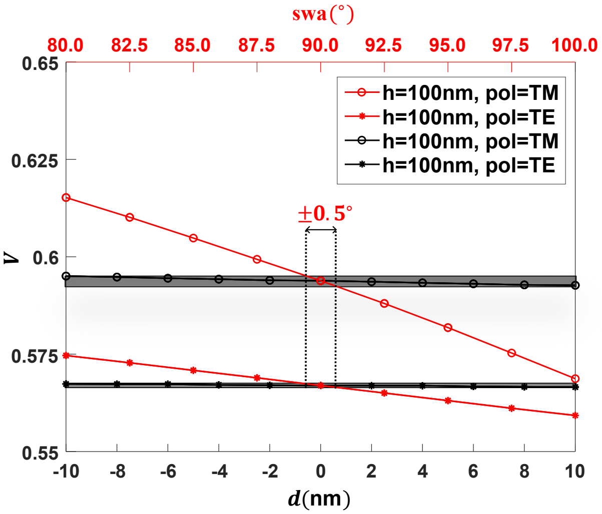

Figure 5.9: Sensitivity analysis, indicating fluctuation of ±10 nm in position of nanostructure results in a stable swa within the range of ±0.5°.

Now, we analyze the sensitivity of the proposed CFS method for the calibration of steep swa against variation in the position of the cliff-like nanostructure with respect to the focused beam. For that, we introduce a displacement $d(= -10$ nm to $+10$ nm) to the nanostructure with respect to the position $b = 0$, for one such nanostructure with parameters: $swa = 90°$ and $h = 100$ nm. In Fig. 5.9 we have shown the variation in V due to the displacement in the nanostructure position with respect to the focused beam in the horizontal bottom axis (shown in black curves), together with the swa calibration curve of the nanostructure (as shown in Fig. 5.6(c)) in the horizontal top axis (shown in red curves). The curves marked with asterisks denote TE polarization, while circles represent TM polarization. We observe that V remains unaltered even in the presence of sufficient fluctuations in the position of the nanostructure, resulting in a variation of swa within the range of $\pm 0.5°$. Here, we observe that the proposed method has a stable value for V as long as the variation in the position of the nanostructure is within 20 nm with respect to the focused beam. Such a stable value of V around the displacement in the position of the nanostructure confirms the robustness of the proposed CFS method implemented against unwanted fluctuations due to tolerances of the piezo translation stage used in the experiments.

5.2.4. EXPERIMENTAL VERIFICATION

In this section, we demonstrate the experimental verification of our numerically simulated results. For that, we measure a cliff-like nanostructure made up of material Si. Further, to establish the ground truth of the geometrical parameters of the nanostructure, the height h and swa have been independently measured by an AFM. In order to determine the steep swa value, we mounted the sample in a holder with a tilt of 60° and analyzed the measurements following Dai *et al.* [17]. In Fig. 5.10(a) we have shown the 3D visualization of the tilted-AFM measurement data. Consequently, in Fig. 5.10(b) we have shown a cross-section profile of the data (shown in black curve), where we measure the steep swa by fitting straight lines through the edge of the profile (shown in red curves) and calculating the angles between them. From the AFM data, we obtain that the geometrical parameters of the nanostructure are: $swa = 77.99° \pm 1.37°$ and $h = 148.35$ nm ± 2.11 nm. In Figs. 5.10(c) and 5.10(d) we have shown the histograms representing the variation in measurement of swa and height of the cliff-like nanostructure, respectively.

Now, to perform experimental measurements using CFS, we have used the setup as depicted in Fig. 5.2. Here, we illuminate the cliff-like nanostructure using a TE or TM polarized focused spot using a microscope objective having $NA = 0.4$. The cliff-like nanostructure sample is placed on the piezo translation stage, which is used to position the sample at the center of the optical axis of the focused beam. Finally, the scattered field is captured by the CMOS camera. In the experiment, we capture a set of five far-field intensity images for each TE and TM polarized incident beam, while moving the sample around the center of the optical axis of the focused beam, this is done because the sample cannot be aligned exactly at the center of the optical axis of the focused beam. In Fig. 5.11(a) we have shown the experimentally captured normalized far-field intensity (on the left) and corresponding closest simulated normalized far-field intensity with geometrical parameters: $swa = 77.5°$ and $h = 150$ nm (on the right). The incident illumination beam is TM polarized. Consequently, in Fig. 5.11(b) we have shown the analogous normalized

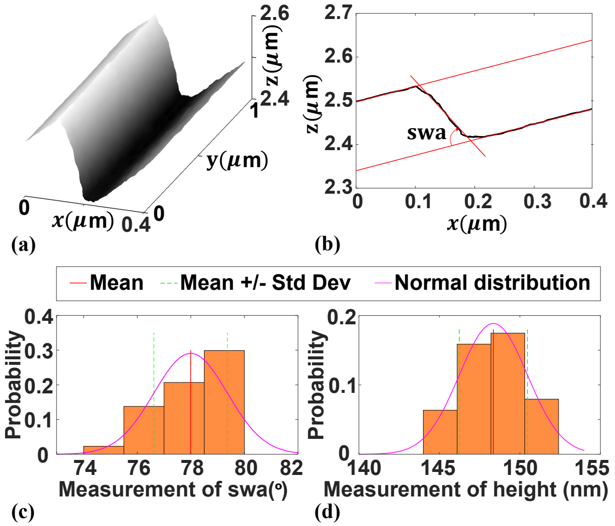

Figure 5.10: (a) 3D visualization of the tilted-AFM data. (b) A cross-section of the AFM data (shown in (a)), where we define the swa of the profile. (c) Histogram representing the variation in swa in the AFM measurement. (d) Histogram representing the variation in height (h) in the AFM measurement.

far-field intensity for the same cliff-like nanostructure parameters but under TE polarized incident illumination. Here, we observe that while exact matching between simulated and experimental far-fields was not achieved due to inherent simulation limitations and the noise in the setup, both the experimental and simulated far-fields exhibit significant agreement with each other. To further validate this concordance, in Fig. 5.11(c) we have plotted the cross-section along $k_y = 0$ the plane for both experimental (black curve) and simulated (red curve) far-field intensities for TM polarized incident illumination. Similarly, in Fig. 5.11(d) we have plotted the cross-section along the $k_y = 0$ plane for both experimental (black curve) and simulated (red curve) far-field intensities for TE polarized incident illumination. Here, we have used a moving average low pass filter on the cross-sections to reduce the high-frequency noise. We observe that pk_1 and pk_2 match roughly for both TE and TM polarization states for both experiments as well as simulations. Further, for the experimentally measured far-field intensities, the parameter V yields the value 0.241 ± 0.012 for TM polarized incident illumination and 0.299 ± 0.005 for TE polarized incident illumination. We introduce a customized Figure of Merit (FOM), analogous to the reduced χ^2 [18], defined as the FOM_{χ^2}. The FOM_{χ^2} can be calculated with, $FOM_{\chi^2} = [1/n]\sum_i^n [k_{x_i}{}^{Exp} - k_{x_i}{}^{Sim}]^2/\delta V$, where n is the total number of measurement points, k_x^{Exp} and k_x^{Sim} are the normalized cross-section along $k_y = 0$ plane of the far-field of experiment and simulation, as shown in Fig. 5.11(c) and Fig. 5.11(d), δV is the uncertainty measured in V. In our measurements, we find $FOM_{\chi^2}^{TM} = 1.85$ and $FOM\chi^{2^{TE}} = 5.4$. The calibration curve presented in Fig. 5.6(c) and Fig. 5.7(c) facilitates the determination of the height and swa value as $h = 149.42$ nm ±1.66 nm and $swa = 77.75° \pm 3.61°$ from the TM polarization calibration curve and $h = 150.05$ nm

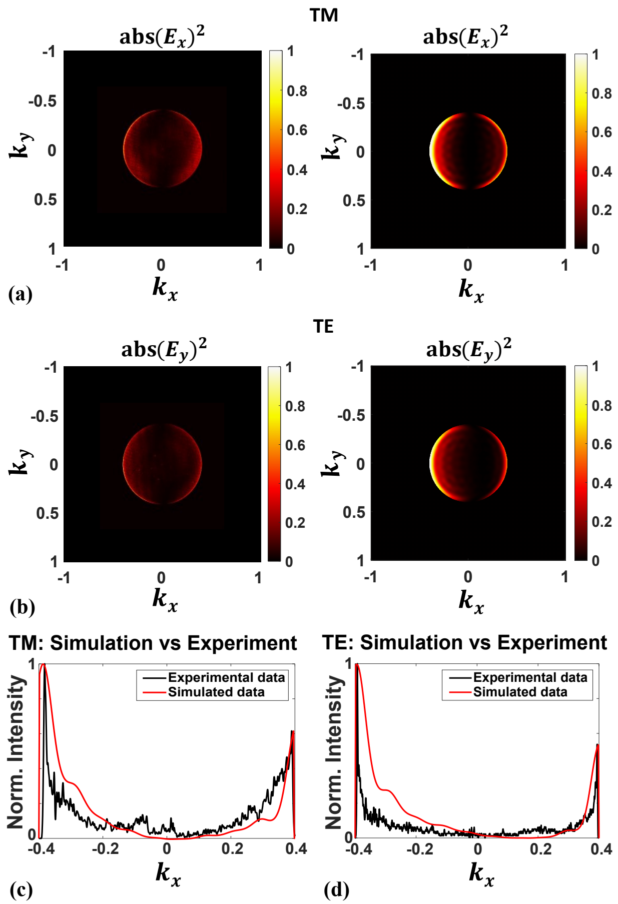

Figure 5.11: (a) Experimental and simulated normalized far-field for TM polarized incident beam. (b) Experimental and simulated normalized far-field for TE polarized incident beam. (c) Cross-section along $k_y = 0$ plane of results shown in (a). (d) Cross-section along $k_y = 0$ plane of results shown in (b).

±1.04 nm and $swa = 78.36° \pm 3.89°$ from the TE polarization calibration curve. The results experimentally demonstrate that CFS is a viable calibration tool for the measurement of the steep swa and heights (h) of cliff-like nanostructures.

5.3. SUMMARY

In this chapter, we demonstrated the extension of coherent Fourier scatterometry (CFS) from a defect-inspection technique to a robust calibration tool for the dimensional characterization of cliff-like nanostructures. Specifically, we focused on accurately measuring the height and steep sidewall angles (swa) of cliff-like features, which represent a fundamentally different challenge from those addressed in previous chapters. Through the introduction of a far-field parameter termed "visibility", we established a direct, quantitative relationship between scattering signatures and structural parameters, enabling calibration without the need for complex inverse modeling. Our experimental and simulation results showed strong agreement, validating the reliability of the proposed approach. The visibility-based method exhibited higher sensitivity to TM-polarized light for swa determination, while both TM and TE polarizations were equally sensitive for height calibration. Sensitivity analyses revealed the method's robustness, showing that fluctuations of ±10 nm in nanostructure position resulted in swa variations within ±0.5°. Additionally, edge roundness variations of 10 nm induced only minor swa deviations ($\sim 1.7°$), indicating high stability against fabrication imperfections. Further optimization could be achieved by replacing the CMOS camera with single-pixel detectors to directly compute visibility in real time. Experimental validation against AFM measurements further confirmed the accuracy of this approach. CFS-derived swa values ($77.75° \pm 3.61°$ and $78.36° \pm 3.89°$) and height measurements (149.42 nm ±1.66 nm and 150.05 nm ±1.04 nm) closely matched AFM results ($77.99° \pm 1.37°$ and 148.35 nm ±2.11 nm). While exact far-field matching between simulations and experiments was not achieved due to inherent modeling limitations, similar trends strengthened confidence in the method. The results presented here underscore the potential of CFS as a powerful, non-destructive, and high-throughput solution for dimensional metrology in advanced semiconductor manufacturing.

BIBLIOGRAPHY

[1] Anubhav Paul et al. “Investigation of coherent Fourier scatterometry as a calibration tool for determination of steep side wall angle and height of a nanostructure”. In: *Measurement Science and Technology* 35.7 (2024), p. 075202. DOI: 10.1088/1361-6501/ad3773.

[2] Bernd Hoefflinger. “ITRS: The international technology roadmap for semiconductors”. In: *Chips 2020: a guide to the future of nanoelectronics*. Springer, 2011, pp. 161–174. DOI: 10.1007/978-3-642-23096-7_7.

[3] Hans Nørgaard Hansen et al. “Dimensional micro and nano metrology”. In: *CIRP Annals* 55.2 (2006), pp. 721–743. DOI: 10.1016/j.cirp.2006.10.005.

[4] Eric Vogel. “Technology and metrology of new electronic materials and devices”. In: *Nature Nanotechnology* 2.1 (2007), pp. 25–32. DOI: 10.1038/nnano.2006.142.

[5] Wayne M Moreau. *Semiconductor lithography: principles, practices, and materials*. Springer Science & Business Media, 2012.

[6] Chris Edwards et al. “Optically monitoring and controlling nanoscale topography during semiconductor etching”. In: *Light: Science & Applications* 1.9 (2012), e30–e30. DOI: 10.1038/lsa.2012.30.

[7] Hyun-Woo Kim et al. “Experimental investigation of the impact of LWR on sub-100-nm device performance”. In: *IEEE Transactions on Electron Devices* 51.12 (2004), pp. 1984–1988. DOI: 10.1109/TED.2004.839115.

[8] Luca Cisotto, Silvania F Pereira, and H Paul Urbach. “Analytical calculation on the determination of steep side wall angles from far field measurements”. In: *Journal of Optics* 20.6 (2018), p. 065601. DOI: 10.1088/2040-8986/aabb59.

[9] Jakob J Stamnes. *Waves in focal regions: propagation, diffraction and focusing of light, sound and water waves*. Routledge, 2017.

[10] Julius Adams Stratton. *Electromagnetic theory*. Vol. 33. John Wiley & Sons, 2007.

[11] Ansys *Lumerical FDTD solutions*. Available from https://www.lumerical.com/.

[12] Bernard Richards and Emil Wolf. “Electromagnetic diffraction in optical systems, II. Structure of the image field in an aplanatic system”. In: *Proceedings of the Royal Society of London. Series A. Mathematical and Physical Sciences* 253.1274 (1959), pp. 358–379. DOI: 10.1098/rspa.1959.0200.

[13] Lukas Novotny and Bert Hecht. *Principles of nano-optics*. Cambridge university press, 2012.

[14] Xiujie Dou et al. “Determination of steep sidewall angle using polarization-sensitive asymmetric scattering”. In: *Measurement Science and Technology* 32.8 (2021), p. 085201. DOI: 10.1088/1361-6501/abfbac.

[15] D.N. Qu, X Yuan, and R.E. Burge. “Polarization dependence of the electromagnetic field distribution across wavelength-sized relief grating surfaces”. In: *JOSA A* 10.11 (1993), pp. 2317–2323. DOI: `10.1364/JOSAA.10.002317`.

[16] D Kolenov et al. “Direct detection of polystyrene equivalent nanoparticles with a diameter of 21 nm ($\lambda/19$) using coherent Fourier scatterometry”. In: *Optics Express* 29.11 (2021), pp. 16487–16505. DOI: `10.1364/OE.421145`.

[17] Gaoliang Dai et al. “Measurements of CD and sidewall profile of EUV photomask structures using CD-AFM and tilting-AFM”. In: *Measurement Science and Technology* 25.4 (2014), p. 044002. DOI: `10.1088/0957-0233/25/4/044002`.

[18] Gerald E Jellison Jr. “Data analysis for spectroscopic ellipsometry”. In: *Thin Solid Films* 234.1-2 (1993), pp. 416–422. DOI: `10.1016/0040-6090(93)90298-4`.

6

SHAPE CHARACTERIZATION OF SUBWAVELENGTH NANOSTRUCTURES

This chapter presents a coherent Fourier scatterometry (CFS)-based approach for determining the lateral shapes of subwavelength nanopillars with various geometries, including cylindrical, triangular, square, and rectangular cross-sections. By exploiting preferential excitation and rotational symmetry, distinct far-field scattering patterns are used to identify structural shapes beyond the diffraction limit. The method is validated through simulations and experiments, demonstrating robustness to fabrication imperfections and edge rounding. These results extend the applicability of CFS to shape metrology, offering new capabilities for advanced nanofabrication and device design.

Parts of this chapter have been published in Physical Review Applied **23**(2), 024016 [1].

The continuous scaling of semiconductor technology and the expanding application space of nanophotonics, sensing, and biotechnology have intensified the need for precise structural characterization of nanostructures. Among these, nanopillars, subwavelength structures with nanoscale dimensions, have emerged as key building blocks in photonic [2–4], electronic [5], sensing [6–8], energy [9, 10], and biomedical devices [11, 12]. Their optical, electronic, and mechanical properties, including band structure, carrier mobility, and light–matter interactions, strongly depend on their geometry—particularly diameter, height, and cross-sectional shape [13–15]. Control over shape is therefore crucial both for optimizing device performance and for understanding structure–function relationships at the nanoscale.

In previous chapters, we demonstrated how coherent Fourier scatterometry (CFS) can address diverse metrology challenges, from nanoscale defect detection and edge limitations to subsurface inspection and dimensional calibration. Building on this foundation, we now address a different challenge: determining the lateral shape of isolated nanostructures smaller than the illumination wavelength. Conventional methods such as SEM [16] and AFM [17] offer high-resolution imaging but are invasive, slow, and unsuitable for in-line use. SNOM [18] surpasses the diffraction limit but remains complex and difficult to interpret. Far-field techniques face fundamental resolution limits, and while scattering-based approaches such as CD-SAXS [19], MMIE [20], and MSM [21] provide structural insights, they require complex modeling and/or are often restricted to periodic structures. CFS, by contrast, is flexible, involves less complex modeling, and is applicable to both periodic and isolated structures. It has been used for grating parameter retrieval [22], detection of isolated nanoparticles [23], and defect localization [24].

Here, we extend CFS to retrieve nanopillar shape beyond the diffraction limit. By exploiting preferential excitation and rotational symmetry, we show that nanopillars with different cross-sections, cylindrical, triangular, square, or rectangular, produce distinctive far-field scattering signatures as they rotate. This enables shape discrimination even when their size is far less than the size of the focused illumination spot. The method is robust against edge rounding and fabrication imperfections, though currently limited to lateral shape characterization. Despite this, it provides a significant step toward non-invasive, high-throughput, and model-independent shape metrology with relevance to semiconductor manufacturing, photonics, and biosensing.

6.1. METHODS

6.1.1. CONCEPT

In this section, we introduce the scattering problem and the associated diffraction theory for CFS. In Fig. 6.1(left) the scattering problem is schematically illustrated, where a subwavelength scatterer present on top of a substrate is illuminated by a focused laser beam. We introduce a coordinate system (x, y, z) at the focal plane to define the geometry of the scattering system. The position of the subwavelength scatterer is defined as the origin of this coordinate system. According to the angular spectrum decomposition formalism, the focused beam can be decomposed into an infinite number of plane waves of different propagation directions [25]. Each such instance of plane waves $U_i(\theta_i, \phi_i)$ will be scattered (U_s) by the scatterer and collected by the microscope objective (O) having

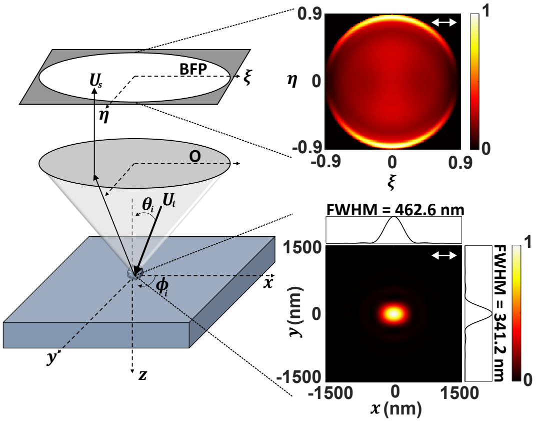

Figure 6.1: (left) Schematic representation of a subwavelength scatterer on a substrate illuminated by a focused laser beam. A plane wave (U_i) within the beam is scattered (U_S) and captured by a microscope objective (O) having numerical aperture (NA) and propagated to the back focal plane (BFP). (bottom right) Electric field intensity in the focal plane that interacts with the scatterer. Cross-sections reveal the FWHM, indicating field elongation along the polarization direction. (top right) Far-field image of a point scatterer illuminated by the focused field, consisting of two lobes, manifesting dipole radiation. Arrows (top right and bottom right) denote the polarization direction.

numerical aperture (NA), which will be further propagated to the back focal plane (BFP) (having a different coordinate system (ξ, η)) based on the Fourier optics theory [26]. The mapping of the scattered beams in the BFP is constrained by the NA of the objective.

A key aspect of our approach is the high NA (= 0.9) illumination, which creates a non-symmetric field in the focal region, as predicted by the vectorial diffraction theory [27, 28]. This field is elongated along the polarization direction of the incident light. In Fig. 6.1(bottom right) the elongated electric field intensity in the focal plane is shown. In the case of NA = 0.9, and wavelength $\lambda = 633$ nm, the electric field intensity along the polarization direction has FWHM = 462.2 nm, and for the electric field intensity orthogonal to the polarization direction, the FWHM = 341.2 nm. Let us consider a simple system where the nanostructure is a very small particle ($\ll \lambda$) and can be approximated to a single oscillating dipole. This approximation yields a characteristic far-field pattern with lobes oriented according to the polarization direction of the incident light (as shown in Fig. 6.1(top right)). This is due to the asymmetry in the focal field which induces a preferential excitation of the nanostructures along specific directions. Further, the scattering pattern deviates from this dipole-like behavior for larger or more complex nanostructures (here nanopillars of different shapes) where the single oscillating dipole approximation is not valid. This leads to additional features encoded in the far-field that provide more detailed information about the nanostructure. We aim to utilize this encoded information in the far-field signatures, where the asymmetry in the focal field induces a preferential excitation of the nanopillars along specific directions, combined with the intrinsic symmetry of the shape of the nanopillar. For this, we systematically rotate the nanopillars and analyze the resulting far-field patterns. By correlating these patterns with the nanostructure's orientation, we can infer the shape of the nanostructures.

6.1.2. EXPERIMENTAL SETUP

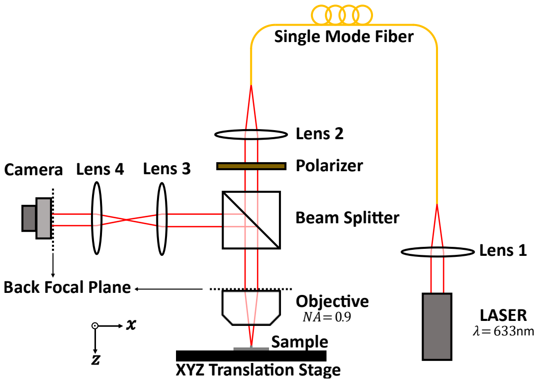

Figure 6.2: Schematic of the experimental setup of coherent Fourier scatterometry (CFS).

In this section, we outline the experimental setup for CFS used in this chapter, as depicted schematically in Fig. 6.2. A He-Ne laser operating at a wavelength of $\lambda = 633$ nm generates a collimated illumination beam, achieved through coupling with a single-mode fiber. Lens 1 couples the laser into the fiber, while lens 2 collimates the light emerging from it. A linear polarizer is used to control the polarization direction of the illumination beam. The polarizer can be rotated by an angle $\theta(= 0^\circ$ to $360^\circ)$, where the position $\theta = 0^\circ$ is defined as that where the polarization direction at the pupil is parallel to the x-axis. The linearly polarized collimated beam is directed through a non-polarizing beam splitter and then focused onto the nanopillars on the sample using a high numerical aperture (NA = 0.9) microscope objective. The sample is mounted on a piezo-controlled translation stage (XYZ-TS), to localize the nanopillars on the sample, allowing for precise observation. The scattered light is collected by the same microscope objective, passes back through the non-polarizing beam splitter, and is then relayed to the back focal plane of the microscope objective via a telescopic system composed of lens 3 and lens 4. A complementary metal-oxide-semiconductor (CMOS) camera positioned at this plane captures the angular spectrum of the scattered waves from all incident plane waves within the focused spot.

In the experiments, rather than rotating the nanopillars, which is practically complex, we manually rotate the linear polarizer and perform a single-shot measurement with the CMOS camera for each of the different polarization directions of the illumination beam, defined by θ. For each of these captured far-field images, we rotate these images back by an angle $-\theta$. This is done to imitate the situation where we rotate the nanopillars by θ. Further due to the reflection symmetry of the linear polarizer, the illumination beam for θ and $\theta + 180^\circ$ is identical. Hence we only perform single-shot measurement for the polarization directions of the illumination beam at θ with, $\theta = \Delta\theta \times n$, where $\Delta\theta = 30^\circ$ and $n \in [0,5] \cap \mathbb{Z}$.

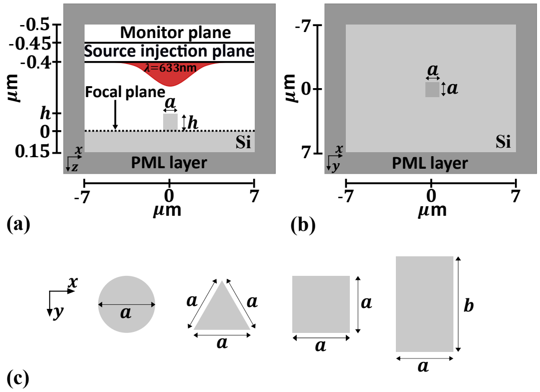

Figure 6.3: Illustration of the 3D-FDTD model, where a nanopillar (square nanopillar) is illuminated by a TM polarized focused beam of wavelength 633 nm (emanating from source injection plane). The scattered near-field is sampled at the monitor plane and propagated to the far-field through the FDTD simulation. (a) Corresponding y = 0 plane; (b) Corresponding z = 0 plane; (c) The orientation of the different nanopillars at z = 0 plane for $\theta = 0$.

6.1.3. NUMERICAL MODEL

The problem of the interaction between a tightly focused beam and nanopillars on a substrate is complex and demands careful consideration due to the intricate geometries and the presence of a substrate that disrupts the symmetry of the system [29]. Previous studies have primarily concentrated on the scattering of electromagnetic waves by spherical particles on flat surfaces, using various methods like Mie theory and the extensions of Weyl's method [30], and dipole approximations [31, 32] to simplify the problem. However, when dealing with more complex shapes, these simplified models and assumptions are insufficient. The substrate's impact on the scattering becomes more pronounced, especially when dealing with non-spherical geometries. Therefore, to accurately model the interaction of a focused beam with these nanopillar structures, we utilized rigorous 3D electromagnetic simulations, the finite difference time domain (3D-FDTD) method, implemented with the commercial software package Lumerical FDTD [33]. This approach solves Maxwell's equations in the time domain by discretizing space (Yee grids) and time.

In the simulations, we replicate the experimental conditions by modeling an isolated nanopillar (centered at the origin on the xy-plane) on top of a flat substrate, as the simulation object. The simulation domain is carefully sized to ensure that the width of the focused beam (FWHM ∼ 462 nm) is much smaller than the simulation domain's dimension (=14 μm). To prevent reflections, we apply perfectly matched layer (PML) boundary conditions on all boundaries. For the illumination, we utilize the vectorial diffraction theory of Richards and Wolf [27, 34], employing a TM polarized (i.e., the polarization direction at the pupil is parallel to the x-axis) plane wave of wavelength $\lambda = 633$ nm being focused by a microscope objective of numerical aperture 0.9 onto the focal plane (we choose our focal plane to be at the top of the substrate i.e., z = 0 plane). The scattered near field from the nanopillar is calculated and sampled at a monitor plane, thereafter propagating it into the far-field through the FDTD simulation [35].

In Fig. 6.3(a), the y = 0 plane, and in Fig. 6.3(b), the z = 0 plane of the complete 3D-

FDTD model is depicted. The geometrical parameters, lateral dimension (a), and height (h) characterize the simulation object's geometry (here the case of square nanopillar for illustration). The nanopillar's and the substrate's material is silicon (Si) with a refractive index of $n = 3.88126 + 0.01894i$. To investigate the influence of rotation of the nanopillar on the far-field signatures, we systematically rotate the simulation object by an angle $\theta (= 0°$ to $360°)$, while keeping the position of the source injection plane, monitor plane, and computational domain constant. The position of the different nanopillars at $\theta = 0°$ is shown in Fig. 6.3(c).

6.1.4. SAMPLE DESIGN AND FABRICATION

Table 6.1: Nominal geometrical parameters of the nanopillars.

Shape	**Diameter/ Length** a **(nm)**	**Breadth** b **(nm)**	**Height** h **(nm)**
Cylindrical nanopillar	100, 200, ..., 1000	-	250
Triangular nanopillar	100, 200, ..., 1000	-	250
Square nanopillar	100, 200, ..., 1000	-	250
Rectangular nanopillar	100, 200, ..., 1000	1000	250

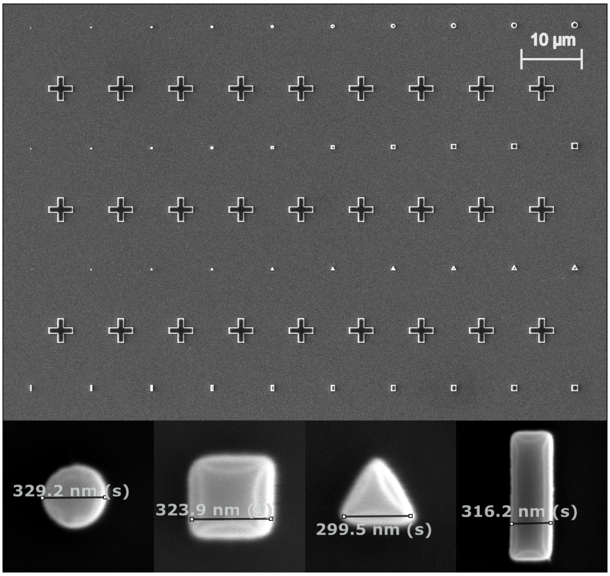

Figure 6.4: (top panel) SEM image of the fabricated nanopillars, described by geometrical parameters of Table 6.1. The + shaped markers are fabricated to facilitate the localization of the nanopillars on the sample. (bottom panel) Zoomed in SEM images of the different nanopillars.

A sample consisting of Si nanopillars of different shapes with nominal geometrical parameters as detailed in Table 6.1 is fabricated using e-beam lithography followed by etching. The Si wafer, after cleaning is spin-coated with the ARN7520 resist at 4000 rpm followed by a pre-exposure bake at 85°C for 60 seconds. The design is written on the resist with an exposure dose of 500 mJ/cm^2 using the Raith EBPG5200. After exposure and a post-exposure bake, the resist is developed in MF322 solution for 60 seconds followed by rinsing in water. The structures are then etched using reactive ion etching in Sentech Etchlab 200. The remaining resist is stripped by sonicating the sample in acetone for 5 minutes. In Fig. 6.4 (top panel), we show the SEM image of the fabricated nanopillars of the different shapes. The + shaped markers are fabricated to facilitate the localization of the nanopillars on the sample. In Fig. 6.4 (bottom panel), we show zoomed-in SEM images of the different nanopillars having nominal geometrical parameters: $a = 300$ nm, and $h = 250$ nm. The SEM measurements show that the lateral dimensions of the fabricated nanopillars are within 30 nm of the nominal values, however the tilted plane measurement of the nanopillars were not conclusive, and we cannot report the actual height of the fabricated nanopillars.

6.2. RESULTS

6.2.1. COMPARISON OF SIMULATIONS AND EXPERIMENTS

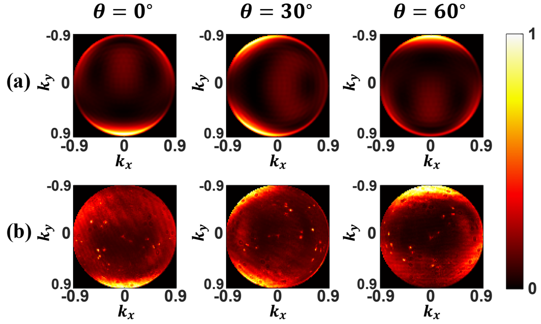

Figure 6.5: Far-field signatures corresponding to different rotations $\theta (= 0°, 30°, \text{ and } 60°)$ of the triangular nanopillar, defined by geometrical parameters: $a = 500$ nm and $h = 250$ nm. (a) Simulated using 3D-FDTD; (b) Experimental data.

In this section, we compare our simulated results with experimental data. Simulations allow us to explore the limitations of the methodology by varying parameters that cannot be easily adjustable in experiments, enabling us to better understand the underlying physics. Therefore, we need to establish that the simulation results are consistent with the experimental data. To illustrate this, let us consider a triangular nanopillar of geometrical parameters defined by length $a = 500$ nm and height $h = 250$ nm. In Fig. 6.5(a), we show the simulated far-field signatures corresponding to different orientations of the triangular nanopillar, defined by the rotation of the nanopillar ($\theta = 0°, 30°, \text{ and } 60°$). We observe a significant deviation of the far-field signatures from the symmetric dipole-like signature when a small spherical particle on a substrate interacts with a focused beam [23], and that the far-field signatures are different for the different θ, demonstrating that the far-field signatures are sensitive to the shape and orientation of the nanopillars even though the dimension of the nanopillars are smaller than the Airy diameter of the focused spot ($= 1.22\frac{\lambda}{NA}$ = 858 nm). In Fig. 6.5(b), we show the corresponding experimental far-field signatures, where instead of rotating the nanopillar sample we have rotated the polarization direction by θ and the far-field signatures have been rotated by $-\theta$. We observe that the simulated and experimental far-field signatures are consistent with each other demonstrating that our simulation model is faithful and that the combination of rotating the direction of polarization and the far-field signatures is equivalent to rotating the sample.

6.2.2. DETERMINATION OF SHAPES OF NANOPILLARS

In this section, we demonstrate that the shape of subwavelength nanopillars can be retrieved by utilizing the influence of geometrical shape and orientation of the nanopillars on the far-field signatures. We aim to understand how the different orientations i.e., the rotation of the nanopillars, will influence the far-field signatures and how they will differ for the different shapes. Now, to quantify these variations in the far-field signatures, we define a metric '$C_{A,B}$' which measures the correlation between the far-field signatures. With '$C_{A,B}$' mathematically expressed as:

$$C_{A,B} = \frac{\sum_{i=1}^{N}\sum_{j=1}^{N}\left(A_{ij}-\bar{A}\right)\left(B_{ij}-\bar{B}\right)}{\sqrt{\left(\sum_{i=1}^{N}\sum_{j=1}^{N}\left(A_{ij}-\bar{A}\right)^2\right)\left(\sum_{i=1}^{N}\sum_{j=1}^{N}\left(B_{ij}-\bar{B}\right)^2\right)}}, \tag{6.1}$$

where, A_{ij} and B_{ij} are the two far-field signatures at the $(i,j)^{th}$ pixel, with N^2 being the total number of pixels in the square far-field plane. $\bar{A}$ and $\bar{B}$ are the mean of all the N^2 pixels in the far-field plane of A and B, respectively.

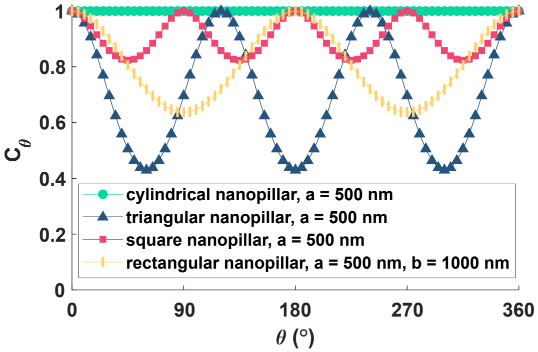

Figure 6.6: Simulated variation in far-field signatures as a function of θ for different nanopillar shapes, quantified by the correlation metric $C_\theta (= C_{0,0+\theta})$ as defined by Eq. 6.1. The results demonstrate a periodic variation in C_θ depending on the symmetry of the nanopillar shapes. The nanopillars are characterized by geometrical parameters: $a = 500$ nm, $b = 1000$ nm, and $h = 250$ nm.

For the analysis, we consider all the different shapes of nanopillars defined by geometrical parameters, $a = 500$ nm, $b = 1000$ nm, and $h = 250$ nm. We systematically rotate each nanopillar by an angle defined by $\theta (\theta = 0°$ to $360°)$ and for each type of nanopillar we calculate the correlation metric '$C_\theta (= C_{\theta_0,\theta_0+\theta})$'. With, $\theta_0 = 0°$, and $\theta = 0°$ to $360°$. However, θ_0 can be chosen to be any other arbitrary angle as well. In Fig. 6.6, we show the variation in the far-field signatures for the different shapes of nanopillars. The curves of different shapes have markers of the corresponding shapes. We observe that all the nanopillars of different shapes display different periodicity in the correlation metric. We observe that the periodicity of the correlation metric varies for the different shapes of the nanopillars i.e., 120° for triangular nanopillar, 90° for square nanopillar, and 180° for rectangular nanopillar. This periodicity depends on the rotational symmetry of the shape of the nanopillar. For cylindrical nanopillar, we do not observe any periodicity in the correlation metric as the cylindrical nanopillar is identical for any rotation θ. Therefore, based on C_θ we can determine the shape of the different nanopillars. Further, we observe that the peak-to-peak of C_θ, of the different shapes of nanopillars is not the same and indicates that the influence of rotation of the nanopillars on the variation in the far-field signatures is most sensitive for the triangular nanopillar, followed by rectangular nanopillar, with the square nanopillar showing the least sensitivity.

Now, we demonstrate experimentally that by utilizing CFS one can determine the shape of all different shapes of nanopillars. Here, we measure the far-field signatures of all the fabricated nanopillars described by the geometrical parameters as shown in Table 6.1. For each nanopillar, we systematically rotate the linear polarizer manually from $\theta = 0°$ to $150°$ with a separation of 30°, following the description in Section 6.1.2. From all the far-field signatures measured, we calculate the correlation metric '$C_\theta (= C_{\theta_0,\theta_0+\theta})$', where $\theta_0 = 0°, \theta = \Delta\theta \times n$, with $\Delta\theta = 30°$ and $n \in [0,12] \cap \mathbb{Z}$. In Fig. 6.7(a), we show the experimental variation of the correlation metric for cylindrical nanopillars. The correlation metric shows no periodicity for all the different dimensions a, indicating that these nanopillars are cylindrical. Further, we have $C_0 = C_{360} = 1$ as they are the same far-field signature and identical. However, for the other C_θ, it is not 1, this is because of experimental limitations, as it is not possible to guarantee that the nanopillar is at the exact center of the beam while we are taking the different measurements by rotating the linear polarizer manually. Further, there is the presence of multiple dirt particles in the microscope objective (can also be seen in the experimental far-field signatures of Fig. 6.5(b)) which appears in the far-field signatures, and as we rotate the far-field by an angle $-\theta$, these specks of dirt also rotate and reduce the correlation between them. Furthermore, as the fabrication process is not ideal, the presence of surface roughness and the fact that nanopillars are not exactly symmetric, also contributes to the reduction in correlation between them. In Fig. 6.7(b), we show the experimental variation of the correlation metric for triangular nanopillars. The correlation metric shows a clear periodicity of 120° for the different dimensions a. In Fig. 6.7(c), we show the experimental variation of the correlation metric for square nanopillars. The correlation metric shows a clear periodicity of 90° for the different dimensions a. In Fig. 6.7(d), we show the experimental variation of the correlation metric for rectangular nanopillars. The correlation metric shows a clear periodicity of 180° for the different dimensions a. Further, it is interesting to observe the variation in the correlation metric for the situation where the rectangle is converting to a square i.e., for $a = 800$ nm (rectangle), 900 nm (rectangle), and 1000 nm (square) (shown in the inset of Fig. 6.7(d)). For dimension, $a = 800$ nm (rectangle), the variation in correlation metric has a periodicity of 180°. For dimension $a = 900$

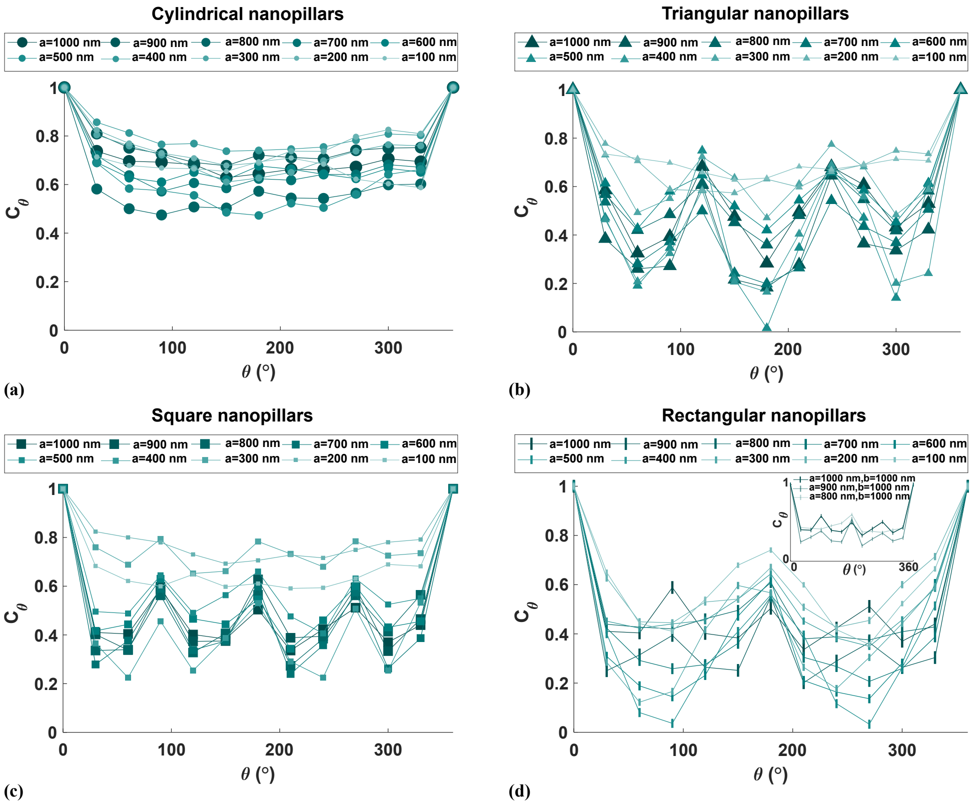

Figure 6.7: Experimental variation in far-field signatures as a function of θ for the different fabricated nanopillars, quantified by the correlation metric $C_\theta (= C_{0,0+\theta})$ as defined by Eq. 6.1. The nanopillars are characterized by geometrical parameters as given by Table 6.1. (a) For cylindrical nanopillars; (b) For triangular nanopillars; (c) For square nanopillars; (d) For rectangular nanopillars, with the inset showing the periodicity of the correlation metric C_θ changing from 180° for $a = 800$ nm (rectangle) to 90° for $a = 1000$ nm (square).

nm (rectangle), the variation in correlation metric has a periodicity of 180° but with small peaks appearing at $\theta = 90°$, and 270°. For dimension $a = 1000$ nm (square), the variation in correlation metric has a periodicity of 90°. These results imply that we can also distinguish the shape of the nanopillars which are almost square to square in shape. This experiment demonstrates that by utilizing CFS we can experimentally determine the shape of the different nanopillars (cylindrical, triangular, square, and rectangular) in a model-independent manner beyond the diffraction limit (diffraction limit = $\frac{\lambda}{2\mathrm{NA}} = 351$ nm).

6.2.3. LIMITATION OF SHAPE DETERMINATION

In this section, we analyze the limitations of our methodology for determining the shape of nanopillars. As our methodology is based on scattering from the nanopillars, the limiting factors include the lateral dimension of nanopillars (a), the height of nanopillars (h), and the quality of the fabrication of the nanopillars. Accordingly, we define a quantitative metric 'pk-to-pk C', which measures the maximum change in the correlation metric. The metric pk-to-pk C indicates the sensitivity of variation in the far-field signatures due to the rotation of the nanopillars. The metric pk-to-pk C can be mathematically expressed as:

$$\text{pk-to-pk } C = \max|\text{loc max}(C_\theta)| - \min|\text{loc min}(C_\theta)|, \tag{6.2}$$

where, $C_\theta (= C_{\theta_0,\theta_0+\theta})$ is the correlation metric as defined by Eq. 6.1, with $\theta_0 = 0°$, and $\theta \in (0°, 360°)$. With loc max$(C_\theta) = C_{\theta_{\text{max}}}$, $C_{\theta_{\text{max}}} \geq C_\theta$ for all $\theta \in (\theta_{\text{max}} - \delta, \theta_{\text{max}} + \delta)$, loc min$(C_\theta) = C_{\theta_{\text{min}}}$, $C_{\theta_{\text{min}}} \leq C_\theta$ for all $\theta \in (\theta_{\text{min}} - \delta, \theta_{\text{min}} + \delta)$, and $\delta (\delta > 0)$ considers the immediate neighborhood of $\theta_{\text{max}}, \theta_{\text{min}}$. We exclude C_0 and C_{360} to emphasize on the relative variations in C_θ for non-identical far-field signatures.

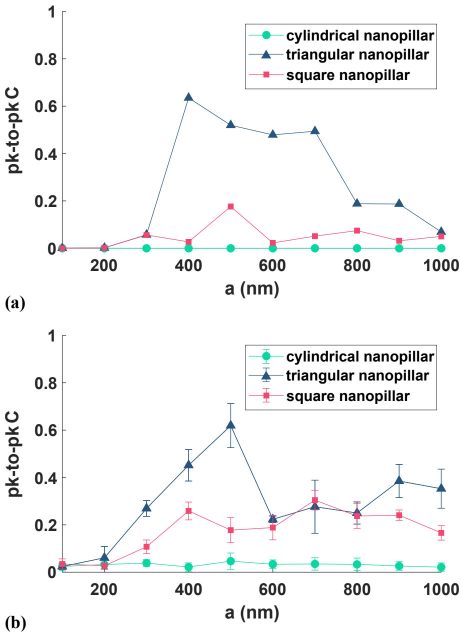

Figure 6.8: Limitation analysis of the lateral dimension (a) of the nanopillars (a) Simulated using 3D-FDTD; (b) Experimental data. Both indicating that the shape of the nanopillars can be determined for $a \geq 300$ nm.

Now, we analyze the limitation of the proposed CFS method for the determination of the shape of the nanopillars against the lateral dimension (a) of the nanopillars. Accordingly, we systematically vary the lateral dimension of the nanopillars $a = 100$ nm to 1000 nm, for the different shapes of nanopillars (cylindrical, triangular, and square) with $h = 250$ nm. We measure the correlation 'C_θ' and calculate the metric 'pk-to-pk C' using Eq. 6.2. In Fig. 6.8 we show how the pk-to-pk C depends on the lateral dimension (a) of the nanopillars for different shapes: Fig. 6.8(a) for the simulated results and Fig. 6.8(b) for the experimental results, respectively. We observe that for $a \leq 200$ nm, pk-to-pk $C \rightarrow 0$, i.e., we cannot distinguish between the different shapes of the nanopillars. This can also be observed in Fig. 6.7 (b) and (c), where for the triangular and square nanopillars with $a \leq 200$ nm, we do not observe any periodicity, and the variation in correlation metric is similar to that of cylindrical nanopillars. This indicates that after $a \leq 200$ nm, we approach the Sommerfeld-Rayleigh system ($a \ll \lambda$), where the nanopillar acts as an oscillating dipole with a defined orientation positioned near the substrate [36]. However for rectangular nanopillars even for $a \leq 200$ nm we always have $b = 1000$ nm which still influences the far-field signatures, preventing such a regime. Further, we observe that the trends for both the simulated and experimental results demonstrate reasonable agreement, where the metric pk-to-pk C is largest when $a \approx 500$ nm as here we have similar lateral dimensions of the nanopillars and the illuminating focused beam. The results demonstrate that the shape of the nanopillars can be determined for $a \geq 300$ nm.

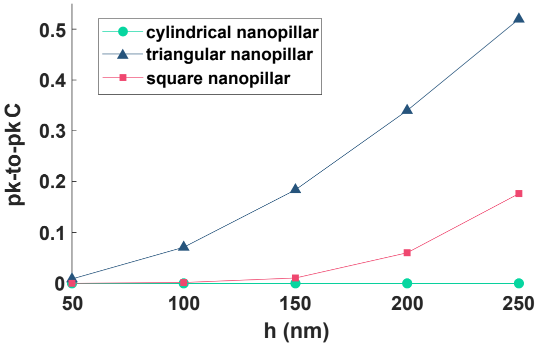

Figure 6.9: Limitation analysis of the height (h) of the nanopillars simulated using 3D-FDTD. Indicating that the shape of the square nanopillars can be determined for $h \geq 150$ nm and the shape of the triangular nanopillars can be determined for $h \geq 50$ nm.

Now, we analyze the limitation of the proposed CFS method for the determination of the shape of the nanopillars against the height of the nanopillars. Accordingly, we systematically vary the height of the nanopillars $h(= 50$ nm to 250 nm), for the different shapes of nanopillars (cylindrical, triangular, and square) with $a = 500$ nm. We numerically measure the correlation 'C_θ' and calculate the metric 'pk-to-pk C' using Eq. 6.2. In Fig. 6.9 we show how the pk-to-pk C depends on the height (h) of the nanopillars for different shapes. We observe that pk-to-pk C increases non-linearly with h, for triangular and square nanopillars. With the triangular nanopillars exhibiting a significantly stronger growth than square nanopillars. Further, we observe that pk-to-pk C is constant (= 0) for cylindrical nanopillars, as there is no variation in the correlation metric C_θ. We observe that the shape of the square nanopillars can be determined for $h \geq 150$ nm and the shape of the triangular nanopillars can be determined for $h \geq 50$ nm.

Now, we analyze the limitation of the proposed CFS method for the determination of the shape of the nanopillars against the distortion in the shape of the nanopillars, namely the edge roundness. Accordingly, we introduce edge roundness $r(= 0$ nm to 100) nm (shown schematically in Fig. 6.10 for a square nanopillar) to the different shapes of the nanopillars (triangular, square, and rectangular) with $a = 300$ nm, 500 nm, and 700 nm, and $h = 250$ nm. We numerically measure the correlation 'C_θ' and calculate the metric 'pk-to-pk C' using Eq. 6.2. In Fig. 6.10 we show how the pk-to-pk C varies with edge roundness (r) of the nanopillars for different shapes. We observe that for all the nanopillars of different shapes pk-to-pk C remains stable. Although we observe

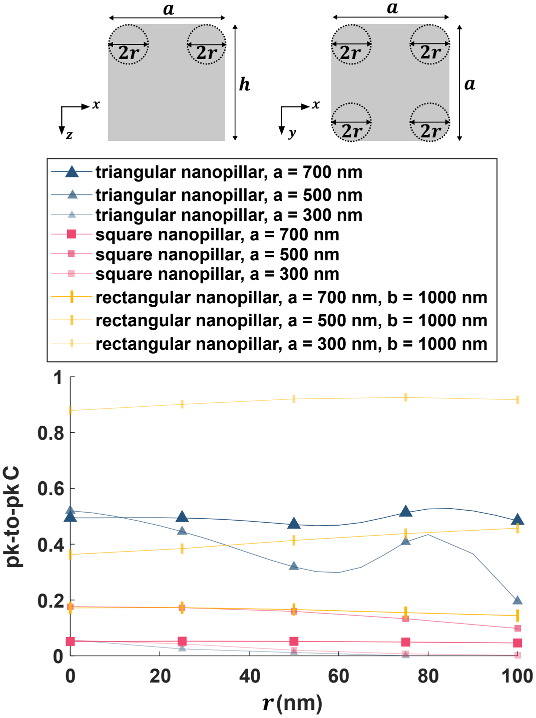

Figure 6.10: Limitation analysis of distortion of the shape of the nanopillars simulated using 3D-FDTD. Indicating the robustness of the methodology with the edge roundness (r) of the nanopillars.

some fluctuation for the triangular nanopillar with $a = 500$ nm, pk-to-pk C remains large. Further, only for the triangular and square nanopillars with $a = 300$ nm pk-to-pk C with large edge roundness goes to 0. This is understandable as at this edge roundness, these nanopillars are equivalent to cylindrical nanopillars. These results demonstrate the robustness of the methodology with the variation of edge roundness of the nanopillars.

6.3. SUMMARY

In this chapter, we demonstrated the use of coherent Fourier scatterometry (CFS) for determining the lateral shape of subwavelength nanopillars with cylindrical, triangular, square, and rectangular cross-sections. Our approach exploits preferential excitation of a focused beam and the inherent symmetry of the nanostructures to extract shape information from far-field scattering patterns as the sample is rotated. Simulations and experiments showed excellent agreement, and the method reliably distinguished nanopillar shapes with lateral dimensions $a \geq 300$ nm, surpassing the diffraction limit. Triangular nanopillars exhibited the strongest rotational sensitivity, while rectangular structures remained distinguishable even in regimes approaching the dipole limit. The technique was robust against edge rounding up to $r = 100$ nm and could also track transitions between rectangular and square shapes. Sensitivity to height was shape-dependent, with accurate characterization achieved for triangular pillars with $h \geq 50$ nm and square pillars with $h \geq 150$ nm. A key limitation is that the method is restricted to lateral shape determination and cannot resolve longitudinal features. Future work will focus on extending the approach to three-dimensional shape characterization. Overall, this work expands the capabilities of CFS beyond dimensional metrology to robust shape analysis, with direct implications for nanofabrication and device design.

BIBLIOGRAPHY

[1] Anubhav Paul et al. "Utilizing focused field as a probe for shape determination of subwavelength structures via coherent Fourier scatterometry". In: *Physical Review Applied* 23.2 (2025), p. 024016. DOI: `10.1103/PhysRevApplied.23.024016`.

[2] Wei-Yu Chiu et al. "A photonic crystal ring resonator formed by SOI nano-rods". In: *Optics Express* 15.23 (2007), pp. 15500–15506. DOI: `10.1364/OE.15.015500`.

[3] Haider Butt et al. "Photonic crystals & metamaterial filters based on 2D arrays of silicon nanopillars". In: *Progress In Electromagnetics Research* 113 (2011), pp. 179–194. DOI: `10.2528/PIER10122501`.

[4] Hyunsung Park and Kenneth B Crozier. "Multispectral imaging with vertical silicon nanowires". In: *Scientific Reports* 3.1 (2013), p. 2460. DOI: `10.1038/srep02460`.

[5] Charles M Lieber and Zhong Lin Wang. "Functional nanowires". In: *MRS Bulletin* 32.2 (2007), pp. 99–108. DOI: `10.1557/mrs2007.41`.

[6] Claire M Cobley et al. "Shape-controlled synthesis of silver nanoparticles for plasmonic and sensing applications". In: *Plasmonics* 4 (2009), pp. 171–179. DOI: `10.1007/s11468-009-9088-0`.

[7] M Khorasaninejad et al. "Color matrix refractive index sensors using coupled vertical silicon nanowire arrays". In: *Nano Letters* 12.8 (2012), pp. 4228–4234. DOI: `10.1021/nl301840y`.

[8] Chengkuo Lee et al. "Si nanophotonics based cantilever sensor". In: *Applied Physics Letters* 93.11 (2008), p. 113113. DOI: `10.1063/1.2987515`.

[9] Peidong Yang, Ruoxue Yan, and Melissa Fardy. "Semiconductor nanowire: what's next?" In: *Nano Letters* 10.5 (2010), pp. 1529–1536. DOI: `10.1021/nl100665r`.

[10] Rehan Kapadia et al. "Nanopillar photovoltaics: materials, processes, and devices". In: *Nano Energy* 1.1 (2012), pp. 132–144. DOI: `10.1016/j.nanoen.2011.11.002`.

[11] Michael Kandziolka et al. "Silicon nanopillars as a platform for enhanced fluorescence analysis". In: *Analytical Chemistry* 85.19 (2013), pp. 9031–9038. DOI: `10.1021/ac401500y`.

[12] B Ramana Murthy et al. "Silicon nanopillar substrates for enhancing signal intensity in DNA microarrays". In: *Biosensors and Bioelectronics* 24.4 (2008), pp. 723–728. DOI: `10.1016/j.bios.2008.06.044`.

[13] Alexandra C Ford et al. "Diameter-dependent electron mobility of InAs nanowires". In: *Nano Letters* 9.1 (2009), pp. 360–365. DOI: `10.1021/nl803154m`.

[14] D. D. D. Ma et al. "Small-diameter silicon nanowire surfaces". In: *Science* 299.5614 (2003), pp. 1874–1877. DOI: `10.1126/science.1080313`.

[15] Bozhi Tian et al. “Single-crystalline kinked semiconductor nanowire superstructures”. In: *Nature Nanotechnology* 4.12 (2009), pp. 824–829. DOI: `10.1038/nnano.2009.304`.

[16] Carl Georg Frase, Egbert Buhr, and Kai Dirscherl. “CD characterization of nanostructures in SEM metrology”. In: *Measurement Science and Technology* 18.2 (2007), p. 510. DOI: `10.1088/0957-0233/18/2/S26`.

[17] Danish Hussain et al. “Advances in the atomic force microscopy for critical dimension metrology”. In: *Measurement Science and Technology* 28.1 (2016), p. 012001. DOI: `10.1088/0957-0233/28/1/012001`.

[18] Paul Bazylewski, Sabastine Ezugwu, and Giovanni Fanchini. “A review of three-dimensional scanning near-field optical microscopy (3D-SNOM) and its applications in nanoscale light management”. In: *Applied Sciences* 7.10 (2017), p. 973. DOI: `10.3390/app7100973`.

[19] R Joseph Kline et al. “X-ray scattering critical dimensional metrology using a compact x-ray source for next generation semiconductor devices”. In: *Journal of Micro/Nanolithography, MEMS, and MOEMS* 16.1 (2017), pp. 014001–014001. DOI: `10.1117/1.JMM.16.1.014001`.

[20] Shiyuan Liu et al. “Mueller matrix imaging ellipsometry for nanostructure metrology”. In: *Optics Express* 23.13 (2015), pp. 17316–17329. DOI: `10.1364/OE.23.017316`.

[21] Cai Wang et al. “Reconstruction of finite deep sub-wavelength nanostructures by Mueller-matrix scattered-field microscopy”. In: *Optics Express* 29.20 (2021), pp. 32158–32168. DOI: `10.1364/OE.432611`.

[22] Nitish Kumar et al. “Reconstruction of sub-wavelength features and nano-positioning of gratings using coherent Fourier scatterometry”. In: *Optics Express* 22.20 (2014), pp. 24678–24688. DOI: `10.1364/OE.22.024678`.

[23] S. Roy et al. “Coherent Fourier scatterometry for detection of nanometer-sized particles on a planar substrate surface”. In: *Optics Express* 22.11 (2014), pp. 13250–13262. DOI: `10.1364/OE.22.013250`.

[24] Anubhav Paul et al. “Coherent Fourier scatterometry: a holistic tool for inspection of isolated particles or defects on gratings”. In: *Applied Optics* 62.29 (2023), pp. 7589–7595. DOI: `10.1364/AO.503350`.

[25] Jakob J Stamnes. *Waves in focal regions: propagation, diffraction and focusing of light, sound and water waves*. Routledge, 2017.

[26] Julius Adams Stratton. *Electromagnetic theory*. Vol. 33. John Wiley & Sons, 2007.

[27] Bernard Richards and Emil Wolf. “Electromagnetic diffraction in optical systems, II. Structure of the image field in an aplanatic system”. In: *Proceedings of the Royal Society of London. Series A. Mathematical and Physical Sciences* 253.1274 (1959), pp. 358–379. DOI: `10.1098/rspa.1959.0200`.

[28] Ralf Dorn, Susanne Quabis, and Gerd Leuchs. “The focus of light—linear polarization breaks the rotational symmetry of the focal spot”. In: *Journal of Modern Optics* 50.12 (2003), pp. 1917–1926. DOI: `10.1080/09500340308235246`.

[29] Alexei A Maradudin. *Light scattering and nanoscale surface roughness*. Springer Science & Business Media, 2010.

[30] PA Bobbert and J Vlieger. “Light scattering by a sphere on a substrate”. In: *Physica A: Statistical Mechanics and its Applications* 137.1-2 (1986), pp. 209–242. DOI: 10.1016/0378-4371(86)90072-5.

[31] Gorden W Videen, William L Wolfe, and William S Bickel. “Light scattering Mueller matrix for a surface contaminated by a single particle in the Rayleigh limit”. In: *Optical Engineering* 31.2 (1992), pp. 341–349. DOI: 10.1117/12.56076.

[32] Roland Schmehl, Brent M. Nebeker, and E. Dan Hirleman. “Discrete-dipole approximation for scattering by features on surfaces by means of a two-dimensional fast Fourier transform technique”. In: *JOSA A* 14.11 (1997), pp. 3026–3036. DOI: 10.1364/JOSAA.14.003026.

[33] Ansys *Lumerical FDTD solutions*. Available from https://www.lumerical.com/.

[34] Lukas Novotny and Bert Hecht. *Principles of nano-optics*. Cambridge university press, 2012.

[35] İlker R Çapoğlu et al. “The microscope in a computer: image synthesis from three-dimensional full-vector solutions of Maxwell’s equations at the nanometer scale”. In: *Progress in Optics* 57 (2012), pp. 1–91. DOI: 10.1016/B978-0-44-459422-8.00001-1.

[36] Gorden Videen et al. “Scattering from a small sphere near a surface”. In: *JOSA A* 10.1 (1993), pp. 118–126. DOI: 10.1364/JOSAA.10.000118.

7

DEEP LEARNING ENABLED ANISOTROPIC OPTICAL CHARACTERIZATION OF VAN DER WAALS MATERIALS

This chapter presents a deep learning–enabled coherent Fourier scatterometry (CFS) approach for retrieving the full anisotropic refractive index tensor (n_x, n_y, n_z) *of ultrathin materials. By exploiting angular scattering diversity and using radially polarized illumination, the proposed framework, AnisoVision, achieves single-shot, non-destructive optical characterization without prior knowledge of the crystal orientation of the monocrystalline sample. Validated on isotropic, uniaxial, and biaxial materials, the method demonstrates excellent accuracy and scalability. Its localized, high-throughput capabilities make it a powerful tool for anisotropy mapping, defect analysis, and optical metrology of 2D materials.*

Parts of this chapter have been accepted for publication in ACS Photonics **13**(1), 224 [1].

The characterization of anisotropic optical mono-crystalline materials, particularly ultrathin van der Waals crystals, is fundamental to the design and optimization of next-generation photonic and optoelectronic devices [2–7]. Accurate retrieval of refractive indices along different crystal axes enables the understanding of anisotropy-induced resonances, birefringence, and polarization-dependent phenomena, which are essential for tailoring the optical responses of materials such as hexagonal boron nitride (h-BN) and α-MoO_3 [8–10]. However, existing optical metrology techniques often fail to provide localized, non-invasive, and high-resolution measurements that are compatible with the nanoscale dimensions and strong anisotropy of these materials.

Spectroscopic ellipsometry remains a widely used tool for extracting optical constants of thin films [11, 12]. Yet, it requires multiple angles of incidence and polarization states, assumes lateral uniformity, and struggles with out-of-plane anisotropy unless operated at grazing incidence [13–15]. These limitations restrict its use for exfoliated or transferred 2D flakes, where lateral size, orientation, and thickness variation are common. As seen in previous chapters, coherent Fourier scatterometry (CFS) offers a promising alternative, enabling non-destructive, single-shot characterization by analyzing angular scattering/reflectance profiles from focused beams [16–18]. However, retrieving anisotropic dielectric tensor components from CFS data involves solving a high-dimensional inverse problem, which is computationally intensive and often ill-posed.

To overcome this challenge, recent advances in machine learning have introduced powerful tools for rapid inverse modeling in optical metrology [19–21]. Neural networks have been successfully applied to retrieve thickness [22], morphology [23], and optical properties [24–26]. Yet, most approaches remain limited to scalar optical constants or require large, noise-free datasets [27].

In this chapter, we present AnisoVision, a deep learning-enabled CFS framework for retrieving the full anisotropic refractive index tensor (n_x, n_y, n_z) of 2D materials. Our approach combines radially polarized illumination with selected angular cross-sections to decouple in-plane and out-of-plane optical responses. A dedicated neural network, IndexNet, trained on far-field profiles computed via the Berreman 4×4 matrix formalism, achieves rapid and accurate index retrieval across varying flake thicknesses. Validated on both isotropic and anisotropic materials, this technique represents a significant step forward in localized, inline anisotropic metrology, complementing the defect detection, subsurface probing, dimensional calibration, and shape analysis approaches developed in previous chapters.

7.1. METHODS

7.1.1. CONCEPT

In this section, we introduce the angle-resolved reflection problem from multilayered anisotropic flakes and the associated theoretical framework, as implemented through the CFS platform. Figure 7.1(a) illustrates the overall CFS configuration, where a tightly focused laser beam is incident on a multilayer structure consisting of air, an unknown anisotropic film denoted as $\mathrm{F}(n_x, n_y, n_z, h)$, and a semi-infinite silicon substrate. The system is described using a Cartesian coordinate system (x, y, z) with the z-axis normal to the surface and the origin located at the center of the illumination spot. According to the

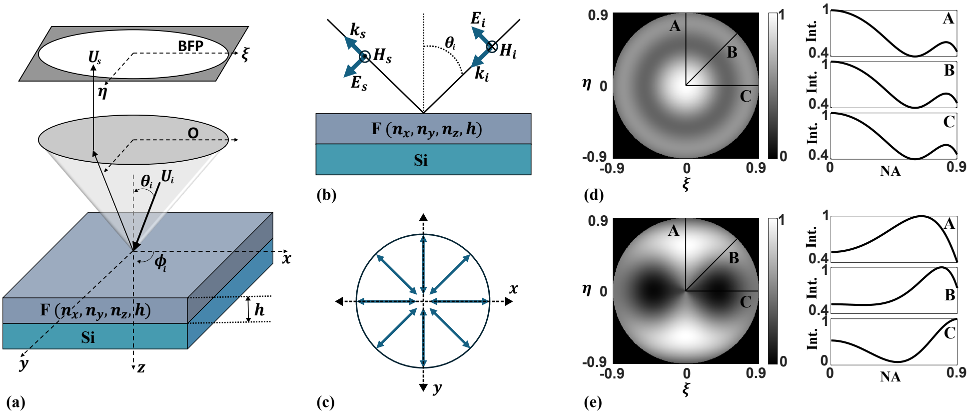

Figure 7.1: (a) Schematic of the CFS setup with focused field illumination and a multilayer stack comprising air, anisotropic film F(n_x, n_y, n_z, h), and silicon substrate. (b) Geometry of a single p-polarized plane wave interacting with the stack at an angle θ_i and azimuth ϕ_i. (c) Top-view of radial polarization showing uniform azimuthal angular coverage. (d) Simulated far-field for an isotropic film ($n_x = n_y = n_z = 1.46$). Cross-sections A, B, C correspond to azimuths $\phi = 0°$, $45°$, and $90°$, respectively. (e) Simulated far-field for an anisotropic film ($n_x = 2.7$, $n_y = 1.9$, $n_z = 2.1$), showing asymmetry in angular response.

angular spectrum decomposition formalism, the tightly focused beam is decomposed into a continuous distribution of plane waves $U_i(\theta_i, \phi_i)$, each characterized by a polar angle θ_i and an azimuthal angle ϕ_i, as shown in the conical illumination geometry. The angular range is determined by the numerical aperture (NA) of the objective lens (O). Upon interacting with the sample, each plane wave is partially reflected and transmitted, resulting in a net reflected field $U_s(\theta_i, \phi_i)$. These reflected fields are collected by the same objective and propagated to the back focal plane (BFP), where the angular distribution of the reflected light is recorded (coordinates (ξ, η)). This mapping between incident angles and spatial frequency at the BFP is governed by Fourier optics and is limited by the NA of the collection system [28].

To model the interaction of each plane wave with the stack (air, F, Si), we employ the 4×4 matrix formalism derived from Maxwell's equations [29]. This approach enables accurate modeling of stratified media with arbitrary anisotropy. The local geometry is shown in Fig. 7.1(b), where an individual p-polarized plane wave (i.e., with the electric field vector E_i lying in the plane of incidence) impinges on the multilayer structure. The film layer is characterized by a dielectric tensor $\bar{\varepsilon}$ with principal components ε_x, ε_y, and ε_z, which correspond to the square of the refractive indices ($\varepsilon_i = n_i^2$ for $i = x, y, z$). We assume the materials are linear, nonmagnetic ($\mu = \mu_0$), and homogeneous in each layer.

Each plane wave can be treated independently, and its interaction with the stack is modeled by solving Maxwell's equations in matrix form. The state of the electromagnetic field in the z-direction is represented by a four-component field vector: $\Psi(z) = [E_x(z), H_y(z), E_y(z), -H_x(z)]^T$, which satisfies the differential equation:

$$\frac{\partial}{\partial z}\Psi(z) = i\frac{\omega}{c}\Delta(z)\Psi(z), \tag{7.1}$$

where the 4×4 system matrix $\Delta(z)$ is constructed from the material tensors and the transverse wavevector $K_x = n_{\text{inc}} \sin\theta_i$. Assuming propagation in the x–z plane ($K_y = 0$), the matrix Δ takes the form [30] :

$$\Delta = \begin{bmatrix} -\frac{K_x \varepsilon_{zx}}{\varepsilon_{zz}} & 1 - \frac{K_x^2}{\varepsilon_{zz}} & -\frac{K_x \varepsilon_{zy}}{\varepsilon_{zz}} & \frac{K_x}{\varepsilon_{zz}} \\ \varepsilon_{xx} - \frac{\varepsilon_{xz}\varepsilon_{zx}}{\varepsilon_{zz}} & -\frac{K_x \varepsilon_{xz}}{\varepsilon_{zz}} & \varepsilon_{xy} - \frac{\varepsilon_{xz}\varepsilon_{zy}}{\varepsilon_{zz}} & \frac{\varepsilon_{xz}}{\varepsilon_{zz}} \\ 0 & 0 & 0 & 1 \\ \varepsilon_{yx} - \frac{\varepsilon_{yz}\varepsilon_{zx}}{\varepsilon_{zz}} & -\frac{K_x \varepsilon_{yz}}{\varepsilon_{zz}} & \varepsilon_{yy} - \frac{K_x^2 + \varepsilon_{yz}\varepsilon_{zy}}{\varepsilon_{zz}} & \frac{\varepsilon_{yz}}{\varepsilon_{zz}} \end{bmatrix}. \tag{7.2}$$

In the case of an isotropic, uniaxial, or biaxial material aligned with the coordinate axes, the off-diagonal components vanish, simplifying the matrix. The eigenmodes of the system, corresponding to forward and backward propagating (or evanescent) solutions, are obtained by diagonalizing Δ. The field evolution through each layer of thickness h is then expressed using:

$$\Psi(z+h) = R(h)\Psi(z), \quad R = P\exp(ik_0 hQ)P^{-1}, \tag{7.3}$$

where P contains the eigenvectors and Q is a diagonal matrix of eigenvalues (the z-components of the wavevectors). This formalism is implemented via the scattering matrix method as in the `ReticoloFilmStack` package to determine the reflected far-field pattern [31], which ensures stability even for highly anisotropic or thick layers.

A critical aspect of our approach is the use of radially polarized illumination (Fig. 7.1(c)), which provides a cylindrically symmetric, purely p-polarized angular spectrum. For illumination configuration, where the plane of incidence is aligned along the x-axis (i.e., $\phi = 0°$), the field satisfies $E_y = H_x = 0$, reducing the field vector to $\Psi(z) = [E_x(z), H_y(z), 0, 0]^T$. In this case, the optical response is independent of ε_y, making the response sensitive only to ε_x, ε_z, and h. Similarly, when the plane of incidence is along the y-axis ($\phi = 90°$), the response depends on ε_y, ε_z, and h. For intermediate orientations such as $\phi = 45°$, all three components ε_x, ε_y, and ε_z contribute. Figures 7.1(d) and (e) demonstrate this angular dependence using simulated far-fields for two representative cases. In Fig. 7.1(d), the film is isotropic ($n_x = n_y = n_z = 1.46$, $h = 600$ nm), producing a radially symmetric far-field pattern. In contrast, Fig. 7.1(e) shows the far-field for an anisotropic film with $n_x = 2.7$, $n_y = 1.9$, $n_z = 2.1$, and $h = 600$ nm. The asymmetry is evident, particularly in the angular slices labeled A, B, and C, which correspond to $\phi = 0°$, 45°, and 90°, respectively. The azimuthal variation encodes the anisotropy of the film. This property allows us to drastically reduce the dimensionality of both simulation and experiment. Instead of analyzing the full 2D far-field, we extract only three azimuthal cross-sections (at 0°, 45°, and 90°), which are sufficient to uniquely retrieve n_x, n_y, and n_z for a known h. Because the radially polarized illumination always contains all azimuths (Fig. 7.1(c)), these slices are inherently present in every measurement, eliminating the need for sample alignment or scanning.

In summary, we utilize the 4×4 matrix formalism to rigorously model the reflectance of each angular plane wave in the focused beam. The combination of radially polarized illumination and selective azimuthal sampling enables efficient and robust reconstruction of anisotropic optical properties, using a minimal subset of far-field data. This approach is broadly applicable to layered anisotropic materials, including but not limited to van der Waals materials.

7.1.2. EXPERIMENTAL SETUP

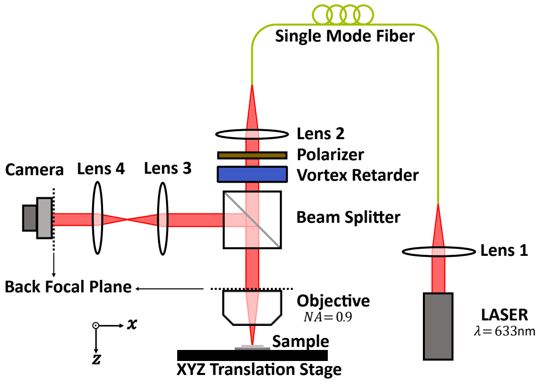

Figure 7.2: Schematic of the experimental setup of coherent Fourier scatterometry (CFS).

Here, the experimental configuration of the CFS setup, schematically illustrated in Fig. 7.2, is employed to perform the measurements in this chapter. A linearly polarized He-Ne laser operating at a wavelength of $\lambda = 633$ nm serves as the illumination source. The laser beam is first coupled into a single-mode optical fiber using Lens 1 to ensure a clean Gaussian mode profile. Light emerging from the fiber is collimated using Lens 2 to produce a spatially uniform, coherent, and collimated beam. To generate spatially varying polarization states, we employ a combination of a linear polarizer and a liquid crystal polymer (LCP) vortex half-wave retarder of topological charge $m = 1$. By aligning the fast axis of the vortex retarder either parallel or perpendicular to the input linear polarization, one can produce radially or azimuthally polarized beams, respectively. In this work, we exclusively use the radially polarized configuration, which ensures that all incident plane waves in the focused beam are p-polarized with respect to their local planes of incidence. The collimated, radially polarized beam is directed toward a nonpolarizing beam splitter, which transmits the beam to a high numerical aperture (NA = 0.9) microscope objective; with the beam diameter being significantly larger than the objective aperture, ensuring uniform, flat-field illumination across the entrance pupil (the calibration of the microscope objective is provided in Appendix B). This objective focuses the beam onto the sample surface, resulting in a tightly confined focal spot (nominal FWHM ≈ 491.39 nm). The sample, composed of a multilayer stack (air, anisotropic film $\mathrm{F}(n_x, n_y, n_z, h)$, and silicon substrate), is mounted on a piezocontrolled XYZ translation stage, allowing for precise sample positioning. In this study, we investigate four types of samples: Si_3N_4 (SiN) on Si, SiO_2 on Si, hexagonal-BN (h-BN) on Si, and α-MoO_3 on Si. The backreflected light from the sample is collected by the same microscope objective and passes back through the beam splitter. A relay telescope, composed of Lens 3 and Lens 4, projects the back focal plane (BFP) of the objective onto a complementary metal-oxide-semiconductor (CMOS) camera. As each incident plane wave contributes to a specific direction in the BFP, the recorded image represents the far-field reflectance distribution resulting from the entire angular spectrum present in the focused beam.

An important consideration in this setup arises from the phase singularity introduced by the vortex retarder. At the beam center, where the azimuthal phase wraps by 2π, a phase singularity forms, leading to a central null-intensity in the illumination profile [32]. This singularity is transferred to the BFP of the objective and appears as a region of undefined phase and suppressed intensity at the center of the far-field image. As this central region contains distorted or ambiguous information, we exclude it from all data analysis and from the retrieval algorithm. This masking step is critical for ensuring accurate reconstruction of the anisotropic optical constants.

7.1.3. DEEP LEARNING ARCHITECTURE

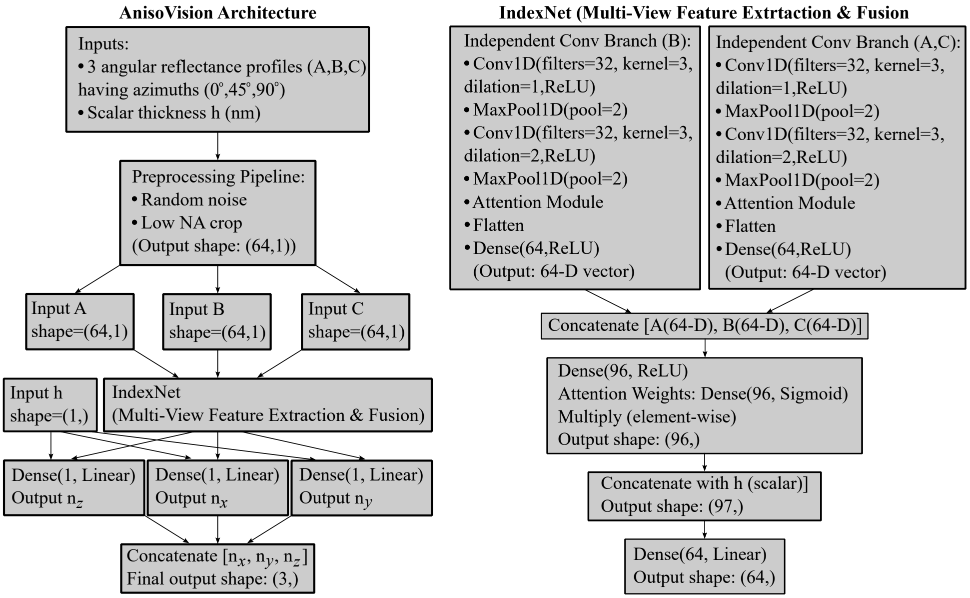

Figure 7.3: Schematic of the deep learning framework. The AnisoVision model accepts three far-field signals (A, B, C) and one scalar thickness value h. Signals A and C are processed through a shared IndexNet block comprising Conv1D, pooling, dilation, and attention layers. Signal B is processed in a similar, separate path. Extracted features are fused and passed through a global attention layer. After concatenation with h, the network predicts n_x, n_y, and n_z.

To retrieve the anisotropic refractive indices n_x, n_y, n_z of thin films from angle-resolved reflectance data, we developed a deep learning framework termed AnisoVision, illustrated schematically in Fig. 7.3. This framework is designed to process multi-view, polarization-resolved far-field signals and output accurate predictions of material parameters from minimal data. The AnisoVision model uses a custom-built architectural module called IndexNet, which performs joint feature extraction and fusion from multiple 1D signal channels.

The AnisoVision model accepts four inputs: three angular reflectance profiles (signals A, B, and C), each corresponding to a fixed azimuthal slice (0°, 45°, and 90°), and a scalar value representing the film thickness h. The network architecture comprises a shared convolutional feature extractor, attention-based weighting modules, and a fully connected regression head.

The feature extraction pipeline for signals A and C is identical and performed by the shared IndexNet module. This module includes a sequence of 1D convolutional layers followed by max pooling to extract local features and reduce dimensionality. A dilated convolutional layer is applied next to capture long-range dependencies and broader contextual information. The resulting feature maps are passed through a channel-wise attention mechanism that learns to amplify or suppress specific features, selectively enhancing those most relevant to the prediction task. This process yields a compact 64-dimensional representation for each input signal. Signal B is processed using a similar but independent feature extraction path.

The resulting feature vectors from all three signal branches are concatenated and passed through a global attention block, which enables the model to prioritize information across the different inputs. The scalar thickness value h is then concatenated to this combined feature representation to condition the network's prediction on film thickness. The final layers consist of a series of fully connected layers that map the fused features to three outputs: the refractive indices n_x, n_y, and n_z.

The model comprises approximately 186,000 trainable parameters and is optimized using the Adam optimizer with a mean squared error loss function. For training, we generated a synthetic dataset of 26 million samples using the `ReticoloFilmStack` package. Each sample corresponds to a unique combination of refractive indices within the range $n_i \in [1.3, 4.0]$ and thickness values $h \in [200, 800]$ nm. In all generated datasets, the substrate was assumed to be Si, consistent with the experimental samples studied. For measurements involving different substrate materials, new datasets must be generated to account for the modified optical response; however, the network architecture of the model remains unchanged. To align the training data with realistic experimental conditions, the preprocessing pipeline introduces additive Gaussian noise ($\sigma \in [0.001, 0.01]$), normalizes cross-sections to (0,1), crops the central angular region affected by the vortex singularity, and resizes to reduce sensitivity to local defects. These steps ensure that the network learns robust features representative of practical reflectance profiles, enabling generalization to experimental data. The idea of improving robustness via input perturbations is conceptually supported by stability training in deep neural networks [33]. By training the model only on three azimuthal slices instead of the full 2D far-field, we significantly reduce the dimensionality and computational load while preserving directional sensitivity necessary to infer anisotropy at the cost of some reduction in the overall SNR by using only a (very) limited subset of the data.

7.1.4. SAMPLE PREPARATION

SiN / SiO$_2$ on Si: The samples consist of thin layer of either SiN or SiO$_2$ on a Si substrate. The samples are fabricated on a standard 525 μm thick Si wafer. The wafer is first cleaved into 15 × 15 mm samples, and cleaned in acetone and isopropanol (IPA) using an ultrasonic bath. Subsequently, we deposited a 337.3 nm silicon nitride and a 608.1 nm silicon dioxide layer, respectively, on the substrates via inductively coupled plasma chemical vapor deposition (ICPCVD, Oxford PlasmaPro100). ICPCVD is known for enhanced deposition uniformity and minimized edge effects, which are beneficial for accurate refractive index determination. The depositions are carried out at a table temperature of 150 °C and a chamber pressure of 8 mTorr.

h-BN on Si: The sample consists of flakes of h-BN flakes on a Si substrate. The Si substrate was first acid cleaned, followed by organic cleaning with acetone, IPA and DI water in an ultrasonic bath. The h-BN flake was fabricated by mechanically exfoliating commercially available bulk h-BN (HQ Graphene) using the scotch tape method. The flakes were thinned down by a few exfoliations on the tape itself and then exfoliated on the Si substrate.

α-MoO$_3$ on Si: The sample consists of flakes of α-MoO$_3$ flakes on a Si substrate. Bulk α-MoO$_3$ crystals were acquired from 2D Semiconductors. The flakes were mechanically exfoliated from the bulk crystals and transferred onto the Si substrates (350 μm in thickness) using a polydimethylsiloxane (PDMS)-based exfoliation and transfer method (X0 retention, DGL type, Gelpak) at 90°C.

7.2. RESULTS AND DISCUSSION

7.2.1. ANISOVISION MODEL PERFORMANCE

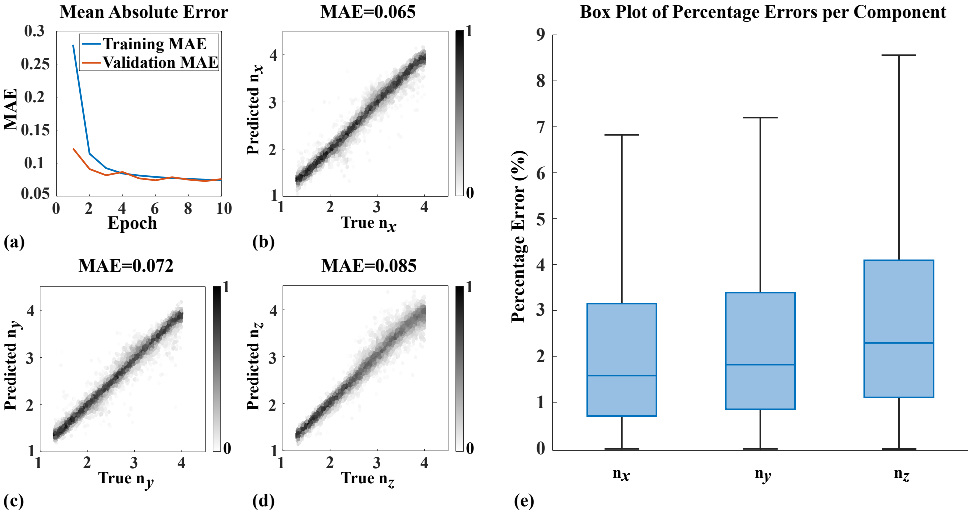

Figure 7.4: Performance evaluation of the AnisoVision model. (a) MAE vs. epoch for training and validation sets. (b–d) Scatter density plots comparing predicted and true values for n_x, n_y, and n_z over 10,000 random test samples; corresponding MAEs are also indicated. (e) Box plot of percentage errors for each refractive index component showing the statistical spread and median error.

To evaluate the predictive accuracy and generalization capability of the AnisoVision model, we conducted both training-validation tracking and targeted performance testing on a held-out test set. The model was trained for 10 epochs using the synthetic dataset described previously, with the learning progress monitored via the mean absolute error (MAE) metric on both training and validation sets. As shown in Fig. 7.4(a), the model exhibits stable convergence behavior, reaching a final validation MAE of 0.0758 after 10 epochs.

While the training dataset was constructed from uniformly sampled combinations of film thickness $h \in [200, 800]$ nm (sampled in 10 nm steps) and refractive indices $n_i \in [1.3, 4.0]$ (sampled in steps of 0.02), we further evaluated the model's ability to interpolate and generalize to unseen combinations within these ranges. To this end, we generated a test set consisting of 10,000 random configurations, sampled across the same parameter space. The model's predictions on this randomized test set are shown in Fig. 7.4(b–d), where true versus predicted values for n_x, n_y, and n_z are plotted, demonstrating the prediction density. The model demonstrates excellent agreement between true and predicted values across the entire refractive index range, with component-wise MAEs of 0.065 for n_x, 0.072 for n_y, and 0.085 for n_z. It should be noted that the 10,000 test samples do not represent repeated measurements of a single configuration, but rather 10,000 distinct unseen parameter combinations used to assess model generalization. Therefore, the reported prediction errors should be interpreted as generalization errors over the sampled parameter space, rather than as statistical uncertainties scaling with $1/\sqrt{N}$. Among the three components, the model shows slightly higher error for n_z. This reduced accuracy can be attributed to the inherently lower sensitivity of the far-field signal to the out-of-plane permittivity ε_z, particularly for thinner layers. The influence of n_z on the angular reflectance is comparatively weaker and highly dependent on the layer thickness h, making its contribution more difficult to resolve.

To obtain a more statistically robust assessment of prediction error, we also computed the percentage error for each component across the 10,000 test samples and summarized the distributions as box plots in Fig. 7.4(e). The median percentage error for in-plane indices n_x and n_y was 1.582% and 1.820%, respectively, while for n_z it was 2.292%. These low percentage errors indicate that the model captures the underlying physics and anisotropic trends of the reflectivity process with high fidelity, even in unseen regions of the parameter space. Moreover, we observe that the MAE is worse at higher refractive indices (as can be seen in Fig. 7.4(d)); however, such high refractive index values are uncommon outside narrow resonance bands [34]. Therefore, for most real materials with moderate and smoothly varying indices, where the model performs with significantly lower error, the method is expected to perform even better than what is indicated in Fig. 7.4(e). More details on the performance of the AnisoVision model are provided in Appendix C.

7.2.2. OPTICAL CHARACTERIZATION OF ISOTROPIC MATERIALS

To experimentally validate the accuracy and robustness of the proposed approach, we applied the AnisoVision model to characterize two well-known isotropic dielectric films: silicon nitride (SiN) and silicon dioxide (SiO_2). These materials serve as important reference samples to confirm that the framework can reliably extract refractive index values when the sample exhibits no in-plane and out-of-plane anisotropy, i.e., $n_x = n_y = n_z$.

Figure 7.5(a) shows the measured far-field reflectance pattern for the SiN sample (air/SiN/Si), captured at the back focal plane with the central region cropped due to the vortex-induced singularity. The three cross-sectional slices: A ($\phi = 0°$), B ($\phi = 45°$), and C ($\phi = 90°$) are also shown as normalized intensity profiles. As expected for an isotropic film, the angular reflectance pattern is radially symmetric, and thus the intensity variations along different azimuthal directions are nearly identical. This radial symmetry enables profile averaging, which improves the signal-to-noise ratio and reduces the impact of scattering artifacts caused by surface dust or imperfections across the objective's aperture.

The corresponding cross-sectional SEM image of the SiN sample is shown in Fig. 7.5(b). The SiN layer thickness is measured to be $h = 337.3$ nm. Using this thickness as input to the AnisoVision model, we retrieved the refractive indices as $n_x = n_y = n_z = 2.057$, which is in good agreement with the literature values for SiN at the wavelength of 633 nm [35].

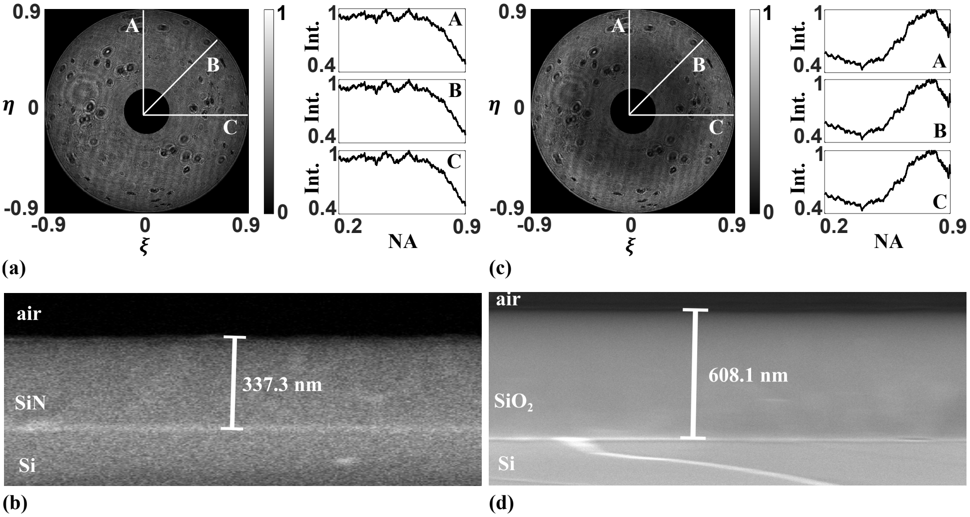

Figure 7.5: Experimental validation of the AnisoVision framework on isotropic films. (a) Measured far-field and normalized cross-sections (A, B, C) for SiN on Si; (b) cross-sectional SEM image showing SiN thickness of 337.3 nm. (c) Measured far-field and normalized cross-sections (A, B, C) for SiO_2 on Si; (d) SEM image showing SiO_2 thickness of 608.1 nm.

Similarly, Fig. 7.5(c) shows the measured far-field pattern for the SiO_2 sample (air/SiO_2/Si), again exhibiting radial symmetry across the three angular slices. The corresponding SEM image in Fig. 7.5(d) reveals a film thickness of $h = 608.1$ nm. Using this value in AnisoVision yields the retrieved refractive indices $n_x = n_y = n_z = 1.469$, which also agrees well with standard reported values for SiO_2 at this wavelength [36, 37].

These two examples demonstrate that the proposed deep-learning-based CFS framework is capable of accurately retrieving isotropic refractive index values from experimental far-field data. The radial polarization illumination, combined with the model's ability to focus on key angular features, ensures robustness to noise and spatial inhomogeneities in the optical system.

7.2.3. Optical Characterization of Van der Waals Materials

To demonstrate the generalizability of our technique beyond conventional isotropic materials, we apply it to characterize thin exfoliated flakes of van der Waals (vdW) materials. In this section, we present results on two representative materials: hexagonal-BN (h-BN) and α-MoO_3, which exhibit uniaxial and biaxial optical anisotropy, respectively. These materials are widely studied in nanophotonics for their unique optical responses and anisotropic dielectric properties [38, 39]. h-BN is a wide-bandgap (~6 eV) layered material composed of alternating boron and nitrogen atoms in a hexagonal lattice. It is optically transparent

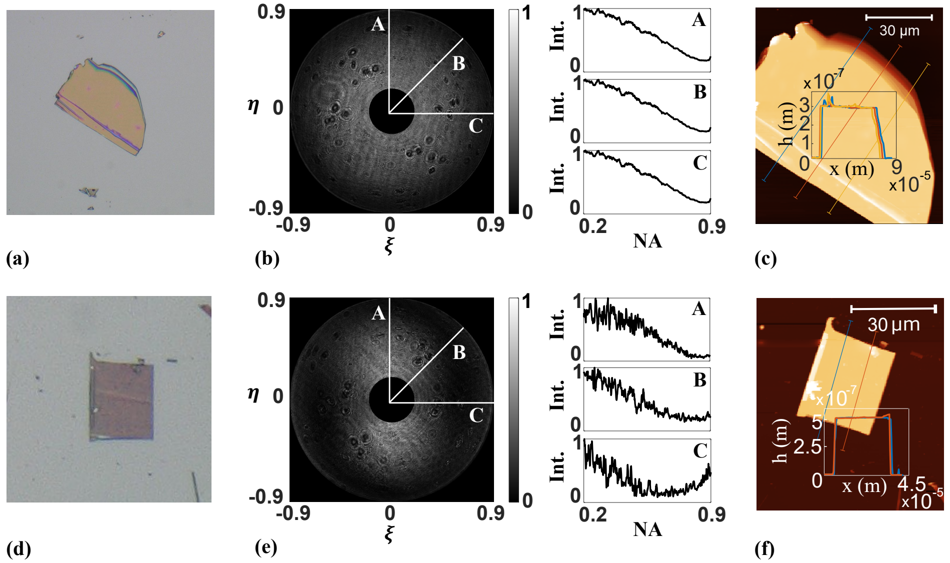

Figure 7.6: Optical characterization of anisotropic van der Waals materials using AnisoVision. (a) Optical microscope image of an exfoliated h-BN flake. (b) Measured far-field intensity profile (central region cropped) and normalized cross-sectional slices A (0°), B (45°), and C (90°) for h-BN, showing radial symmetry due to uniaxial anisotropy. (c) Atomic force microscopy (AFM) image of the h-BN flake, indicating a thickness of 300 nm. (d) Optical microscope image of an exfoliated α-MoO$_3$ flake. (e) Orientation-corrected far-field intensity profile and corresponding cross-sections A, B, and C, revealing asymmetry due to biaxial anisotropy. (f) AFM image of the α-MoO$_3$ flake, indicating a thickness of 510 nm.

across a broad spectral range and exhibits pronounced uniaxial anisotropy due to its anisotropic crystal structure. The in-plane refractive index ($n_x = n_y$) and out-of-plane index (n_z) differ significantly, with reported anisotropy $\Delta n \approx 0.3$–0.7 in the visible range [8, 40]. These properties make h-BN an ideal platform for nanoscale optical confinement, quantum emitters, and hyperbolic dispersion. α-MoO$_3$ is a strongly birefringent vdW crystal that exhibits a monoclinic lattice structure, resulting in three distinct principal refractive indices ($n_x \neq n_y \neq n_z$). This biaxial character leads to asymmetric light-matter interactions, enabling applications in mid-infrared photonics, in-plane hyperbolicity, and directionally dependent excitonic responses [3, 4, 6, 10]. Mechanical exfoliation of α-MoO$_3$ yields optically flat flakes suitable for far-field optical studies. Due to the nature of mechanical exfoliation, the flakes used in this study exhibit variation in lateral dimensions, thickness, and in-plane crystal orientation. To correct for rotational misalignment of the far-field patterns, we apply a symmetry-based algorithm (see Appendix D) to infer the principal crystal axes and align the far-field data accordingly.

Figure 7.6(a) shows the optical microscope image of the h-BN flake characterized in this study. The corresponding measured far-field pattern (after cropping the central vortex region) is shown in Fig. 7.6(b), along with the normalized cross-sectional profiles A, B, and C at azimuthal angles 0°, 45°, and 90°, respectively. As expected for a uniaxial crystal with no in-plane anisotropy, the far-field exhibits radial symmetry, allowing us to average the profiles across all azimuthal directions to suppress experimental noise. The height of the flake was measured using atomic force microscopy (AFM), as shown in Fig. 7.6(c), yielding a thickness of $h = 300$ nm (details of the AFM measurements is provided in Appendix E). Using this value as input to the AnisoVision model, we retrieve the refractive indices $n_x = n_y = 2.109$ and $n_z = 1.485$, which correspond to an out-of-plane anisotropy $\Delta n_{xz} = \Delta n_{yz} = 0.624$. These results are in agreement with previously reported values at 633 nm, including $n_x = n_y = 2.126$ and $n_z = 1.567$ from Zotev *et al.* [2], $n_x = n_y = 2.215$ and $n_z = 1.601$ from Grudinin *et al.* [8], and $n_x = n_y = 2.137$ and $n_z = 1.851$ from Rah *et al.* [41].

Figure 7.6(d) shows the optical microscope image of an exfoliated α-MoO$_3$ flake. The far-field, corrected for orientation, is shown in Fig. 7.6(e), along with the extracted normalized cross-sectional profiles A, B, and C. Unlike h-BN, the far-field distribution of α-MoO$_3$ is clearly anisotropic, confirming the presence of strong in-plane anisotropy. To reduce noise while preserving directional information, we average the profiles only over azimuthally equivalent directions: A over 0° and 180°, B over 45°, 135°, 225°, and 315°, and C over 90° and 270°. The flake height was measured via AFM (Fig. 7.6(f)) to be $h = 510$ nm. Using AnisoVision, we retrieve $n_x = 2.297$, $n_y = 2.229$, and $n_z = 1.926$, leading to in-plane anisotropic value of $\Delta n_{xy} = 0.068$, and out-of-plane anisotropic values of $\Delta n_{xz} = 0.371$, and $\Delta n_{yz} = 0.303$. These results are in agreement with previously reported anisotropic indices at 633 nm, $n_x = 2.230$, $n_y = 2.220$, and $n_z = 1.969$ by Andres-Penares *et al.* [42].

These experiments validate the ability of our framework to accurately extract full dielectric tensor components from far-field intensity profiles of anisotropic 2D materials, without requiring prior knowledge of the crystal orientation or using polarization-resolved detection.

7.2.4. ANISOVISION MODEL STABILITY WITH VARYING HEIGHT

To further validate the robustness of AnisoVision, we assess its stability in retrieving consistent optical properties across samples of the same material but with varying thicknesses. While the height of an anisotropic film significantly influences the resulting far-field patterns, the underlying refractive indices of the material remain constant. Therefore, an accurate and reliable model should consistently recover the same n_x, n_y, n_z values irrespective of layer thickness.

To test this, we study twelve different mechanically exfoliated flakes of α-MoO$_3$, each with a distinct thickness due to the random nature of exfoliation. These flakes exhibit various lateral dimensions and thicknesses ranging from approximately 380 to 720 nm. The far-field angular distributions of all twelve samples are shown in Fig. 7.7. For each flake (indexed 1 through 12), we show (i) the normalized, cropped, and rotation-corrected far-field image at the top, and (ii) the corresponding AFM height line profile at the bottom. With the red star shaped markers representing the approximate location of the measurements. The corresponding flake thicknesses were precisely determined using AFM, and the measured heights were used as inputs to AnisoVision for retrieval. In Table 7.1, we summarize the retrieved values of n_x, n_y, and n_z along with the corresponding heights h for each of the twelve flakes. In Fig. 7.8, we present the predicted values of n_x, n_y, and n_z as a function of layer thickness h. Despite significant variation in height across the samples, the retrieved refractive indices remain consistent. Specifically, the mean retrieved values are $n_x = 2.291$, $n_y = 2.207$, and $n_z = 1.947$, with standard deviations

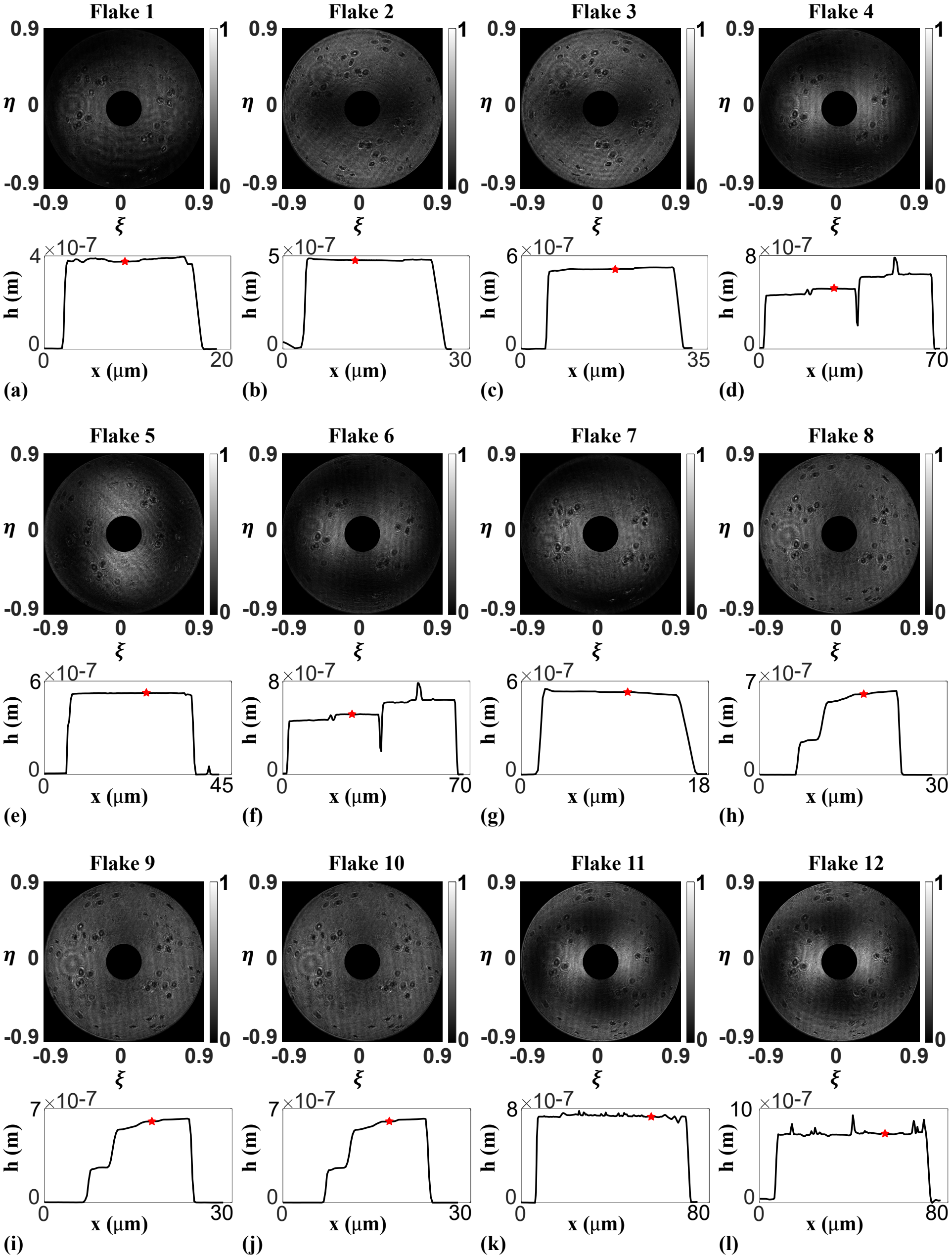

Figure 7.7: (a)–(l) Normalized, cropped, and rotation-corrected far-field images (top) and atomic force microscopy (AFM) height line profiles (bottom) for twelve distinct α-MoO$_3$ flakes (Flakes 1–12). Red stars denote the approximate location of the measurements.

Table 7.1: Retrieved refractive indices n_x, n_y, and n_z for twelve exfoliated α-MoO$_3$ flakes of varying thicknesses.

Flake	h **(nm)**	n_x	n_y	n_z
1	383	2.3472	2.2882	1.9197
2	475	2.3894	2.2338	2.0720
3	495	2.2340	2.0806	1.8520
4	503	2.2728	2.2317	2.0087
5	510	2.2975	2.2299	1.9264
6	511	2.2496	2.2308	1.9283
7	538	2.2466	2.1534	1.9371
8	608	2.2703	2.2078	1.9282
9	608	2.2709	2.1727	1.9385
10	608	2.2357	2.1678	1.9237
11	721	2.2961	2.2546	2.0103
12	735	2.3776	2.2283	1.9229

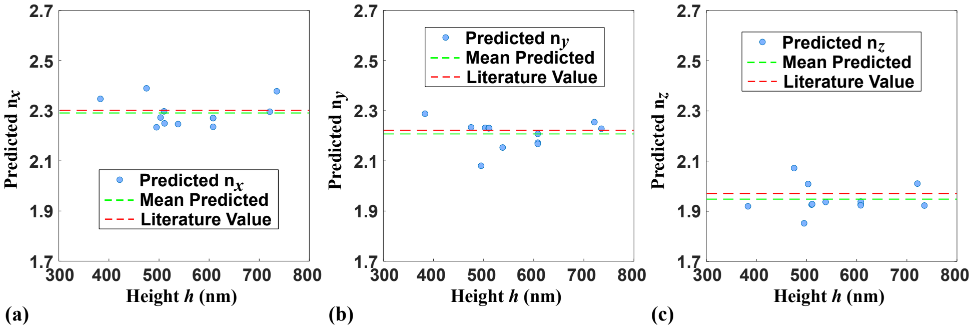

Figure 7.8: Stability test of AnisoVision for α-MoO$_3$ flakes of varying thicknesses. Each point corresponds to a retrieved refractive index (n_x, n_y, or n_z) for a single flake, plotted as a function of the measured height. The red dashed line indicates the expected (literature) value, while the green dotted line shows the mean of the predicted values. Despite changes in thickness, the model consistently predicts the same optical properties.

of 0.0274, 0.0307, and 0.0303, respectively. These results not only fall within the expected experimental uncertainty but also agree well with literature reported values for α-MoO$_3$ [42].

The slight fluctuations observed are attributed primarily to sample imperfections, surface roughness, and minor experimental noise, rather than model instability. The low spread in retrieved indices demonstrates the stability and reliability of AnisoVision when applied to realistic, variable-thickness flakes, further reinforcing its utility for high-throughput characterization of 2D anisotropic materials.

7.2.5. JOINT RETRIEVAL OF THICKNESS AND REFRACTIVE INDEX USING CROSS-FLAKE CONSISTENCY

When multiple flakes of the same material with different thicknesses are available, the height–refractive index ambiguity can be resolved without explicitly using height as an input. While the AnisoVision model typically requires the flake thickness as an input to resolve the inherent coupling between optical path length and refractive index, this dependency can be bypassed when multiple flakes of the same material but different thicknesses are available. In such cases, the model is evaluated for each flake across a range of candidate thicknesses. The correct thickness values are those that yield consistent refractive index predictions across all flakes. Because only the true thicknesses produce a common triplet (n_x, n_y, n_z) for all flakes, this method enables simultaneous retrieval of both thickness and refractive indices purely from the consistency constraint across samples.

When several flakes belong to the same anisotropic material, they share the same intrinsic refractive indices, but have different thicknesses h_i. For each flake i, the trained model predicts, $n_i^{\text{pred}}(h) = (n_{x,i}(h), n_{y,i}(h), n_{z,i}(h))$, when evaluated at a candidate height h. If the assumed height is incorrect, the prediction compensates for the wrong optical path length and therefore deviates from the true material refractive index, and only the correct thicknesses will produce refractive index predictions that agree across all flakes: $n_1^{\text{pred}}(h_1) \approx n_2^{\text{pred}}(h_2) \approx \cdots \approx n$.

For each flake i, we evaluate the model over a discrete height range $h_i \in [h^{\text{min}}, h^{\text{max}}]$, storing $n_i^{\text{pred}}(h_i)$. For any combination of heights $h_1, \ldots, h_F$ across flakes, we compute the maximum inter-flake deviation: $\Delta(h_i, \ldots, h_F) = \max_i n_i^{\text{pred}}(h_i) - \min_i n_i^{\text{pred}}(h_i)$. A combination is accepted if $||\Delta(h_1, \ldots, h_F)||_\infty < \varepsilon$, meaning the predicted indices agree within a small tolerance ε. All accepted height combinations form the "consistent solution set," from which we compute the refined thickness for each flake (mean ± std of all accepted h_i). This is a robust method because the far-field reflectance depends on the optical path length. If an incorrect height is provided, the network's predicted refractive index shifts to compensate. Therefore, flakes of the same material will only produce consistent refractive index predictions when their correct heights are used. This removes the intrinsic n–h coupling without requiring height as an explicit input or as a trainable output, as shown in the Table 7.2. However, the accuracy and std deviation are higher than we can achieve if the neural network model is used to do the same.

Table 7.2: Recovered thicknesses and predicted refractive indices for two α-MoO$_3$ flakes using cross-flake consistency.

h^{AFM} (nm)	$h^{\text{retrieved}}$ (nm)	$\Delta h^{\text{retrieved}}$ (nm)	n_x	n_y	n_z
510	515	16	2.3026	2.1453	1.9791
735	715	21	2.3145	2.1620	1.9953

While this cross-flake approach allows estimation of both thickness and refractive indices using only far-field reflectance data, it requires data of two or more flakes of the same material. For single flakes, AnisoVision still provides accurate single-shot predictions of refractive indices, but the height must be measured independently, e.g., using AFM/SEM.

7.3. SUMMARY

In this chapter, we demonstrated a data-driven approach for retrieving the anisotropic optical constants of thin films by combining coherent Fourier scatterometry (CFS) with deep learning. Using the angular diversity of far-field scattering, our framework, AnisoVision, accurately reconstructs the full refractive index tensor (n_x, n_y, n_z) from single-shot measurements. Validated on simulated and experimental data for isotropic (SiN, SiO_2), uniaxial (h-BN), and biaxial (α-MoO_3) materials, the method showed excellent agreement with literature values and independent thickness measurements.

By using radially polarized illumination and selecting only a few angular cross-sections, we significantly reduced data dimensionality while maintaining retrieval accuracy. The approach is robust to flake thickness variations and does not require prior knowledge of crystal orientation, as a symmetry-based rotation-correction procedure recovers principal axes in biaxial crystals. Its local, non-destructive, and single-shot nature makes it well-suited for high-throughput mapping of anisotropy, defect characterization, and stress analysis.

While current demonstrations are monochromatic, the framework is compatible with multispectral or broadband implementations for dispersion-sensitive metrology. In particular, two-pulse broadband CFS, as demonstrated by van der Sijs *et al.* [43], could enable single-shot, spectrally resolved anisotropic characterization, paving the way toward dispersion-sensitive metrology using the same framework. Overall, this work establishes CFS, enhanced by deep learning, as a powerful and scalable platform for quantitative anisotropic tensor characterization in advanced photonic and layered material systems.

BIBLIOGRAPHY

[1] Anubhav Paul et al. "Characterization of the 3D-Optical Properties of van der Waals Materials with Deep Learning-Based Coherent Fourier Scatterometry". In: *ACS Photonics* 13.1 (2026), pp. 224–235. DOI: `10.1021/acsphotonics.5c02153`.

[2] Panaiot G Zotev et al. "Van der Waals materials for applications in nanophotonics". In: *Laser & Photonics Reviews* 17.8 (2023), p. 2200957. DOI: `10.1002/lpor.202200957`.

[3] Sina Abedini Dereshgi et al. "Low-Symmetry α-MoO3 Heterostructures for Wave Plate Applications in Visible Frequencies". In: *Advanced Optical Materials* 11.7 (2023), p. 2202603. DOI: `10.1002/adom.202202603`.

[4] Gonzalo Álvarez-Pérez et al. "Infrared permittivity of the biaxial van der waals semiconductor α-MoO3 from near-and far-field correlative studies". In: *Advanced Materials* 32.29 (2020), p. 1908176. DOI: `10.1002/adom.202202603`.

[5] Bin Lu et al. "When machine learning meets 2D materials: a review". In: *Advanced Science* 11.13 (2024), p. 2305277. DOI: `10.1002/advs.202305277`.

[6] Michael T Enders et al. "Deeply subwavelength mid-infrared phase retardation with α-MoO3 flakes". In: *Communications Materials* 5.1 (2024), p. 16. DOI: `10.1038/s43246-024-00453-z`.

[7] Mitradeep Sarkar et al. "Lithography-free directional control of thermal emission". In: *Nanophotonics* 13.5 (2024), pp. 763–771. DOI: `10.1515/nanoph-2023-0595`.

[8] DV Grudinin et al. "Hexagonal boron nitride nanophotonics: a record-breaking material for the ultraviolet and visible spectral ranges". In: *Materials Horizons* 10.7 (2023), pp. 2427–2435. DOI: `10.1039/D3MH00215B`.

[9] Wanfu Shen et al. "Origins and cavity-based regulation of optical anisotropy of α-MoO3 crystal". In: *2D Materials* 10.1 (2022), p. 015024. DOI: `10.1088/2053-1583/acad13`.

[10] Luc Lajaunie et al. "Strong anisotropic influence of local-field effects on the dielectric response of α-MoO 3". In: *Physical Review B—Condensed Matter and Materials Physics* 88.11 (2013), p. 115141. DOI: `10.1103/PhysRevB.88.115141`.

[11] M Erman and JB Theeten. "Spatially resolved ellipsometry". In: *Journal of Applied Physics* 60.3 (1986), pp. 859–873. DOI: `10.1063/1.337327`.

[12] Yecheng Ma et al. "Optical parameters of graphene/MoS2 van der Waals heterostructure investigated by spectroscopic ellipsometry". In: *Applied Surface Science* 599 (2022), p. 153987. DOI: `10.1016/j.apsusc.2022.153987`.

[13] Mingze He et al. "Anisotropy and Modal Hybridization in Infrared Nanophotonics Using Low-Symmetry Materials". In: *ACS Photonics* 9.4 (2022), pp. 1078–1095. DOI: `10.1021/acsphotonics.1c01486`.

[14] Grazia Giuseppina Politano and Carlo Versace. “Spectroscopic ellipsometry: advancements, applications and future prospects in optical characterization”. In: *Spectroscopy Journal* 1.3 (2023), pp. 163–181. DOI: `10.3390/spectroscj1030014`.

[15] Wanfu Shen et al. “Resolving the optical anisotropy of low-symmetry 2D materials”. In: *Nanoscale* 10.17 (2018), pp. 8329–8337. DOI: `10.1039/C7NR09173G`.

[16] Anubhav Paul et al. “Investigation of coherent Fourier scatterometry as a calibration tool for determination of steep side wall angle and height of a nanostructure”. In: *Measurement Science and Technology* 35.7 (2024), p. 075202. DOI: `10.1088/1361-6501/ad3773`.

[17] Nitish Kumar et al. “Reconstruction of sub-wavelength features and nano-positioning of gratings using coherent Fourier scatterometry”. In: *Optics Express* 22.20 (2014), pp. 24678–24688. DOI: `10.1364/OE.22.024678`.

[18] Anubhav Paul et al. “Coherent Fourier scatterometry: a holistic tool for inspection of isolated particles or defects on gratings”. In: *Applied Optics* 62.29 (2023), pp. 7589–7595. DOI: `10.1364/AO.503350`.

[19] Chao Zuo et al. “Deep learning in optical metrology: a review”. In: *Light: Science & Applications* 11.1 (2022), p. 39. DOI: `10.1038/s41377-022-00714-x`.

[20] Lei Zhang and Shaofeng Shao. “Image-based machine learning for materials science”. In: *Journal of Applied Physics* 132.10 (2022), p. 100701. DOI: `10.1063/5.0087381`.

[21] Yifei Li et al. “Deep learning for rapid analysis of spectroscopic ellipsometry data”. In: *Advanced Photonics Research* 2.12 (2021), p. 2100147. DOI: `10.1002/adpr.202100147`.

[22] Yu Mao et al. “Thickness determination of ultrathin 2D materials empowered by machine learning algorithms”. In: *Laser & Photonics Reviews* 17.4 (2023), p. 2200357. DOI: `10.1002/lpor.202200357`.

[23] Yaodong Xu et al. “Machine learning enhanced optical microscopy for the rapid morphology characterization of silver nanoparticles”. In: *ACS Applied Materials & Interfaces* 15.14 (2023), pp. 18244–18251. DOI: `10.1021/acsami.3c02448`.

[24] Bingnan Han et al. “Deep-learning-enabled fast optical identification and characterization of 2D materials”. In: *Advanced Materials* 32.29 (2020), p. 2000953. DOI: `10.1002/adma.202000953`.

[25] Shuo Liu et al. “Inverse optical scatterometry using sketch-guided deep learning”. In: *Optics Express* 32.11 (2024), pp. 20303–20315. DOI: `10.1364/OE.524091`.

[26] Dmytro Kolenov and SF Pereira. “Machine learning techniques applied for the detection of nanoparticles on surfaces using coherent Fourier scatterometry”. In: *Optics Express* 28.13 (2020), pp. 19163–19186. DOI: `10.1364/OE.395233`.

[27] Kefu Ning et al. “Deep self-learning enables fast, high-fidelity isotropic resolution restoration for volumetric fluorescence microscopy”. In: *Light: Science & Applications* 12.1 (2023), p. 204. DOI: `10.1038/s41377-023-01230-2`.

[28] Julius Adams Stratton. *Electromagnetic theory*. John Wiley & Sons, 2007.

[29] Dwight W Berreman. “Optics in stratified and anisotropic media: 4× 4-matrix formulation”. In: *Journal of the Optical Society of America* 62.4 (1972), pp. 502–510. DOI: 10.1364/JOSA.62.000502.

[30] Mélanie M Bay, Silvia Vignolini, and Kevin Vynck. “PyLlama: A stable and versatile Python toolkit for the electromagnetic modelling of multilayered anisotropic media”. In: *Computer Physics Communications* 273 (2022), p. 108256. DOI: 10.1016/j.cpc.2021.108256.

[31] Jean-Paul Hugonin and Philippe Lalanne. *Analysis of stacks of anisotropic uniform layers: user guide for the RETICOLOfilm-stack program*. 2022. URL: https://hal.science/hal-03899689.

[32] Alexey P Porfirev, Andrey V Ustinov, and Svetlana N Khonina. “Polarization conversion when focusing cylindrically polarized vortex beams”. In: *Scientific Reports* 6.1 (2016), p. 6. DOI: 10.1038/s41598-016-0015-2.

[33] Jan Laermann, Wojciech Samek, and Nils Strodthoff. “Achieving Generalizable Robustness of Deep Neural Networks by Stability Training”. In: *Pattern Recognition*. Ed. by Gernot A. Fink, Simone Frintrop, and Xiaoyi Jiang. Cham: Springer International Publishing, 2019, pp. 360–373. DOI: 10.1007/978-3-030-33676-9_25.

[34] Hyungki Shim, Francesco Monticone, and Owen D Miller. “Fundamental limits to the refractive index of transparent optical materials”. In: *Advanced Materials* 33.43 (2021), p. 2103946. DOI: 10.1002/adma.202103946.

[35] Kevin Luke et al. “Broadband mid-infrared frequency comb generation in a Si3N4 microresonator”. In: *Optics Letters* 40.21 (2015), pp. 4823–4826. DOI: 10.1364/OL.40.004823.

[36] Luis V Rodríguez-de Marcos et al. “Self-consistent optical constants of SiO2 and Ta2O5 films”. In: *Optical Materials Express* 6.11 (2016), pp. 3622–3637. DOI: 10.1364/OME.6.003622.

[37] Daniel Franta et al. “Optical characterization of SiO2 thin films using universal dispersion model over wide spectral range”. In: *Optical Micro-and Nanometrology VI*. Vol. 9890. SPIE. 2016, p. 989014. DOI: 10.1117/12.2227580.

[38] Han Lin et al. “Engineering van der Waals Materials for Advanced Metaphotonics”. In: *Chemical Reviews* 122.19 (2022). PMID: 35749269, pp. 15204–15355. DOI: 10.1021/acs.chemrev.2c00048.

[39] Pulickel Ajayan, Philip Kim, and Kaustav Banerjee. “Two-dimensional van der Waals materials”. In: *Physics Today* 69.9 (2016), pp. 38–44. DOI: 10.1063/pt.3.3297.

[40] A Segura et al. “Natural optical anisotropy of h-BN: Highest giant birefringence in a bulk crystal through the mid-infrared to ultraviolet range”. In: *Physical Review Materials* 2.2 (2018), p. 024001. DOI: 10.1103/PhysRevMaterials.2.024001.

[41] Yoonhyuk Rah et al. “Optical analysis of the refractive index and birefringence of hexagonal boron nitride from the visible to near-infrared”. In: *Optics Letters* 44.15 (2019), pp. 3797–3800. DOI: 10.1364/OL.44.003797.

[42] Daniel Andres-Penares et al. “Optical and dielectric properties of MoO3 nanosheets for van der Waals heterostructures”. In: *Applied Physics Letters* 119.22 (2021), p. 223104. DOI: `10.1063/5.0066219`.

[43] T. A. van der Sijs et al. “Broadband coherent Fourier scatterometry: A two-pulse approach”. In: *Review of Scientific Instruments* 96.1 (2025), p. 013702. DOI: `10.1063/5.0226043`.

8

CONCLUSIONS AND OUTLOOK

This thesis has advanced coherent Fourier scatterometry (CFS) from a niche optical method into a broader, more capable framework for nanoscale metrology. Across the work, CFS has been strengthened along three dimensions: sensitivity, generality, and functional scope. First, the technique has been shown to detect and interpret subtle light–matter interactions at the nanoscale, extending its sensitivity to smaller particles, weak scattering signatures, and geometrically complex structures. Second, CFS has been expanded beyond periodic diffraction problems to encompass a range of aperiodic, anisotropic, and buried structures, demonstrating that far-field angular scattering carries rich information even when classical optical resolution limits would suggest otherwise. Third, this thesis has established pathways for CFS not only as a detection tool, but also as a method for *quantitative dimensional measurement, material characterization,* and *shape classification.* Together, these developments illustrate a recurring theme: **CFS, when supported by proper optical design, modeling, and data processing, can extract more information from scattered light than traditional interpretations typically assume.**

The work has further shown that CFS can transition from a laboratory-scale concept to a technology aligned with modern semiconductor and nanomaterial metrology needs. Focused-beam architectures, advanced detection schemes, near-infrared illumination, and data-driven retrieval all contribute to making CFS faster, more flexible, and more informative than earlier implementations. Ultimately, this thesis demonstrates that CFS is not limited by geometry, periodicity, or isotropy; it is a scalable optical metrology method capable of resolving nanoscale structure, composition, and anisotropy in ways that are non-destructive, local, and compatible with high-throughput inspection. The technical progress made here lays the foundation for CFS to evolve into a unified and technologically relevant nanoscale metrology platform.

8.1. OUTLOOK 1: MICROSPHERE-ASSISTED CFS

One of the fundamental limits of CFS (as with any far-field optical method) is the diffraction-limited size of the focal spot, which restricts the minimum feature size that can be interrogated or the sensitivity to weak scatterers. A promising way to overcome this limit is to integrate microsphere-assisted optics, using dielectric microspheres to generate photonic nanojets, which focus light into sub-diffraction-limited, high-intensity beams. Such "super-lenses" formed by microspheres have already proven effective in microscopy for super-resolution imaging and label-free nanostructure inspection [1–4].

By placing a microsphere on (or near) the sample surface and aligning the CFS illumination through the sphere, one could create a highly confined probing volume, boosting sensitivity to extremely small particles, shallow defects, or ultrafine geometrical variations. This microsphere-assisted CFS (μ-CFS) could bridge the gap between near-field sensitivity and far-field simplicity: offering sub-diffraction metrology without contact, labeling, or complex tip-based scanning. Applications may include detection of sub-10 nm contaminants, nanoscale roughness measurement, or high-resolution shape/edge metrology on photonic devices, nanophotonic gratings, or semiconductor wafers. Further, because microspheres are inexpensive and easy to integrate, μ-CFS could offer a cost-effective upgrade to existing CFS platforms.

8.2. OUTLOOK 2: FIBER-BASED / WAVEGUIDE-INTEGRATED CFS

A major practical challenge for deploying CFS, especially in industrial or in-situ environments, is the bulkiness and alignment demands of free-space optics (objective lenses, beam splitters, relays, etc.). An alternative direction is to develop a fiber- or photonic-waveguide-based CFS system, where optical excitation and collection are carried entirely through optical fibers or integrated waveguides. Using fibers would allow the system to access hard-to-reach or confined spaces, such as inside deep trenches, vias, microfluidic chips, or 3D-integrated packages, where bulky microscope objectives cannot reach [5, 6].

Fiber-based scattering measurements have proven successful in many domains (e.g., light scattering in microfluidics, fiber-based bio-sensing, photoacoustic microscopy, fluorescence imaging) thanks to their flexibility, compactness, and robustness [7–10]. By adapting such concepts to CFS, coupling a fiber or waveguide to the sample, and collecting scattered light back into the same or another fiber, one could build a compact, portable, and alignment-free CFS probe. This would significantly increase the flexibility and deployment potential of CFS, e.g., for inline monitoring in semiconductor lines, inspection of internal surfaces of assembled devices, or metrology inside microfluidic chips or MEMS devices.

8.3. OUTLOOK 3: HYBRID METROLOGY (CFS COMBINED WITH OTHER TECHNIQUES)

No single metrology technique can address all needs; every method has trade-offs: resolution vs throughput, surface vs subsurface sensitivity, structural vs material contrast, etc. A promising direction is hybrid metrology, where CFS is combined with complementary techniques to form a holistic metrology toolbox [11, 12]. For example:

- Combining CFS with scanning-probe methods (e.g., AFM) or electron microscopy (SEM) for regions needing ultra-high spatial resolution or chemical/material contrast.
- Integrating CFS with spectroscopic techniques (e.g., Raman, photoluminescence, or ellipsometry) to simultaneously retrieve structural geometry and material composition or stress/strain, particularly useful for complex layered or anisotropic materials.
- Merging CFS with interferometric or phase-based metrology (e.g., structured-illumination interferometry, digital holography) to obtain both angular scattering (for defects/shape) and phase/topography information (for thickness, profile, surface roughness).

In addition, CFS is closely related to ptychography, as both employ coherent illumination, scanned focused probes, and far-field detection with pixelated sensors [13–16]. Although ptychography enables high-resolution phase and amplitude reconstruction via iterative algorithms, CFS provides direct, high-sensitivity access to angular scattering asymmetries associated with defects, edges, and anisotropies. A hybrid CFS–ptychography approach could combine rapid defect localization with quantitative complex-field reconstruction, enabling adaptive and information-efficient inspection workflows.

Such hybrid systems can leverage the strengths of each technique while compensating for their weaknesses, resulting in more comprehensive metrology solutions, especially relevant for advanced semiconductor, photonic, and 3D-integrated packaging technologies.

8.4. FINAL REMARKS

Over the course of this thesis, we have shown that CFS, once considered a rather academic, niche method, can be transformed into a powerful, flexible, and scalable metrology platform suitable for the demands of modern nanofabrication and device integration. By advancing its sensitivity, versatility, and interpretability through a combination of rigorous simulation, detection/illumination design, and data-driven signal processing, we have expanded its scope far beyond classical scatterometry.

The future directions outlined above: microsphere-assisted focusing, fiber-based probes, and hybrid metrology represent natural and promising evolutions of this work. If realized, they can push CFS into new regimes: sub-diffraction metrology, in-situ industrial inspection, multidimensional material characterization, and high-throughput nano-quality control.

In this way, the foundations laid in this thesis can serve as a springboard for next-generation optical metrology systems, not only for continued academic research, but also for practical deployment in semiconductor manufacturing, photonics, materials science, and beyond.

BIBLIOGRAPHY

[1] Arash Darafsheh. “Microsphere-assisted microscopy”. In: *Journal of Applied Physics* 131.3 (2022), p. 031102. DOI: `10.1063/5.0068263`.

[2] Sylvain Lecler et al. “Photonic jet lens”. In: *Scientific Reports* 9.1 (2019), p. 4725. DOI: `10.1038/s41598-019-41193-2`.

[3] Jangryul Park et al. “Microsphere-assisted hyperspectral imaging: super-resolution, non-destructive metrology for semiconductor devices”. In: *Light: Science & Applications* 13.1 (2024), p. 122. DOI: `10.1038/s41377-024-01469-3`.

[4] Soonyang Kwon et al. “Microsphere-assisted, nanospot, non-destructive metrology for semiconductor devices”. In: *Light: Science & Applications* 11.1 (2022), p. 32. DOI: `10.1038/s41377-022-00720-z`.

[5] Jinlong Zhu et al. “Optical wafer defect inspection at the 10 nm technology node and beyond”. In: *International Journal of Extreme Manufacturing* 4.3 (2022), p. 032001. DOI: `10.1088/2631-7990/ac64d7`.

[6] Elisabeth Mansfield et al. *International Roadmap for Devices and Systems^{TM} 2023 Edition Metrology*. 2023. URL: `https://irds.ieee.org/editions/2023`.

[7] Sundar Hengoju et al. “Advantages of optical fibers for facile and enhanced detection in droplet microfluidics”. In: *Biosensors and Bioelectronics* 200 (2022), p. 113910. DOI: `10.1016/j.bios.2021.113910`.

[8] David J Monk and David R Walt. “Optical fiber-based biosensors”. In: *Analytical and Bioanalytical Chemistry* 379.7 (2004), pp. 931–945. DOI: `10.1007/s00216-004-2650-x`.

[9] P. Hajireza, W. Shi, and R. J. Zemp. “Label-free in vivo fiber-based optical-resolution photoacoustic microscopy”. In: *Optics Letters* 36.20 (2011), pp. 4107–4109. DOI: `10.1364/OL.36.004107`.

[10] Benjamin A Flusberg et al. “Fiber-optic fluorescence imaging”. In: *Nature Methods* 2.12 (2005), pp. 941–950. DOI: `10.1038/nmeth820`.

[11] Wolfgang Osten. “The wide scale range of optical measurement technology and its exploration”. In: *Optical Measurement Systems for Industrial Inspection XIV*. Vol. 13567. SPIE. 2025, p. 1356702. DOI: `10.1117/12.3071536`.

[12] Alok Vaid et al. “A holistic metrology approach: hybrid metrology utilizing scatterometry, CD-AFM, and CD-SEM”. In: *Metrology, Inspection, and Process Control for Microlithography XXV*. Vol. 7971. SPIE. 2011, pp. 21–40. DOI: `10.1117/12.881632`.

[13] Guoan Zheng, Roarke Horstmeyer, and Changhuei Yang. “Wide-field, high-resolution Fourier ptychographic microscopy”. In: *Nature photonics* 7.9 (2013), pp. 739–745. DOI: `10.1038/nphoton.2013.187`.

[14] Guoan Zheng et al. “Concept, implementations and applications of Fourier ptychography”. In: *Nature Reviews Physics* 3.3 (2021), pp. 207–223. DOI: `10.1038/s42254-021-00280-y`.

[15] Yifeng Shao et al. “Wavelength-multiplexed multi-mode EUV reflection ptychography based on automatic differentiation”. In: *Light: Science & Applications* 13.1 (2024), p. 196. DOI: `10.1038/s41377-024-01558-3`.

[16] Wim Coene et al. “EUV imaging of nanostructures without lenses”. In: *UV and Higher Energy Photonics: From Materials to Applications 2024*. Vol. 13115. SPIE. 2024, pp. 22–25. DOI: `10.1117/12.3028711`.

A

DETAILS OF ZEMAX SIMULATIONS

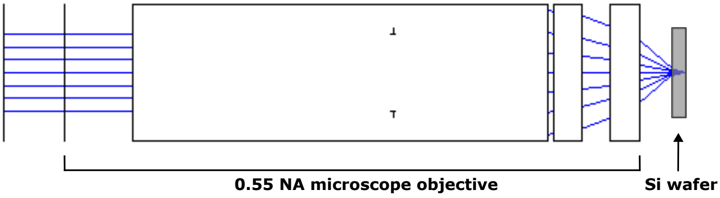

Figure A.1: Layout of the Zemax simulations for aberrations study.

Table A.1: **Parameters of the designed system**

Parameter	Values
Entrance pupil diameter	5.631335
Image space F/#	0.7591
Paraxial working F/#	0.7591
Working F/#	0.7483276
Image space N/A	0.55
Object space N/A	2.815667e-10

In this section, we describe how the aberrations study for Chapter 4 was performed using Zemax OpticsStudio software. In the simulations we mimic the experimental conditions, where a linearly polarized plane wave of wavelength 1055 nm, is illuminated on a microscope objective having a numerical aperture (NA) of 0.55. The objective focuses the light on a Si wafer of thickness H_{Si}, the Si wafer is moved such that the focused plane is on the backside of the wafer. The layout of the design in Zemax is shown in Fig. A.1.

In the simulations we use the physical optics propagation (POP) mode, where the field's wave nature, such as polarization and diffraction effects, are taken into account. Using this mode, we analyse the wavefront to calculate the Zernike coefficients of the focused spot at the back of the wafer for varying H_{Si}. Some of the important parameters of the simulations are provided in Table A.1.

B

MICROSCOPE OBJECTIVE CALIBRATION

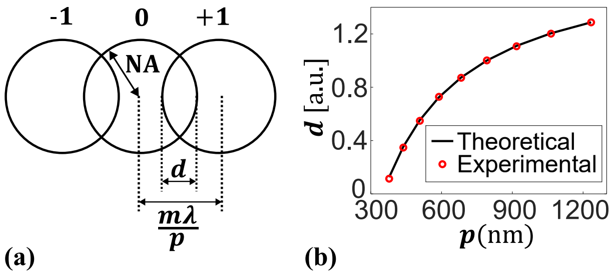

Figure B.1: (a) Schematic representation of diffraction order overlap in the back focal plane for a grating with period p. (b) Comparison of experimentally measured overlaps (red circles) with theoretical predictions (black curve), validating the NA of the microscope objective.

Accurate calibration of the microscope objective is essential for retrieving reliable optical constants using the AnisoVision model in Chapter 7. Suppose the actual numerical aperture (NA) of the objective deviates from the specified value due to lens imperfections or misalignment. In that case, it introduces systematic errors in the angular spectrum of the far-field, which is directly used as input to the model. This, in turn, can lead to incorrect predictions of material refractive indices.

To verify the fidelity of the objective, we employ a calibration procedure based on diffraction from 1D gratings with known periods. The idea is to examine the angular separation between diffraction orders as they appear in the back focal plane. As illustrated in Fig. B.1(a), the diffracted orders ($m = -1, 0, +1$) appear as overlapping circular regions. The overlap distance d between the central order and the m^{th} diffracted order depends on the grating period p, the wavelength λ, and the NA of the objective, and is given by:

$$d = 2 \cdot \mathrm{NA} - \frac{m\lambda}{p}. \tag{B.1}$$

To carry out this calibration, we measured the overlap distance d for a series of diffraction gratings with varying periods p, and image their far-field diffraction patterns. These experimental values are then compared to the theoretical expression derived above. Figure B.1(b) shows the comparison between measured overlaps and the corresponding theoretical predictions for multiple grating periods. The experimental data (red circles) show excellent agreement with the theoretical curve (black line), confirming that the objective is free of significant aberrations and that its effective NA matches the nominal specification. As such, this ensures that the angular spectrum collected during experiments accurately reflects the sample's scattering response, which is critical for robust performance of the AnisoVision model.

C

ANISOVISION MODEL ACCURACY STATISTICS

The model architecture consists of convolutional, pooling, and dense layers. It receives multiple inputs and processes them through successive feature extraction and integration steps. The Table C.1 summarizes the layer types, output shapes, and number of parameters for each layer.

The dataset used for training, validation, and testing the model consisted of 25,200,000 samples, with 20,160,000 samples allocated for training and 5,040,000 samples for testing. Among the total samples, approximately 4% were isotropic materials, 4% were uniaxial materials, and the remaining 92% were anisotropic, reflecting a strong emphasis on anisotropic materials for predicting refractive indices. Each sample consists of three cross-sections of the the far-field scattering response along with the flake thickness. Each cross-section was then resized to 64 points, normalized individually, and optionally augmented with Gaussian noise ($\sigma \in$[0.1 -0.001]) to account for practical measurement variations and limitations. The resulting training inputs had shapes (20160000, 64, 1) for each cross-section and corresponding outputs of shape (20160000, 3), while the testing inputs had shapes (5040000, 64, 1) and outputs (5040000, 3). This preprocessing ensured uniformity across samples, enhanced the model's generalization, and allowed it to accurately learn patterns from isotropic, uniaxial, and anisotropic materials.

The model was trained for 10 epochs on 20,160,000 training samples with a batch size resulting in 126,000 steps per epoch. During the first epoch, the model started with a relatively high loss of 1.6093 and a mean absolute error (MAE) of 0.2793, while the validation loss was 0.0323 with a validation MAE of 0.1222, indicating a significant initial difference between training and validation scales due to the large dataset and normalization. Over successive epochs, both training and validation metrics improved steadily, with the training loss decreasing to 0.0165 and MAE to 0.0742 by the 10th epoch. The validation loss reached a minimum of 0.0163 with an MAE of 0.0728 during epoch 9, before slightly increasing in epoch 10, reflecting good generalization with minor fluctuations. Overall, the training history demonstrates that the model converged effectively, reducing both loss

Table C.1: Summary of AnisoVision model layers (type, output shape, parameters).

Layer (type)	**Output shape**	**Param #**	**Connected to**
input_layer_2 (InputLayer)	(None,64,1)	0	-
convid_2 (Convid)	(None,64,32)	128	input_layer_2[0][0]
max_poolingid_2 (MaxPoolingID)	(None,32,32)	0	convid_2[0][0]
convid_3 (Convid)	(None,32,64)	6208	max_poolingid_2[0][0]
max_poolingid_3 (MaxPoolingID)	(None,16,64)	0	convid_3[0][0]
global_average_poolingid_1 (GlobalAveragePoolingID)	(None,64)	0	max_poolingid_3[0][0]
dense_3 (Dense)	(None,32)	2080	global_average_poolingid_1[0][0]
dense_4 (Dense)	(None,64)	2112	dense_3[0][0]
reshape_1 (Reshape)	(None,1,64)	0	dense_4[0][0]
multiply_1 (Multiply)	(None,16,64)	0	max_poolingid_3[0][0], reshape_1[0][0]
input_layer_1 (InputLayer)	(None,64,1)	0	-
flatten_1 (Flatten)	(None,1024)	0	multiply_1[0][0]
input_layer_3 (InputLayer)	(None, 64, 1)	0	-
functional (Functional)	(None, 64)	76128	input_layer_1[0][0], input_layer_3[0][0]
dense_5 (Dense)	(None, 64)	65000	flatten_1[0][0]
concatenate (Concatenate)	(None, 192)	0	functional[0][0], dense_5[0][0], functional[1][0]
dense_6 (Dense)	(None, 96)	18528	concatenate[0][0]
dense_7 (Dense)	(None, 96)	9312	dense_6[0][0]
multiply_2 (Multiply)	(None, 96)	0	dense_6[0][0], dense_7[0][0]
h_input (InputLayer)	(None, 1)	0	-
concatenate_1 (Concatenate)	(None,97)	0	multiply_2[0][0], h_input[0][0]
dense_8 (Dense)	(None, 64)	6272	concatenate_1[0][0]
n_x (Dense)	(None, 1)	65	dense_8[0][0]
n_y (Dense)	(None, 1)	65	dense_8[0][0]
n_z (Dense)	(None, 1)	65	dense_8[0][0]
final_output (Concatenate)	(None, 3)	0	n_x[0][0], n_y[0][0], n_z[0][0]

and error on unseen validation data while maintaining stability, highlighting its capability to accurately predict refractive index components from the cross-sectional profiles.

The model was evaluated on the test set consisting of 5,040,000 samples, achieving a test loss of 0.0188 and a mean absolute error (MAE) of 0.0781. This indicates that the model generalizes well to unseen data, maintaining a low prediction error and demonstrating consistent performance compared to the training and validation results.

Table C.2: Statistical summary of the components n_x, n_y, and n_z showing mean, median, and standard deviation.

Component	n_x	n_y	n_z
Mean	0.065362	0.072127	0.084714
Median	0.040221	0.046504	0.055828
Std. Dev.	0.088869	0.095604	0.097459

Table C.2 presents the statistical summary of the predicted components n_x, n_y, and n_z of 10,000 random configurations, sampled across the parameter space ($h \in [200, 800]$ nm and $n_i \in [1.3, 4.0]$). The components n_x, n_y, and n_z show average values (0.065, 0.072, 0.085), with medians slightly lower than means, indicating slightly skewed distributions. Standard deviations range from 0.089 to 0.097, capturing minor variability in the data.

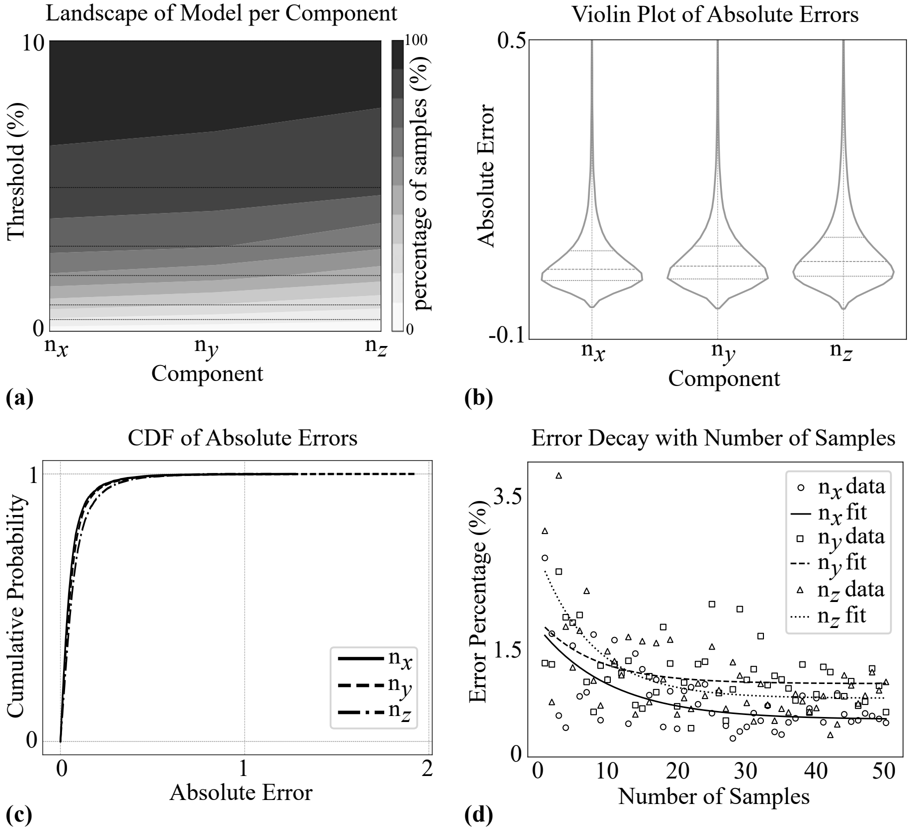

Figure C.1: Model performance for n_x, n_y, and n_z: (a) prediction coverage across error thresholds, (b) violin plots of absolute errors with medians and interquartile ranges, (c) CDFs of absolute errors, and (d) Prediction Error (in %) as a function of the number of samples for n_x, n_y, and n_z.

The accuracy landscape (Fig. C.1(a)) shows that prediction coverage for n_x, n_y, and n_z increases with wider error thresholds, with over 80% of predictions within 5% error and over 96% within 10%. Violin plots (Fig. C.1(b)) of absolute errors indicate medians of 0.040 (n_x), 0.047 (n_y), and 0.056 (n_z), with interquartile ranges below 0.1 for all components. The CDF plot (Fig. C.1(c)) shows that the majority of predictions for all three components fall within relatively low absolute errors. At the 50% cumulative probability level, n_x has the smallest error (0.040), followed by n_y (0.047) and n_z (0.056). The error decay data show that the mean absolute errors decrease as more samples are aggregated, highlighting improved stability in predictions (Fig. C.1(d)). Across all sample sizes, n_x generally exhibits lower errors compared to n_y and n_z, indicating it is predicted most reliably. n_z shows higher variability, particularly at smaller sample counts, suggesting that it is more sensitive to sampling fluctuations. The overall exponential decay trend demonstrates that averaging over multiple similar samples effectively reduces prediction error, confirming the model's robustness and the benefit of sample aggregation for stabilizing predictions, hence averaging improves accuracy.

D

ROTATION OF FAR-FIELD IMAGES

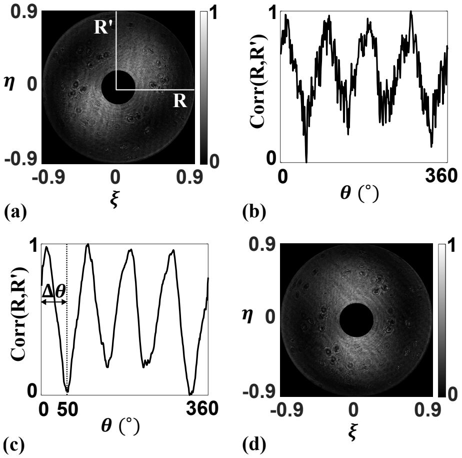

Figure D.1: (a) Measured far-field pattern from an exfoliated α-MoO$_3$ flake, with two orthogonal radial profiles R and R' shown. (b) Computed correlation function corr2(R, R') between radial pairs as a function of rotation angle. (c) Smoothed correlation function showing the reduced correlation at $\Delta\theta = 50^\circ$. (d) Far-field image after rotational correction by $\Delta\theta$, aligned with the crystal axes.

In this section, we outline the method used to correct for the unknown crystal axis orientation in mechanically exfoliated biaxial flakes. For such flakes, the in-plane crystal axes can be randomly rotated with respect to the laboratory reference frame. To accurately retrieve the anisotropic refractive indices n_x, n_y, n_z, the measured far-field must first be realigned such that the in-plane optical axes align with fixed angular directions (e.g., $\phi = 0^\circ, 45^\circ, 90^\circ$) used by the AnisoVision model. As illustrated in Fig. D.1(a), we begin with the measured far-field pattern for an exfoliated α-MoO$_3$ flake. Two orthogonal radial line profiles, R and R', are extracted at angles separated by 90°. In general, if the crystal axes are not aligned with these radial directions, the two profiles will be correlated due to mixed index contributions. However, when the crystal axes align with R and R', the optical response becomes independent of the orthogonal in-plane index, minimizing the correlation between the two profiles.

To systematically identify this alignment, we define an angular correlation function:

$$\mathrm{corr2}(R, R') = \frac{\sum_{i=1}^{N} (R_\theta - \bar{R}_\theta)(R'_\theta - \bar{R}'_\theta)}{\sqrt{(\sum_{i=1}^{N} (R_\theta - \bar{R}_\theta)^2)(\sum_{i=1}^{N} (R'_\theta - \bar{R}'_\theta)^2)}}, \tag{D.1}$$

where R_θ and R'_θ denote radial intensity profiles extracted from directions θ and $\theta + 90°$, respectively, and $\bar{R}_\theta$ and $\bar{R}'_\theta$ are the mean of the respective profiles.

By evaluating corr2(R, R') over the full 0° to 360° range, as shown in Fig. D.1(b), we observe a periodic function with fourfold symmetry, as expected due to the equivalence of quadrants in the far-field. To improve robustness and suppress high-frequency noise, we apply a smoothing filter to the correlation function, as shown in Fig. D.1(c) (Both Fig. D.1(b) and Fig. D.1(c) are normalized between 0 and 1 for consistency and clarity in comparison). The global minimum in the smoothed curve indicates the angular offset $\Delta\theta$ needed to align the crystal axes with the reference coordinate system used in AnisoVision. For the case shown, we find $\Delta\theta = 50°$. After rotating the original far-field image by $\Delta\theta$, we obtain the corrected field shown in Fig. D.1(d). This aligned far-field is then used to extract the azimuthal cross-sections A, B, and C at 0°, 45°, and 90°, respectively, and fed into the AnisoVision model for the optical characterization of the material. This procedure ensures consistent and physically meaningful extraction of the anisotropic optical parameters from arbitrarily oriented exfoliated flakes.

E

AFM MEASUREMENT DETAILS

Atomic Force Microscopy (AFM) measurements were conducted to determine the thicknesses of the exfoliated flakes used in the study of Section 7.2.4, which is critical for accurate optical property retrieval using AnisoVision. The measurements were performed using a Bruker AFM system operated in non-contact mode (NCM) to minimize tip-induced surface deformation, ensuring accurate height characterization for mechanically exfoliated 2D materials.

AFM Imaging Parameters:

- **Imaging Mode:** Non-contact mode (NCM)
- **AFM Tip:** Bruker RTESP-300
- **Setpoint Amplitude:** 8 nm
- **Z-Gain:** 1.000
- **Proportional Gain (P-gain):** 5.000
- **Integral Gain (I-gain):** 2.000

Adaptive Scanning Settings:

- **Maximum Scan Speed:** 2 Hz
- **Minimum Scan Speed:** 0.1 – 0.15 Hz
- **Error Bound Threshold:** 1 nm

These adaptive scanning parameters were employed to ensure high-resolution and stable imaging across the flakes, especially in areas with rapid height variations or surface irregularities.

Post-Processing in Gwyddion:

To extract quantitative height information from the raw AFM scans, post-processing was carried out using the open-source software Gwyddion. The following sequence of operations was performed:

- **Slope Correction:** Removal of global sample tilt or curvature to obtain an even baseline.
- **Row Alignment:** Performed using the "median of differences" method to reduce line-by-line offsets and noise.
- **Scar Correction:** Horizontal scanning artifacts (if present) were corrected to ensure clean and continuous surface profiles.
- **Plane Leveling:** The data was leveled by fitting a best-fit plane through three reference points on the substrate.
- **Height Offset:** The minimum value of the surface was shifted to zero to simplify thickness measurements.
- **Profile Extraction:** Height profiles were manually drawn across step edges of the flakes to extract local thickness values.

These preprocessing steps ensured consistent and artifact-free measurements, enabling robust height estimation across multiple flakes. The extracted values were subsequently used as fixed input h for the AnisoVision model when retrieving the anisotropic refractive indices.

CURRICULUM VITÆ

Anubhav Paul

28-12-1998	Born in Siliguri, West Bengal, India.

EDUCATION

2004–2016	Kendriya Vidyalaya Sukna, Sukna, India	
2016–2019	Bachelor of Science in Physics, Siliguri College, North Bengal University, Siliguri, India	
2019–2021	Master of Science in Physics, Indian Institute of Technology Jodhpur, Jodhpur, India	
2022– 2025	Doctor of Philosophy (Ph.D.), Applied Physics, Delft University of Technology, The Netherlands	
	Thesis:	Advancing optical metrology with coherent Fourier scatterometry
	Promotor:	Dr. ir. S. F. Pereira
	Promotor:	Prof. dr. W. M. J. M. Coene

List of Publications

12. **A. Paul**, K. Rishav, G. Klootwijk, M. Sarkar, O. Bisht, Z. Li, S. Conesa-Boj, G. T. Papadakis, S. F. Pereira, *Characterization of the 3D-optical properties of van der Waals materials with deep learning based coherent Fourier scatterometry*, ACS Photonics **13**(1), 224-235 (2026).

11. **A. Paul**, M. Boonstra, S. F. Pereira, *Near-infrared coherent Fourier scatterometry for deep subsurface nanostructure metrology in silicon*, Optics and Lasers in Engineering **195**, 109354 (2025).

10. **A. Paul**, S. Soman, S. F. Pereira, *Recent developments in coherent Fourier scatterometry*, EPJ Web of Conferences **335**, 03041 (2025).

9. **A. Paul**, S. F. Pereira, *Implementation of quad detection scheme in coherent Fourier scatterometry for inspection of patterned structures*, Proc. SPIE **13567**, Optical Measurement Systems for Industrial Inspection XIV, 135671I (2025).

8. **A. Paul**, S. F. Pereira, *Limits of detection of defects near edges of nanostructures for coherent Fourier scatterometry*, Proc. SPIE **13567**, Optical Measurement Systems for Industrial Inspection XIV, 135672I (2025).

7. **A. Paul**, R. Wever, S. Soman, S. F. Pereira, *Utilizing focused field as a probe for shape determination of subwavelength structures via coherent Fourier scatterometry*, Physical Review Applied **23**, 024016 (2025).

6. **A. Paul**, J. Rafighdoost, X. Dou, S. F. Pereira, *Investigation of coherent Fourier scatterometry as a calibration tool for determination of steep side wall angle and height of a nanostructure*, Measurement Science and Technology **35**(7), 075202 (2024).

5. **A. Paul**, D. Kolenov, T. Scholte, S. F. Pereira, *Coherent Fourier scatterometry: a holistic tool for inspection of isolated particles or defects on gratings*, Applied Optics **62**(29), 7589-7595 (2023).

4. **A. Paul**, D. Kolenov, S. F. Pereira, *Coherent Fourier scatterometry for particle detection on structured surfaces*, EPJ Web of Conferences **266**, 10014 (2022).

3. **A. Paul**, A. Laha, S. Dey, S. Ghosh, *Asymmetric guidance of multiple hybrid modes through a gain-loss-assisted planar coupled-waveguide system hosting higher-order exceptional points*, Physical Review A **104**(6), 063503 (2021).

2. **A. Paul**, A. Laha, S. Dey, S. Ghosh, *Exceptional points and non-chiral mode conversion of hybrid-modes in a manifold coupled planar waveguide*, 2021 Opto-Electronics and Communications Conference (OECC), 1-3 (2021).

1. **A. Paul**, A. Laha, S. Ghosh, *Hosting of exceptional points in an atom-field interaction Hamiltonian and manipulation of light states*, Physica Scripta **96**(7), 075503 (2021).

ACKNOWLEDGEMENTS

A successful PhD is never the achievement of a single individual. It is the outcome of constant guidance from dedicated supervisors, the support of skilled technical staff, stimulating discussions with colleagues, and the encouragement of friends, both nearby and far away, who keep one grounded and motivated. This thesis is therefore as much a collective effort as it is a personal one, and I am deeply grateful to everyone who contributed to this journey in their own way.

First and foremost, I would like to express my sincere gratitude to my supervisors. I am deeply grateful to **Dr. Silvania F. Pereira**, my daily supervisor and promotor, for her unwavering support throughout this PhD. Her ability to plan research strategically, provide clear scientific direction, and remain constantly available for discussion made an enormous difference to my development as a researcher. Beyond her scientific mentorship, her warmth, friendliness, and encouragement created an environment in which I could grow with confidence. I am also grateful for the many non-scientific moments, including her cooking in group dinners, which made the journey all the more memorable. I would also like to thank **Dr. Wim M. J. M. Coene**, my promotor, for his invaluable feedback and broad perspective. His course on "Optics for Lithography" was instrumental in shaping my understanding of the field, and his deep connection to industrial challenges ensured that this research remained grounded in real-world relevance.

This PhD would not have been possible without the extraordinary support of the technical staff. **Roland Horsten**, thank you for always being ready to help, for the countless insightful discussions during group meetings, and for your passion for electronics, software, and cakes alike. Everything related to electronics and software in this research benefited from your expertise and enthusiasm. **Thim Zuidwijk**, your help with mechanical design, your lightning-fast solutions, and your mastery of the 3D printer were indispensable. **Thomas Scholte**, despite being constantly busy supporting many people, your assistance with fabrication and SEM measurements was crucial. All three of you consistently supported not only our group members, but many others as well, and I am extremely grateful for that.

I also sincerely thank **Lidija Nikolic**, our secretary. From administrative matters to friendly conversations, you ensured that everything ran smoothly, even under difficult circumstances. Joining after I started and leaving before I finished, you nevertheless made a lasting positive impact and removed countless worries along the way.

I gratefully acknowledge the support of our consortium partners. The project meetings, insightful questions, motivating discussions, and especially the industry visits greatly enriched this work. In particular, I would like to thank **Marnix Tas** for continuously motivating and inspiring us to aim higher, as well as **Peter van der Walle**, **Eric Kosters**, **Paul Bloom**, and **Sven Pekelder** for their valuable input and engagement.

My deepest thanks go to the core scatterometry group. **Sarika Soman**, my group mate and office mate for four years, your support during my first days in a new country helped me settle both professionally and personally. Our scientific discussions, countless non-scientific conversations, and legendary debates about whether West Bengal lies in North or East India (it is East!) made this journey unforgettable. You were a constant source of inspiration, and we still owe ourselves that Kerala trip. **Dmytro Kolenov**, your role in this PhD cannot be overstated. You trained me on the experimental tool when I had no idea where to begin, co-authored my first PhD paper, and always provided sharp and critical feedback; approval from you was a quality stamp. I will never forget your flamenco dance. **Jila Rafighdoost**, joining at the same time, you were always helpful and fun, and our road trips to Belgium remain some of my favorite memories. I also thank **Thomas van der Sijs**, **Han Frencken**, **Haoyang Yin**, **Jorik Nuijten**, **Xiujie Dou**, **Dion Jetulahi**, and **Freek Looman** for the support, discussions, and collaborative spirit that defined the group.

I greatly enjoyed supervising students **Robin Wever**, **Sven Notermans**, **Victor Adriani**, **Mathijs Boonstra**, **Guus Geelen**, **Guus Klootwijk**, and **Daniel de Graaf**. It was a pleasure working with all of you. Supervising you was as educational for me as it was for you, and I am proud of the work we accomplished together.

I am also grateful to the broader Optica cluster. **Frank van der Ceelen** and **Rishav Kumar**, although you joined later, we quickly became close through scientific discussions, collaborations, and countless games of table tennis, tennis, and badminton, not to mention the amazing food you guys cooked. **Bruno Lopez Rodriguez** and **Hui Wang**, I enjoyed our lab discussions and shared drinks. Thanks also to **Alex Heemels**, **Sander Senhorst**, **Thomas Kotte**, **Luuk Zonneveld**, **Jan de Graaf** (for bringing the fascinating and cool trucker vibe to the group), **Zizheng Li**, **Reint Koppert**, **Behnoosh Babaghorbani**, **Naresh Sharma** (your support and inspiration meant a lot, wishing you success as a PI in India), **JP** (for all the fun and stories), **Hong Zhao**, **Mathijs Velsink**, **Roald van der Kolk**, **Yifeng Shao**, **Sven Weerdenburg** (for being so active in organizing group events), **Anne Nurmohamed**, **Jonas van Eeten**, **Shrouk Eid Zaki**, **Chunxiao Chen**, and **Sofia Mariani**, thank you all for the good times and stimulating discussions. I would also thank the PIs **Iman Esmaeil Zadeh**, **Omar El Gawhary**, **Stefan Witte**, **Jian Rong Gao**, **Florian Bociort**, **Aurèle Adam**, and **Sonia Conesa-Boj** for engaging and insightful scientific discussions.

To my master's friends **Harshita Devda**, **Manisha**, **Shubham Sharma**, and **Akshima Negi**, we started our PhD journeys across different countries at the same time, and your support through thick and thin meant everything. Our trips across Italy, Germany, Croatia, and Greece were unforgettable, and we still owe ourselves a trip together with **Akshima**.

To the Khana Khazana group, **Pratik Tawade**, **Sameer Khan**, **Onima Bisht**, **Mohit Rodhia**, **Siddharth Singh**, **Lucas Huet**, **Mudassir Hussian**, **Barka Khan**, **DJ**, thank you for the food, the Bollywood parties, house dinners, and for making life feel like home. At one point, we were sharing lunch and dinner every day, and those shared meals became an essential part of my life during the PhD.

To my Dutch course friends, **Irene Orellana Plaza**, **Camila Martínez Torres**, **Boyan Kolev**, **Victor Weber**, **Simona Di Costanza**, **Davide Panico**, **Nilay Zaveri**, **Canan Tezgeç**, **Sereno**, and **Natalia**, what started as a language course turned into deep friendships. **Irene**, I am especially grateful for the time we spent together during your master's thesis in our group, and for the unforgettable memories we made during our trip to Madrid. Watching friends transition from thesis stress to job stress made the journey feel shared and real.

I also thank my friends in the Netherlands. **Lavanya Beri**, **Itir Bakis Dogru**, **Megha Khokhar**, **Vivek Gupta**, **Hemant Sharma**, **Antariksha Das**, **Julius Fischer**, **Taco Dommerholt**, **Deepika Poonia**, and **Shivani Gupta**, for your support in countless ways throughout the years.

Finally, I thank my constants back home. **Mahi Sarkar**, **Samrat Roy**, **Biswarup Biswas**, **Varun Yadav**, **Subham Singh**, **Prithviraj Debnath**, **Manisha Sengupta**, **Ravi Ranjan Das**, **Pragati Gupta**, **Md. Haroon**, **Sayani Roy Sarkar**, **Ritika Chaturvedi**, **Upasana Jharia**, and **Alliya Khurshid**. No matter the distance, you were always there when I needed you most.

Above all, I thank my family. To my **Ma**, the most important person in my life, your sacrifices, strength, and unconditional support are my greatest motivation. To my **Baba**, thank you for supporting me from childhood onward. To my **Didi**, you taught me everything from reading to speaking and have always been there for me. To my **Jija Ji**, welcome to the family. After you married my sister, I somehow ended up spending more time in Haryana than in West Bengal. And to **Aradhya**, my niece and the newest member of the family, although you may not understand this now, I hope one day seeing your uncle complete a PhD will inspire you to pursue science, curiosity, and knowledge.

This journey would not have been possible without all of you. Thank you.